



NTNU – Trondheim
Norwegian University of
Science and Technology

Combined EBSD-Investigations and In-situ Tensile Tests of a Direct Metal Deposited Ti6Al4V-Alloy

Lars Eriksen

Materials Science and Engineering

Submission date: June 2013

Supervisor: Jarle Hjelen, IMTE

Co-supervisor: Martin Mathisen, Norsk Titanium Components
Ola Jensrud, Sintef Raufoss

Norwegian University of Science and Technology
Department of Materials Science and Engineering

Preface

This work has been carried out at the Norwegian University of Science and Technology (NTNU) at the Department of Materials Science and Engineering, as a master thesis within the field of physical metallurgy.

First I would like to express my gratitude to my supervisor Professor Jarle Hjelen for useful conversations and advices along the way, especially on the EBSD-technique for sharing his knowledge in this field. Gratitude also goes to co-supervisor Martin Borlaug Mathisen at NTiC. His ability to transfer his knowledge on the Direct Metal Deposited Ti6Al4V-alloy has been admirable.

Trondheim, June 2013

Lars Eriksen

Acknowledgements

Sincere thanks to the following persons who have been of great help at different stages of this work. The supervisors have really balanced their job elegantly between providing the right information, challenging me, and encouraging me to follow my ideas throughout the work:

Professor Jarle Hjelen (NTNU):

Supervisor, help with improvements and challenges related to the EBSD + in situ equipment.

Martin Borlaug Mathisen (Norsk Titanium Components):

Co-supervisor, questions related to the DMD Ti6Al4V-alloy and the process parameters.

Ola Jensrud (SINTEF Raufoss Manufacturing):

Co-supervisor, questions related to the mechanical properties, chemical composition and solidification imperfections of the material investigated.

Dr. Yingda Yu (NTNU):

SEM, EBSD, sample preparation, analysing and indexing softwares.

And thank you to Norsk Titanium Components AS for delivery of sample material and financial support.

Abstract

Two blocks made of Ti6Al4V-alloy produced by Norsk Titanium Components new Direct Metal Deposition (DMD) production technology were delivered for this investigation. The main difference between the blocks was the different waiting time implemented in the production parameters. The different waiting time implied that the material were allowed to cool to desired Interpass Temperatures (IT). The blocks are referred to as T200 and T600 after their lowest IT of $<200^{\circ}\text{C}$ and $500\text{-}700^{\circ}\text{C}$, respectively. SINTEF Raufoss Manufacturing reported elongations of 5% and 8% in the deposition direction for the two blocks, which was lower than the 10% elongation obtained for the building direction. The objective was to find any explanations for the impaired ductility in the deposition direction, and why T200 have a lower elongation than T600. To reveal differences in microstructure and deformation mechanisms between the blocks was combined EBSD+In-situ. tensile tests the main tool. Complementary studies with optical microscopy of etched in-situ specimens were also performed to reveal macro deformations.

The work started with an extensive macroetching of different planes relative to the deposition direction. This revealed a 3D-image of the epitaxially growing solidification structure of columnar prior β -grains. Measurements of grain size and morphology did not indicate significant differences between the blocks. Later was EBSD selected to prior β -grain boundaries for specimens at the center of the blocks. Measurements of the thickness of primary α -phase also indicated small differences between the blocks. From this it was concluded that the different ITs lead to small differences in solidification structure and the amount of primary α -phase in the center of the blocks.

The EBSD + in-situ tensile tests were carried out for specimens fabricated from the blocks in the deposition direction, such that investigation could be performed in the XZ-plane. The force was applied parallel to the deposition direction X. The in-situ specimens in block T200 had a slightly higher position in the block giving a finer microstructure because of faster cooling rates. The T200 specimens also contained two deposition layers in contrast to only one in T600 specimens, this made a direct comparison difficult. However, from the four in-situ specimens investigated was the following concluded: specimens from T200 deformed more homogeneously on a macroscale. Correspondingly was more activity observed at prior β -grain boundaries for T600. The more active grain boundaries in T600 may result from the different cooling rates from the peak temperature. Slower cooling rates will give smaller prior β -grains decorated with more homogeneous α -phase along the boundaries of T600 specimens. The frequently reported detrimental mismatch between soft and hard HCP-grains in titanium alloys were also observed. However, the orientation and morphology of these grains seems to play an important role. Cracks growing along prior β -grains were always located at the side having a non-Burgers Orientation Relationship. The lamellar basketweave microstructure

also seem quite effective to stop cracks from growing further, because of the plates having distinct orientations.

This work has also uncovered the transition in microstructure between the substrate plate and first deposition layer. The microstructure develops from a very fine bimodal plate structure, through a equiaxed region with small amounts of primary α -phase, to early stages of the columnar β -grain configuration. The first columnar β -grains are very small in size compared to higher up in the block, and they contains very small amounts of primary α -phase. However, the basketweave microstructure develops relatively close to the substrate plate.

Sammendrag

To blokker av Ti6Al4V-materiale produsert med Norsk Titanium Components nye direkte metal deponerings-teknologi har blitt undersøkt i dette studiet. Hovedforskjellen mellom blokkene lå i hvilke ventetid som ble valgt mellom hvert lag deponert metall. Dette resulterer i at det siste laget avkjøles til en ønsket temperatur før neste lag legges oppå. Denne temperaturen kalles Interpass Temeperaturen (IT). De to blokkene ble navngitt T200 og T600 etter denne temperaturen på henholdsvis $<200^{\circ}\text{C}$ og $500\text{-}800^{\circ}\text{C}$.

Kombinert EBSD+in-situ strekktester ble utført inne i et tradisjonelt SEM. Metoden ble valgt for å avsløre forskjeller mellom blokkene når det kommer til forskjeller i mikrostrukturens utseende og deformasjonsmekanismer. Før arbeidet startet var det rapportert fra SINTEF Raufoss Manufacturing at blokk T600 hadde bedre bruddforlengelse i deponeringsretningen enn T200, det vil si: 8% sammenlignet med 5%. Men dette var generelt sett lavere enn i byggeretningen der 10% bruddforlengelse var rapportert. Hovedvekten i arbeidet lå defor på å forklare hva forskjellene i bruddforlengelse kan skyldes ut ifra mikrostrukturanalyser med overnevnte metode. Tilleggsundersøkelser med optisk lysmikroskop ble også utført for å avsløre makrodeformasjoner.

Undersøkelsene startet med en omfattende makroetsing i ulike plan av blokkene for å avsløre eventuelle forskjeller i størkningsstrukturen mellom blokkene. Dette avslørte et 3D-bilde av størkningsstrukturen bestående av tidligere β -fase søylekorn. Målinger av søylekornenes form og størrelse viste få om ingen forskjeller mellom blokken. Senere ble EBSD benyttet til å sammenligne tykkelse på primær α -fase langsmed tidligere β -søylekornrensere for de to blokkene for prøver tatt ut i senter. Målingene viste også her små forskjeller. Fra dette ble det konkludert med at de ulike IT-ene fører til små forskjeller i størkningstrukturen og mengden primær α -fase i senter av blokkene.

Videre ble EBSD+in-situ undersøkelsene utført for strekkstaver tatt ut parallelt med deponeringsretningen. Strekkretning var også parallelt med deponeringsretningen. Det ble observert at strekkstavene i T200 var tatt ut høyere oppe i blokken, noe som ga en finere mikrostruktur grunnet den raskere avkjølingshastigheten der. Videre ble det observert at T200 strekkstaver også inneholdt to deponeringslag i motsetning til T600 som bare hadde en. Dette gjorde en direkte sammenligning vanskeligere. Fra de fire strekkstavene som ble strukket ble likevel følgende konkludert: strekkstaver fra T200 deformerte mer homogent på et makronivå. Tilsvarende var mer aktivitet observert ved tidligere β -kornrensere i strekkstaver fra T600. De større aktiviteten i T600 kan skyldes den saktere avkjølingshastigheten fra makstemperaturen. Saktere avkjølingshastighet vil gi mindre β -korn dekorert med mer primær α -fase langsmed β -kornrensene. Den ofte rapporterte mismatchen mellom myke og harde HCP-korn i titanlegeringer var også observert. Tilsynelatende spilte

også formen og orienteringene til disse en viktig rolle for deformasjonen. Sprekker som vokste frem langsmed β -korngrenser var alltid lokalisert på den side som ikke har Burgers Orienterings-sammenheng. Den lamellære mikrostrukturen i materialet virker også å være forholdsvis effektiv til å stoppe sprekker fra å vokse videre, grunnet den stadig endrede vekstretningen av platene.

Dette arbeidet har også avdekket mikrostrukturene i overgangssonen mellom substratplaten og det første deponerte laget. Mikrostrukturen der utvikler seg fra å være bimodal, til equiakset med små mengder primær α -fase, til tidlig stadier av søylekorn. De første søylekornene er små iforhold til høyere opp i blokken. De består også av veldig små mengder primær α -fase. Den lamellære strukturen kan likevel dannes i nærhet til substratplaten.

List of Abbreviations

DMD	Direct Metal Deposition
EBS	Electron BackScatter Diffraction
SEM	Scanning Electron Microscope
ALM	Additive Layer Manufacturing
NTiC	Norsk Titanium Components
HAZ	Heat affected Zone
IT	Interpass Temperature
BSE	BackScatter Electrons
SE	Secondary Electrons
EBSP	Electron BackScatter Pattern
HCP	Hexagonal Close Packed
BCC	Body Centered Cubic
OR	Orientation Relationship
BOR	Burgers Orientation Relationship
CCD	Charge Coupled Device
CAD	Computer Aided Design
ROI	Region of Interest
OIM	Orientation Imaging Microstructure
CI	Confidence Index
IQ	Image Quality
IPF	Inverse Pole Figure
PF	Pole Figure
XrD	X-ray Diffraction
CRSS	Critical Resolved Shear Stress
UTS	Ultimate Tensile Strength
YS	Yield Strength

Contents

Preface	I
Acknowledgements	III
Abstract	V
Sammendrag	VIII
List of Abbreviations	XI
1 Introduction	1
1.1 Scope of the Work	2
2 Theory	3
2.1 The Respective Ti6Al4V-alloy	3
2.1.1 Duplex Morphologies	3
2.2 Atomic Configurations	6
2.3 Equilibrium Phase Diagrams	7
2.3.1 The Ti-Al Alloy System	7
2.3.2 The Ti-V Alloy System	9
2.3.3 The Ti6Al4V-Alloy System	11
2.4 Direct Metal Deposition	12
2.4.1 Interpass Temperature Process Parameter	14
2.5 Solidification of the DMD-material	15
2.6 Solid State Phase Transformations	16
2.6.1 Grain Boundary α -phase	17
2.6.2 α -Colonies and Basketweave Microstructure	19
2.7 Effect of Cooling Rates on Solid State Phase Transformations	21
2.8 Mechanical Properties	23
2.8.1 Critical Resolved Shear Stress and Schmid's Law	23
2.8.2 HCP-Slip Systems	24
2.8.3 BCC-Slip Systems	25
2.9 Microstructural Effects	28
2.9.1 Dislocation Mobility	28
2.9.2 Effect of Globular α -Phase on Ductility	32
2.10 The EBSD-Technique	34
2.10.1 Effect of Probe Current	35
2.11 TSL OIM Data Collection 5.32 Indexing Software	39
2.12 TSL OIM Analysis 6.1 Software	40
2.12.1 Quality Parameters of EBSD-map	40
3 Materials	42
3.0.2 Interpass Temperature	43
3.0.3 Chemical Compositions	43

3.0.4	Reported Differences in Microstructure	44
3.0.5	Mechanical Properties	45
3.0.6	Stress Relief	46
3.0.7	Disposition of the Material	46
4	Experimental	47
4.1	Sample Preparation for General Metallographic and EBSD-Analysis	47
4.1.1	Cutting	47
4.1.2	Grinding	47
4.1.3	Polishing	48
4.1.4	Etching and Macroetching	48
4.1.5	Cleaning	49
4.1.6	Ion Sputtering	49
4.2	Specimen Sampling of In-situ Tensile Specimens	50
4.2.1	Preparation of In-situ Tensile Specimens	52
4.3	SEMs	53
4.4	In-situ Tensile Equipment set-up	55
4.4.1	In-situ Tensile Stage	56
4.5	Indication of Phases by XrD-Analysis	57
5	Results	58
5.1	Macroetched Samples	58
5.2	EBSD+In-situ Tensile Results	59
5.2.1	Important Observations from the In-situ Tensile Tests	60
5.3	Deformation at Macro Level	61
5.4	Deformation at Micro Level	69
5.4.1	S1T200	69
5.4.2	S2T200	72
5.4.3	S1T600	74
5.4.4	S2T600	76
5.5	Tensile Curves	78
5.6	Interface Region between Substrate Plate and DMD-Block	79
5.7	Grain Boundary α -Distribution along prior β -Grains	83
5.8	Effect of Ion Milling on Quality Parameters of the EBSD-map	84
5.9	Effect of Probe Current on Quality Parameters of the EBSD-map	88
5.10	Summary of Quality Parameters of the EBSD-map	90
5.11	Phases Indicated by XrD-Analysis	91
5.11.1	Indexing with Ti_3Al -Phase	92
5.12	Fracture Surface	93
6	Discussion	94
6.1	Deformation at Macro Level	94
6.1.1	Slip Bands in T200 vs. T600	96
6.2	Deformation at Micro Level	97
6.2.1	Deformation in globular α -phase	97
6.2.2	Critical Resolved Shear Stress in α -Colony	98

6.2.3	Dominating Slip Systems Indicated by Taylor Factor Maps	100
6.3	Tensile Curves	101
6.4	Identification of Burgers Orientation Relationship at Prior β -Grain Boundaries	102
6.5	Texture in Columnar β -Grains	103
6.6	Contributions from Hydrocarbon Deposition on Quality Parameters of the EBSD-maps	105
6.7	Calculation of Spatial Resolution	106
6.8	XrD-Analysis and Indexing of Ti_3Al -Phase	106
6.9	Effect of Deformation on Quality Parameters of the EBSD-map	107
6.10	Fraction β -Phase	108
6.11	Fracture Surface	109
7	Conclusion	111
8	Further Work	112
9	References	113
10	Appendices	117
10.1	Critical Resolved Shear Stress for single crystals	117
10.2	Spatial Resolution vs. Probe Current	118
10.3	Stress Relief	119
10.4	Macroetched Samples	120
10.5	SEM-Procedures before EBSD-Investigations	121
10.6	Frequently used CCD-Camera Settings in NORDIF 1.4.0	122
10.7	Hough Transformation Settings	123
10.8	Camera Length for the two SEMs	123
10.9	Formula for Confidence Index	123
10.10	Thickness of primary α -phase in block T200 and T600	124
10.11	Interface Region between Substrate Plate and Block	125
10.12	Procedure to Create Taylor Factor Map	126
10.13	Summary of Quality Parameters of the EBSD-maps	127
10.13.1	XrD-Spectras	131
10.14	Buy-to-fly ratio - DMD Compared to Machining	133
10.15	Comparison of Mechanical Properties between Lamellar, Bimodal and Equiaxed Microstructures	134
10.16	Machining of Titanium	135
10.17	Tensile Properties of Laser-aided Deposited Ti6Al4V after Different Heat Treatments	136
10.18	Methods for Improving Mechanical Properties of the DMD-Material	137
10.19	Fusion Line between Single String and Substrate Plate	138
10.20	Pole Figures	139

1 Introduction

The connection between the process parameters of the DMD-process and the final mechanical properties of the blocks still needs research. The DMD-process is only 9 years old and limited research has been published so far on the link between production parameters and mechanical properties. This report will only consider the Interpass Temperature (IT) parameter and its influence on microstructure and deformation mechanisms. IT does not influence the bead geometry in contrast to the other parameters in the process, but the production efficiency have an indirect dependency on the IT. However, throughout this work it is the metallurgical aspects regarding implementing different ITs in the production parameters which is the motivation. The strength of the material is for instance expected to increase with lower IT.

A challenge with the DMD-process is the low ductility observed in the final blocks after the process and the sometimes different mechanical properties relative to the deposition direction. For NTiC to deliver products to the aerospace industry, the ductility of the products is desired to improve to meet the requirements to mechanical properties set by this industry. In this industry ductility is of concern since it offer a margin of safety for critical applications. Improved ductility is for instance said to be one of the most important material-properties determining fatigue life [1]. The DMD-process have a large potential in this industry. For instance is the type of microstructure that normally forms after the DMD-process considered as the most crack propagation resistant microstructure available for the Ti6Al4V-alloy. The crack propagation resistance is the most important mechanical property requirement determining the service time between each inspection of an aircraft, ch. 5.5 [2]. The investigated Ti6Al4V-alloy also represent 50% of the titanium market [3], where very large quantities go into the aerospace industry.

Traditionally are titanium components machined from forged plates. But machining lead to large fractions of wastage material, especially for complex geometries. For instance can the production of a stiffening panel for an airplane with traditional methods produce 80% wastage after machining. The Direct Metal Deposition technology can produce the same component with only 10% material wastage. See Figure 84 in appendix for comparison of initial and final weight of the panel.

Recently did Additive Layer Manufacturing (ALM) achieve attention in the largest technical magazine in Norway, as a very promising production method. The major advantages was said to be large materials savings and reduced need for machining. Others have even predicted that ALM can contribute to a new industrial revolution which may be supplementary to machining [4]. This is especially interesting when considering that titanium is one of the most difficult and expensive materials to machine ch. 10 [5]. In spite of this, machining is still very often the last manufacturing step of titanium products today. The DMD-process is called a game-changer because of the the new approach to manufacture final titanium products.

1.1 Scope of the Work

The reduced strain properties in the deposition direction of DMD-blocks was only partly explained in previous work by the orientation of β -grains relative to the tensile direction, Martin Mathisen [6]. Specimens tensiled in the deposition direction contains a larger volume of prior β -grain boundaries where failures can occur more frequently compared to tensile specimens tensiled in the building direction. The differences in ductility between the blocks and the reduced strain properties in the deposition direction is the motivation for this work. This work continues in the same direction as previous work with the combined EBSD+in-situ investigations. What distinguishes this work from the previous is the focus on connecting IT to microstructures and deformation mechanisms, and finally present a discussion on the impaired ductility.

2 Theory

The DMD-process is only a 9 years old production technology applied on a relatively old Ti6Al4V-alloy system developed in the 1950s, Lütjering [2]. Because ALM and DMD-processes are relatively new science, limited information is published on the connection between microstructure, mechanical properties and production parameters. This theory section focuses on to summarize the available information from published sources. However, welding and laser deposition of Ti6Al4V have many similarities to the DMD-process and are used as supplementary information. The first sections i.e. 2.1-2.3.3 summarize the phases and microstructures present in the Ti6Al4V-alloy system. The next sections 2.4-2.7, focus on how this material behaves when it is welded or deposited into layers in addition to present the most important aspects regarding the IT. Towards the end of the theory i.e. sections 2.8-2.9.2, the focus turns to connect the mechanical properties to microstructures observed in the Ti6Al4V-material after deposition.

2.1 The Respective Ti6Al4V-alloy

Today the Ti6Al4V-alloy system is the most widely used titanium alloy in the world, ch. 1.3 Lütjering [2]. The explanation for why this material is so widely used is because of the material's good combination of properties, and the well-responding effects on thermo-mechanical treatments to improve mechanical properties. Some of its popular properties are for instance combinations of: high specific strength, weldability, the alloy can maintain high strength and good fatigue properties at elevated temperatures, suitable for cryogenic conditions, and its excellent corrosion resistance in many critical environments. However, there are other titanium alloys which are more specialized than Ti6Al4V. For instance have some β -alloys higher strengths. The Ti6Al4V-alloy was developed with one purpose, performing well under many conditions. Because of this the Ti6Al4V-alloy is called the work-horse among titanium alloys.

2.1.1 Duplex Morphologies

The alloy is referred to as a duplex alloy consisting of a combination of two phases, the α - and β -phases. Dependent on the combination of heat treatment and manufacturing processes involved, can different ratios of the phases be obtained. See section 2.3.3 for reported volume fractions of the β -phase. Duplex alloys are generally developed with the idea of combining the best properties of two phases. A description of the atomic configurations of the two phases is presented in section 2.2. And a discussion of the differences in mechanical properties can be found in section 2.8.

The microstructures in Ti6Al4V-alloys obtained after various thermo-mechanical treatments are generally divided into three different groups: lamellar platelets, equiaxed and bimodal. See Figure 1 below for illustration. The lamellar microstructure in a) is of most importance for this study, since its frequently observed in the DMD-material. However, a mixture of the lamellar and bimodal microstructures is expected in the interface region between the substrate plate and the DMD-block.

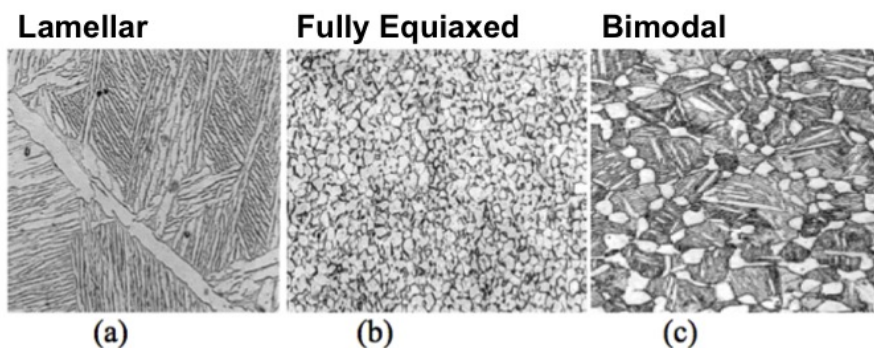


Figure 1: Images of the three possible microstructures in the Ti6Al4V-alloy. a) Lamellar, b) Fully equiaxed microstructure consisting of primary α and retained β (close to equilibrium microstructure), c) The bimodal microstructure consisting of α -islands surrounded by colonies of alternating $\alpha + \beta$ plates [7].

The literature generally reports higher yield strength (YS), better ductility i.e. elongation and reduction in area, higher fatigue crack resistance, and slower fatigue-crack propagation rates for the bimodal microstructures than for a lamellar microstructure. Therefore is the bimodal microstructure often the choice for very demanding applications such as fan blades, compressor blades and disks in turbine engines because of the improved properties, Lütjering [2]. However, the lamellar microstructure generally perform better creep properties and higher fracture toughness than the other two. Table 38 in the appendix compare the different mechanical properties of the microstructures.

The lamellar microstructure may seem chaotic at first, but in reality it is a very complex microstructure which is governed by phase transformation relationships called orientation relationships (OR). In short this mean there are some crystallographic orientation between the phases which are preferred orientations and readily forms chemical bonds during the phase transformation. These orientation tend to outgrow other less dominating crystallographic orientations both during solidification of the material and during solid state transformations at lower temperatures. The OR present in Ti6Al4V will be discussed in further details in section 2.6.1.

By rapid cooling (410-525 °C/s) of the Ti6Al4V-alloy from the β -phase region of the phase diagram a fourth microstructure can be observed, the martensite microstructure. The strength gained by this martensite microstructure cannot be compared to what is observed in steel. The explanation for this is that oxygen does not distort the hexagonal structure to the same degree as the tetragonal distortion by carbon in ferrous martensite [2]. However, the strength gained in both YS and ultimate tensile strength (UTS) is significantly increased compared to the strength gained by reducing width and length of lamellas in lamellar microstructures [8]. Martensite is not a desired microstructure in the DMD-material, because it reduces the ductility of the material. This is in contrast to NTiCs focus to increase the ductility of the DMD-blocks. Hence, the martensite structure will only be of minor interest throughout this report.

2.2 Atomic Configurations

What recognizes a phase is a relatively uniform distribution of chemical and physical properties in a restricted region of the microstructure. The Ti6Al4V-alloy consist of two different phases with very different chemical- and physical properties. The wide range of properties origins from the combination of properties given by the atomic configurations or unit cells. The α -phase is referred to as a HCP atomic configuration (hexagonal closed packed), while the β -phase have a BCC atomic configuration (body centered cubic). Their unit cells are given in Figure 2 for unalloyed conditions. In reality, the two unit cells can solve large concentrations of different elements at interstitial and substitutional positions in the lattices. The solubilities of the main alloying elements will be discussed in section 2.3 concerning the equilibrium phase diagrams. The BCC configuration does not normally exist at room temperature such as the HCP configuration. It has been stabilized to room temperature by a sufficiently large amount of β -stabilizers, for instance V in this case. This is done by purpose to give some desired properties to the alloy, for instance workability. See section 2.3.2 for more contribution of V to the alloy. These two atomic configurations is the foundation for the mechanical properties we observe in the DMD-material since they behave differently during tensile tests. See section 10.1 for deformation mechanisms and slip systems of the two phases.

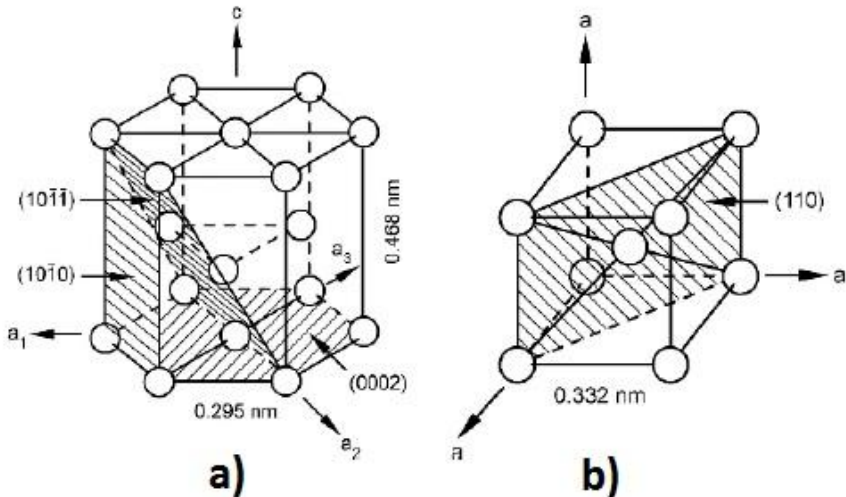


Figure 2: Figure a) the HCP atomic configuration.
Figure b) the BCC atomic configuration (G. Lütjering, James C. Williams ch. 2.2)[2].

2.3 Equilibrium Phase Diagrams

Generally, when alloying elements are added to titanium two effects can be observed in the phase diagram dependent on the solubility of the elements. Large solubility of an element can be seen as an expansion of a phase-region, while a small solubility contracts a region in the phase diagram. The other effect is the effect of different solubilities on the transition regime α/β , given by the β -transus line in the phase diagram. Al tend to elevate this line for increasing concentrations as seen in the Ti-Al phase diagram in Figure 3, while V tend to lower it. See Ti-V phase diagram in Figure 5. In general, elements which are closely located in the periodic table have a large solid solubility and subsequently also a large phase stabilizing effect, which is according to Hume and Rothery's work.

2.3.1 The Ti-Al Alloy System

Al is the only common metallic element rising the β -transus line and at the same time having large solubilities in both α - and β -phases. Other α -stabilizers which also increase the β -transus temperature with increasing concentrations are: O, N and C. Lütjering ch. 2.5 [2]. Note that the DMD-material also contains considerable amounts of these interstitial elements.

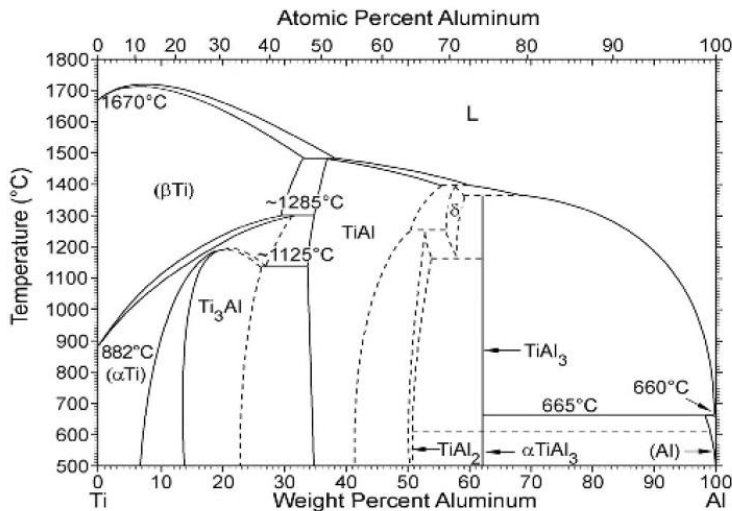


Figure 3: Binary phase diagram of Ti-Al system [2]. Of special concern for mechanical properties is the formation of Ti₃Al-phase.

Intermetallic Titanium Aluminides

Ti_3Al -precipitates can form at aging temperatures of 500-600°C for Al concentration as low as 5wt%, see Ti-Al phase diagram in Figure 3. Ti_3Al is an intermetallic phase which is known to promote coarse planar glide on prismatic planes [9]. The Al-content in commercial titanium alloys is often limited to <6wt% to avoid widespread precipitation of the Ti_3Al -phase and the impaired mechanical properties. The phase can also act as a stress-riser and crack-initiation points because of its coherent relationship with the matrix structure, i.e. easy slip transfer [2]. O is an element which is known to shift the solubility limit of Al in α -phase to lower values, thus enhancing the likelihood of Ti_3Al -formation ch. 2.8.1 [2].

The repeated heating during the DMD-process by adding new layers will temper the material in previous layers and increase the substitutional diffusion rates. This repeated heating will contribute to make this phase more likely to form. The phase is dependent on equilibrium conditions and on diffusion of large substitutional elements which diffuses relatively slow. The hexagonal super-lattice of the phase can be seen in Figure 4 below. The phase belongs to the P63/mmc space group and have a density of 4.23g/cm³. As a comparison to the lattice parameters of Al-rich α -phase, the Ti_3Al 's unit cell has approximately twice the size. The lattice parameters can be found in section 4.5 experimental part. In the experimental part of the report was this phase attempted to be identified with both EBSD and XrD.

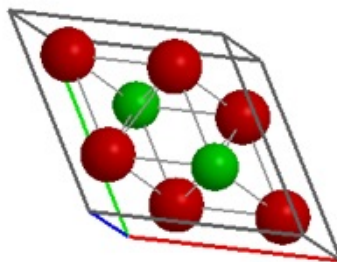


Figure 4: The hexagonal unit cell of the Ti_3Al -phase. Green atoms: Al, Red atoms: Ti.

Increased Al-content can also be an advantage for titanium alloys used in aerospace applications as it decreases the overall weight of the alloy. For instance could titanium alloys be the material of choice for even more application in the aerospace if the weight could be reduced compared to materials such as composites and aluminum alloys.

2.3.2 The Ti-V Alloy System

The β -stabilizers can be divided into isomorphous and eutectoid forming elements, depending on the binary phase diagrams they forms. The binary system Ti-V, presented in Figure 5 below is an isomorphous type. The most widely used β -stabilizers beside V, are Mo and Nb. All three elements are transition elements. Sufficient concentrations of these elements can stabilize the β -phase to room temperature. See section 2.3.3 for the expected β -content in the DMD-material. From the slopes of the solidus lines in the two-phase region below 948K, it can be seen that α -phase is depleted on V, while β is enriched. That means V partitions to the β -phase during cooling, in contrast to Al which have large solubilities in both phases. Lütjering ch. 2.5 [2].

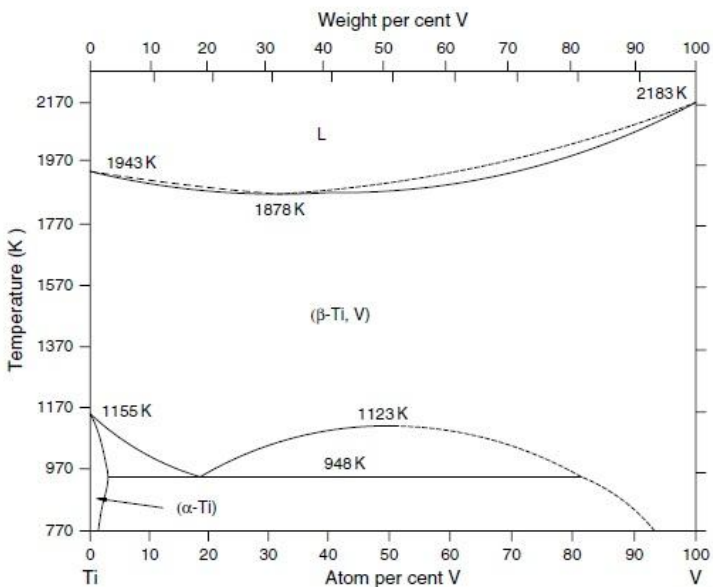


Figure 5: Binary phase diagram of Ti-V system. (Temperature is given in Kelvin and composition in atomic percent) [10].

Contributions from V-additions to the alloy

The hardening rate by solid solution strengthening by V-additions is about 6kg/mm^2 per at% which is a smaller contribution than both α -stabilizers and interstitial elements. As a comparison the hardening rate of Al is 15kg/mm^2 per at%, while nitrogen have a hardening rate of 239kg/mm^2 per at% according to Table 8.2 ch. 12.1 [11]. The explanation for this is the lower difference in atomic radius between Ti and V, than for instance interstitial elements and Ti. For this reason V is regarded as a β -stabilizers rather than a solid-solution strengthener.

Reported improvements to titanium alloys by V-additions are: easier workability at elevated temperatures because of ductile β -phase. For V-concentrations $>4\%$ can the alloy also be significantly strengthened by heat treatment [12].

2.3.3 The Ti6Al4V-Alloy System

For slow cooling rates the Ti6Al4V-alloy can contain up to about 10vol% β -phase at room temperature dependent on the heat treatment and interstitial contents [3]. The ternary phase diagram in Figure 6 indicate 15vol% at 800°C ch. 2.7 [2]. The overall cooling rate of the DMD-material was simulated at NTiC to be 10°C/s, which is relatively slow and may allow close to equilibrium distributions of alloying elements.

The β -transus for the Ti6Al4V-alloy is reported to be 995°C according to Table 2.6 Lütjering [2]. Section 2.7 discuss the Continuous Cooling Temperature (CCT) diagram for the Ti6Al4V-alloy and which phases that can be formed for non-equilibrium cooling rates at the intersection of β -transus. Local differences in V-concentration can retain some β -phase in the most V-rich locations. V >15% is needed for a completely stabilized β -alloy. The locations where its likely to find retained β -phase are between α -lamellas in colonies and α -lamellas in the basketweave microstructure. These two microstructures are presented in section 2.6.2. However, from previous work was very small fractions of retained β -phase detected in the DMD-material with the EBSD-technique i.e. $\sim 1\%$. The phase seems to be very finely dispersed in very distinct small volumes [6].

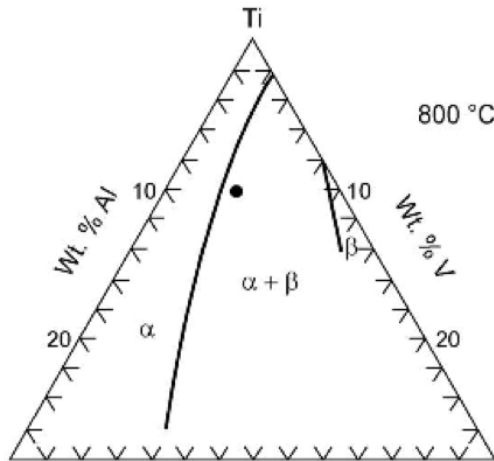


Figure 6: The titanium-rich corner of the ternary Ti6Al4V-alloy system. The solid point indicate the position of the respective alloy. This isothermal section of the ternary phase diagram at 800°C, indicates a small fraction β -phase which can be retained to room temperature [2].

2.4 Direct Metal Deposition

Figure 7 illustrate how a plasma torch can deposit numerous layers of titanium material onto a substrate plate. The fire feeder is where the desired titanium wire are guided into the plasma arc. Instead of a gas inlet, have NTiC developed small "houses" where both the deposition equipment and substrate plate are placed in an inert gas atmosphere. This enables production of larger and more complex geometries than the curtains used in the case of Figure 7. It also provide good shielding to avoid titanium to react with molecules in the atmosphere. The three-axis manipulator control the movement of the torch. NTiC use an robotic arm from ABB instructed by a CAD-software to do this operation.

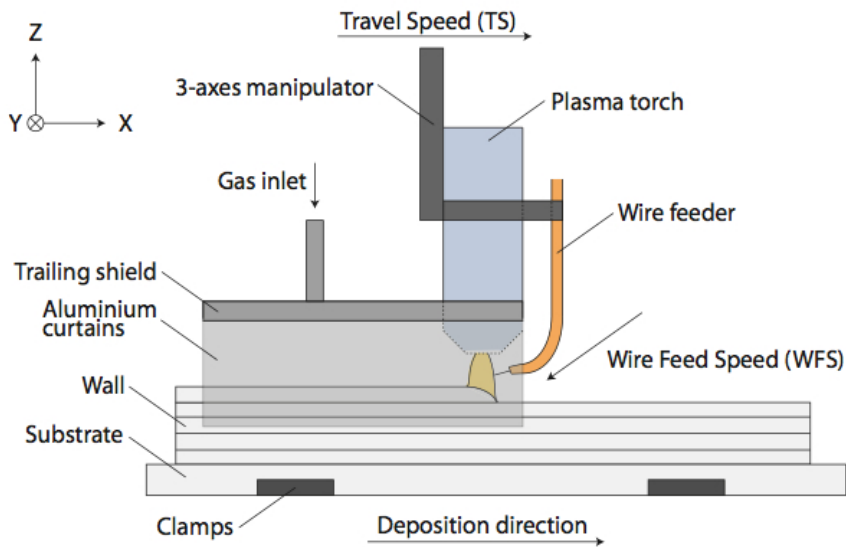


Figure 7: A sketch of the different parts in a DMD set-up. Figure reference: [13].

By fusing layers on top of each other in Z-direction and parallel to each other in the Y-direction can metallic bonds be formed between the layers and eventually a 3D-shape be formed. The welding-approach have very few limitations with respect to geometries. The block can also be built up very close to the final shape of the component. This reduces the need for machining. Compared to directly machining from a forged or casted titanium, this have a potential of large materials savings. See section 10.14 in the appendix for comparison between the DMD-process and the traditional way to produce a component.

The DMD-process can be described as an ALM-process or a so called 3D-printing method. The fundamental idea of fusing layers of the desired material on top of each other is not unique for the DMD-process. There are several other techniques which perform the same operations, but the heat source used is mainly what distinguishes them. The reduced need for machining is a major advantage for the DMD-process because titanium is a difficult material to machine. See section 10.16 for why titanium is difficult to machine.

Figure 8 illustrate a piece of hollow cylinder made by a DMD- process. The deposited layers can be seen as horizontal lines in the image. Fused titanium metal transferred through the plasma to the component surface, remelt some of the previous deposited layers and ensure strong metallic bonds between each layer. The solidification structure can also be seen as diagonal lines. In reality they are large prior β -grains, that normally are weakly tilted towards the deposition direction. These grains can measure up to 30mm in length, and 10mm in width. The presence of these grains are fundamental for the microstructures observed in the DMD-material. The solid state phase transformations that take place at a later stage of the solidification will be located at such grain boundaries. See section 2.6 for solid state phase transformations.

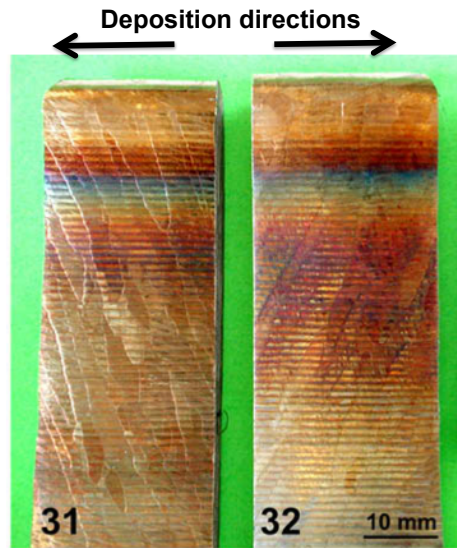


Figure 8: The image illustrate that the β -grains "follow" the deposition direction. The yellowish colour are due to oxide formation on the surface during depositon. This is a result of poor shielding-gas. Argon-gas is for instance used by NTiC. However, it is only considered as a cosmetic fault not influencing the mechanical properties of the material [14].

2.4.1 Interpass Temperature Process Parameter

N. Hoyer et al. [15] investigated how common process parameters in a gas tungsten arc-welding process influence the final weld deposit geometry. The parameters they investigated were different combinations of: IT, arc length, arc current, travel speed and wire feed speed ratio. From initial statistical tests of geometry measurements the IT was said to have a negligible effect on the thickness, height and surface roughness of the multi-layer weld deposits. The IT was then not considered as a factor in all subsequent analysis and modelling. Their final conclusion was: «the average thickness of the wall type deposit is primarily a function of arc current and travel speed while build-up height is chiefly related to wire feed speed, and hence deposition rate.» The value of the IT is therefore mainly of interest for the production efficiency and for mechanical properties.

ITs Influence on Production Efficiency

The IT has a direct influence on the production time of a DMD-block. To reach a desired IT a given waiting time must be implemented between each pass in the CAD-software. The formula below presents a very simplified relationship for the different time-consuming steps in the production.

$$Production\ time = N \cdot \frac{L}{DS} + WT \quad (1)$$

Where N=number of layers, L=length of the block, DS=deposition speed, WT=waiting time which is a function of the cooling rate of the respective Ti6Al4V-alloy.

When comparing the production time of block T200 and T600, the difference lies in the waiting time because the deposition speed and length of the blocks were the same.

2.5 Solidification of the DMD-material

This section focuses on what happens with the deposited material in the two-phase region of the phase-diagram between the liquidus-temperature of 1670°C and the β -transus at 995°C.

Epitaxial Growth of Columnar β -grains

Epitaxial solidification is the initial solidification in the weld or deposition pool at the interface between the liquid and solid metal. The coarsened HAZ at the fusion line act as nuclei for β -crystals in the solidifying weld metal. The crystallographic orientation of the β -grains is inherited from the solid surface in this region. According to [16] β -grains often have a preferential direction of growth corresponding to $\langle 100 \rangle$, as illustrated in Figure 9. The grains having $\langle 100 \rangle$ orientation will quickly outgrow those grains with less favourable orientations. The explanation for why this direction is favourable is that rearrangement of atoms occurs more readily in the directions with low packing density [17]. Epitaxial growth is also recognized with a growing crystal in the weld pool which have the same crystal orientation as the crystal it grows from.

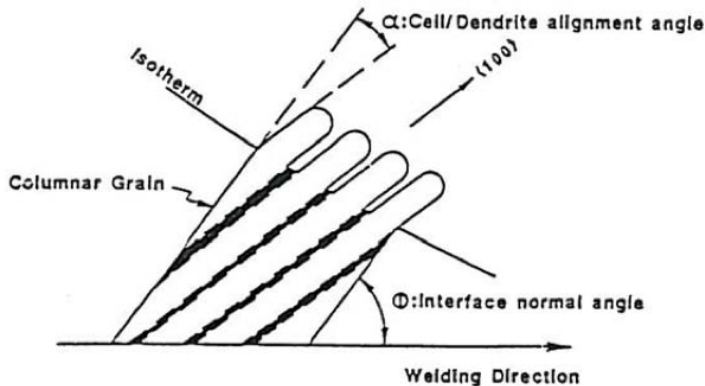


Figure 9: Columnar β -grains growing favourable in $\langle 100 \rangle$ direction from the liquid-solid interface in the weld pool. From Grong 1997 [17]

For the case of deposition technologies like DMD, columnar prior β -grains can be observed approximately 45° towards the travel direction of the electrode, as indicated with the angle ϕ in Figure 9. The growth direction is along the steepest temperature gradients due to a more effective heat extraction through the substrate plate than through convection and radiation (despite titanium is a poor conductor of heat).

2.6 Solid State Phase Transformations

The most important parameter to determine the characteristic features of the lamellar microstructure observed in the DMD-material, is the cooling rate from the β -region ch. 5 Lütjering [2]. The lamellar microstructures formed below β -transus will be addressed in the following sections.

Substructures in the DMD-material

Figure 10 summarizes the different microstructures that should be distinguished between in the DMD-material. This section is added to briefly introduce the different microstructures, while the following sections give more in-depth information on how they are forming during solidification. It can be seen from Figure 10 that the β -grains are weakly tilted along the deposition direction X, as a result of epitaxial growth along the steepest temperature gradient, corresponding to the direction $\langle 100 \rangle$.

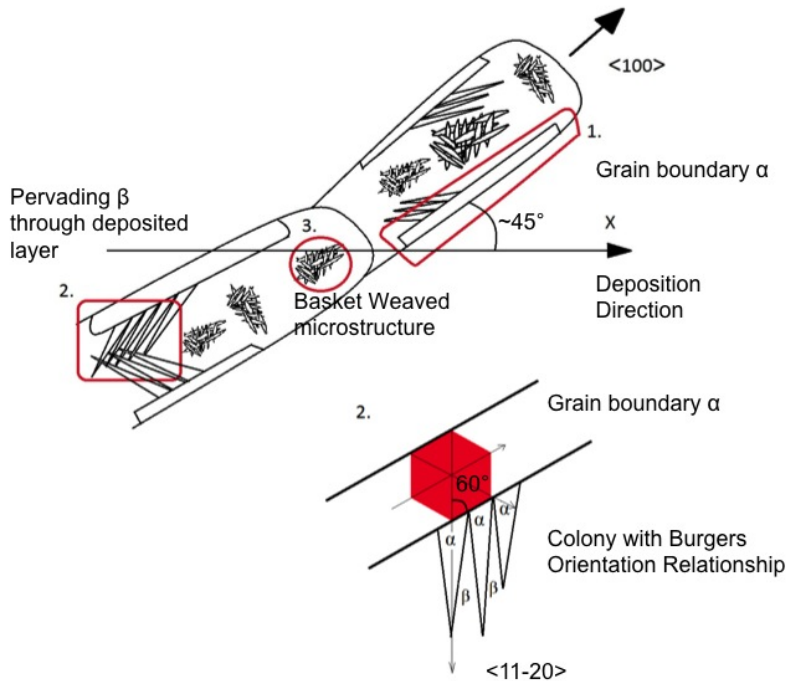


Figure 10: An illustration of the different types of microstructures observed in DMD-material. Figure reference: Lars Eriksen. The idea behind the figure was from the references; Figure 12 in Lütjering [2] and Figure 13 in [13].

The β -grains also tend to pervade the previous deposited layers, and can inherit approximately the same crystallographic orientation as the β -grains in previous layers. Two related β -grains are indicated across the horizontal line (deposition direction X) in the figure.

At position 1, the first α -phase appear during cooling. Further, this already formed grain boundary α -phase act as nucleation sites for colonies which strictly follow BOR, illustrated in position 2. At the center of the β -grains in position 3, the α -phase have a more chaotic appearance often referred to as the basketweave microstructure.

2.6.1 Grain Boundary α -phase

During cooling of Ti6Al4V-alloys, the first α -phase will prefer to nucleate at prior β -grain boundaries right below the β -transus temperature. The first α -phase forms here because of the lower internal energy required to nucleate at β -grain boundaries and the high diffusional pathways due to a less dense crystal lattice at such regions of the microstructure. To what extent the primary α -phase continuous to grow depends on the cooling rates. The thickness of the primary α -phase decreases with increasing cooling rates but is still present at quenching conditions when martensite is the dominating microstructure. For very slow cooling rates the primary α -phase have approximately the same width as the plates in the colonies ch. 5 Lütjering [2].

Upon further cooling will already nucleated primary α -phase start to grow as plates inside the β -grains in so-called α -colonies. The α -colonies have the same crystallographic orientation as the grain boundary α they grows from. See section 2.6.2 for more description of the α -colony structure. The amount of of grain boundary α is important to discuss, because it can be detrimental for mechanical properties. For instance have cleavage fractures been observed more frequently for higher fractions grain boundary. According to page 185 [18] can premature cracks initiate in such locations of the microstructure. The primary α -phase at grain boundaries can be coarsened by different isothermal heat treatments in the two-phase region of the phase diagram, 700-900°C [19]. Since the DMD-material is repeatedly heated a d may spend sufficient time in the two phase-region this isothermal heat treatment temperatures is relevant for the material. The impaired mechanical properties from coarse primary α -phase on grain boundaries is discussed in more details in section 2.9.

Burgers Orientation Relationship at prior β -Grain Boundaries

An orientation relationship (OR) can be described as how the atoms in the interface between a parent and a product phase are related in the moving transformation front. The OR in $\alpha+\beta$ titanium alloys corresponds to the most densely packed planes and direction in the BCC and HCP lattice are parallel, see Figure 11 below. This OR is named Burgers Orientation Relationship (BOR). BOR is closely obeyed for both diffusional growth of the α -phase and the martensite formation ch. 2.6 Lütjering [2].

Figure 11 below illustrate the BOR at β -grain boundaries. It is not possible for the primary α -phase to maintain BOR with two adjacent β -grains. The α -phase therefore "chooses" an orientation which allows it to have a small as possible deviation from BOR with the other grain [20]. The side having a non-BOR will often have α -phase with ledges [21].

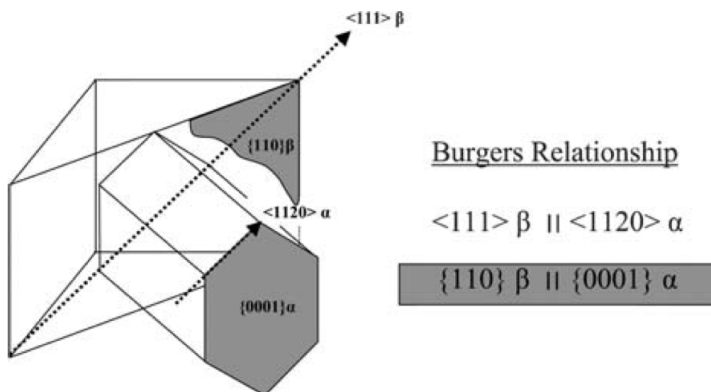


Figure 11: BOR at the interface between columnar β -grains and primary α -phase. Figure reference: [22].

Dependent on the titanium material under consideration are cooled or heated across the β -transus line, there are a number of different variants of BOR presented above that can form. The variants involves different combinations of families of planes and directions given in Figure 11 above. The BCC to HCP transformation during cooling involves one out of 12 variants, while the HCP to BCC during heating result in one out of 6 possible variants. Larger β -grains before cooling also increase the probability of observing more variants. BOR give the minimum distortion and rotation of the lattice vectors of the unit cells in HCP and BCC [10]. Because of the adherence to BOR combined with the lower symmetry of the HCP-unit cell than the BCC-unit cell, $\alpha+\beta$ titanium alloys are known to have a high resistance to recrystallization [23]. For the DMD-material this implies that higher temperatures is needed to activate microstructural changes during deposition and repeated heating.

2.6.2 α -Colonies and Basketweave Microstructure

For relatively slow cooling rates will α -lamellas of the same crystallographic variant, also called colonies form. They can nucleate either at primary α -phase on prior β -grain boundaries, directly from the β -grain boundaries or from the component surfaces itself. For faster cooling rates a more chaotic morphology called a basketweave microstructure forms more readily in the interior of the β -grains. The basketweave microstructure consists of multiple variants of α -lamellas clustered in the same region E. Lee et al. [24]. However, in both cases the α -phase strictly follow the very important BOR with the prior β -phase.

Burgers Orientation Relationship between Lamellas

The colonies consist of parallel α -lamellas with retained matrix of V-rich β -phase in between. Their shared growth directions and planes are illustrated in Figure 12. For slow cooling conditions, these colonies can be as large as half the β -grain size ch. 2.6.2 [2].

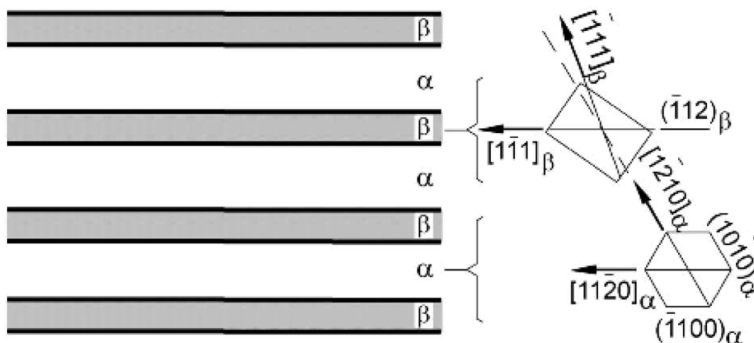


Figure 12: The figure illustrate the BOR inside a α -colony or between plates in the basketweave microstructure [2]. The plates grow with their long direction along former $\{110\}_\beta$ -planes [8].

The α -colony size depends the solution temperature above β -transus and on the cooling rate from the β -region of the phase diagram. Decreased solution temperature above β -transus will give smaller β -grains, and a larger grain boundary area from where colonies can nucleate and grow. Small size of the β -grains will further limit the maximum α -colony size, since the growth will be restricted by other growing colonies from other locations along the grain boundaries [19]. If the cooling rate is increased the size of the colonies and the thickness of the individual α -lamellas will become smaller. This also implies a lower diffusion rate which will lead to slower and shorter growth of the plates into the β -grains. To complete the phase transformation colonies starts to nucleate on each other and in different orientations. The microstructure is now consisting of α -lamellas in which can be

characterized as a basketweave microstructure. Smaller colonies and α -lamellas will generally give improved mechanical properties to the Ti6Al4V-alloy [8]. This is discussed in section 2.9.

Coarseness of the Lamellar Microstructure at Different Positions Inside a Deposited Layer

In Figure 13 can SE-images from different locations inside a deposited layer be seen. The solidification structure growing mainly in the positive Z-direction and the horizontal deposited layers can be seen in image a). The SE-images b)-f) illustrates that the finest platelets is located at the lower part of a deposited layer, e)-f). The explanation for this is the most rapid cooling rates are located there. The previous deposited layers act as a heat sink and rapidly conducts the heat away from the liquid-solid interface in opposite direction to the building direction Z. The finest microstructures are therefore a result of layers which was brought up in the β -region of the phase diagram before cooling.

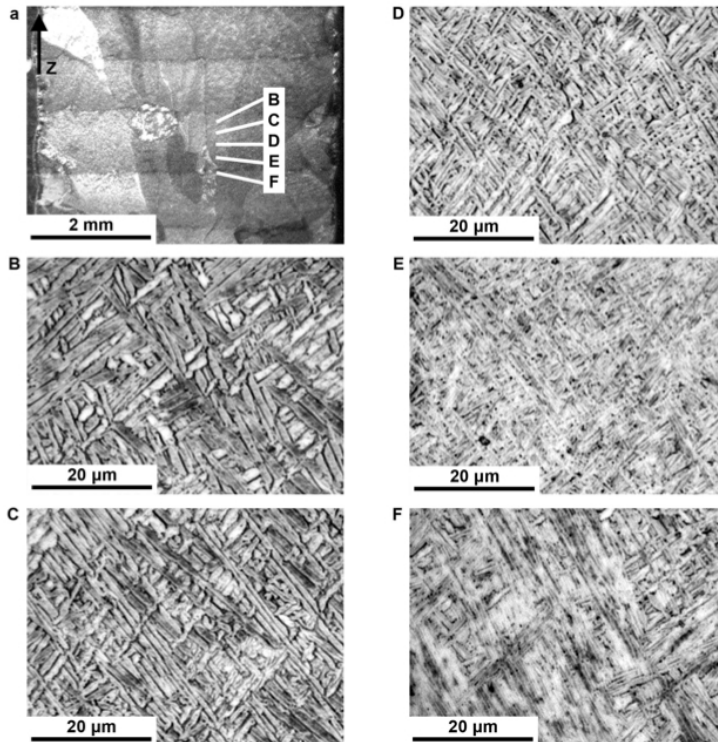


Figure 13: Image a): the macrostructure of a DMD-material as revealed by etching. Image b)-f): microstructures at different locations indicated in a). The differences in α -lamellar size can easily be observed. Reference Image: [13].

At position b), the microstructure is expected to be in the two phase region $\alpha + \beta$. A coarsening of the microstructure can occur because the temperature is high enough to activate substitutional diffusion. If the material is held at this temperature for a sufficient time it can induce significant coarsening of the α -laths. The higher the temperature in the two phase region is the higher diffusional rates can occur and more coarsening can be observed. In the lower temperature regions of the two phase region i.e. position c)-d), no coarsening is observed. The differences in coarseness of the α -lamellas in a given layer is said to appear in the first thermal cycle i.e the next deposited layer. This means that the peak temperature in layer number 2 and 3 is insufficient to cause significant microstructural changes [13].

2.7 Effect of Cooling Rates on Solid State Phase Transformations

The Continuous Cooling Temperature (CCT) diagram for a Ti6Al4V-alloy is given in Figure 14. The diagram illustrates that different configurations of the α -phase can form from the β -phase at different cooling rates. The figure also illustrates that a cooling rate higher than 410°C/s is needed to have a martensitic microstructure given by the symbol α' . Lower cooling rates resulting in a mixed microstructures of α' , massive α i.e. α_m and various morphological forms of diffusion controlled α [25].

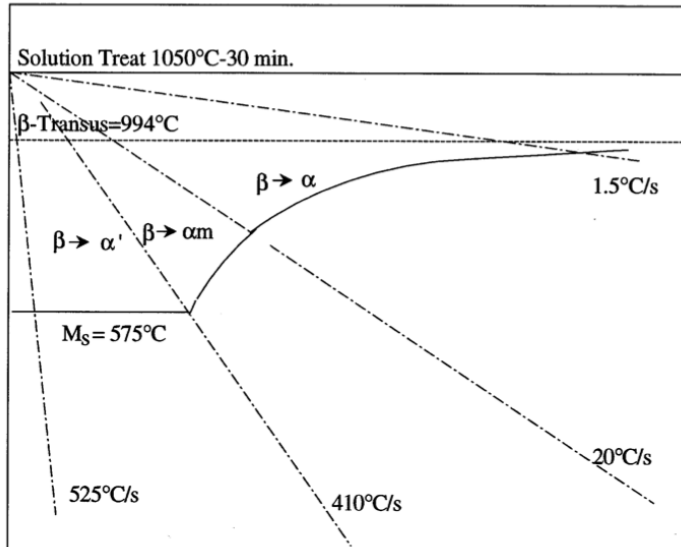


Figure 14: Phase transformation regimes at different cooling rates in alloy Ti-6Al-4V. α' =martensite, α_m ="massive", α =equilibrium. [25].

The fraction of β present in the Ti6Al4V-alloy at room temperature (RT) generally depends on the distribution of the β -stabilizers such as V in the material. There are two conditions which influence V's distribution: the cooling rate and the temperature of the solution treatment before cooling. If the concentration of V is $>15\text{wt}\%$, the β -phase can be retained even at quenching conditions. When the concentration of V is in the range $10 \pm 2\text{wt}\%$ the β -phase will partly retain its BCC-crystal structure and partly decompose into orthorhombic martensite α' for quenching conditions. Higher solution treatment temperatures will lead to smaller V-contents present in the β -phase according to the Ti-V phase diagram. When the material is quenched from high solution temperatures the V-depleted β -phase can transform into hexagonal martensite α'' [19].

2.8 Mechanical Properties

It has been published many models and theories which attempts to explain how polycrystalline materials deform, and how the different grains interacts during deformation e.g. Sachs Model and Taylor Theorem. Because the DMD-material consists of mainly plates, these models are more difficult to apply. Generally, the models are applied to a uniform grain-distribution and equiaxed grains. However, a function in the OIM Analysis 6.0 to plot Taylor-maps were used to analyse polycrystalline areas in the EBSD-results.

Instead of discussing polycrystalline models, the main focus here has been on evaluating the Schmid's law and Critical Resolved Shear Stress (CRSS) for HCP and BCC single-crystals. And for which planes and directions this law are fulfilled. Because Schmid's law is considered as fundamental for materials science it is not included in the report but can be found in section 10.1 of the appendix. However, the interpretation of the law is discussed in the section 2.8.1.

2.8.1 Critical Resolved Shear Stress and Schmid's Law

The Schmid's law are given in section 10.1 appendix. CRSS or τ_r have a maximum value when the angle between the normal to the slip plane and the tensile axis is $\phi=45^\circ$. This also implies that the angle between slip direction and the tensile axis is $\lambda=45^\circ$. CRSS have a minimum value when the tensile axis is normal or parallel to the slip plane i.e. $\phi=90^\circ$ and $\lambda=0^\circ$ and visa versa. Slip will not occur for these extreme orientations since there is no shear stress acting on the slip plane. Crystals close to these orientation tend to fracture rather than slip [26]. When comparing the CRSS-value for different slip systems, the one with the lowest value is the most likely slip system to be operative. The CRSS-value of the different hexagonal slip systems relative to pure α -titanium are given in the last column of Table 15 in section 2.8.2. However, this value varies with temperature and alloying content.

Polycrystals and Deformation Mismatch

The HCP-unit cell is known to have anisotropic properties. Grains oriented with the C-axis parallel to the tensile-direction are called hard grains, while grains oriented with the C-axis perpendicular to the tensile axis are called soft grains after the number of active slip systems for such orientation of the grains [6]. If a soft and hard grain are located in proximity to each other, a deformation mismatch may occur. Others have called such grain combinations for a «rogue grain combination» F.P.E. Dunne et. al. [27]. Some have concluded that this is the main cause for fracture in titanium alloys [28].

2.8.2 HCP-Slip Systems

At room temperature the lowest CRSS-value is reported for the prismatic slip system. See last column in Figure 15 below for comparison with basal plane and pyramidal plane. Note that the CRSS-values are relative to pure α -titanium. The $\langle c+a \rangle$ slip type have a very large CRSS-value. This mean that very large forces are needed to deform along the c-axis [6].





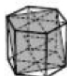

Slip plane No. of variants		Slip direction No. of variants	Total no of slip systems Designation	Approximat e relative CRSS
{0001} 1		$\langle \bar{2}110 \rangle$ 3	3 'Basal'	1
{01 $\bar{1}$ 0} 3		$\langle \bar{2}110 \rangle$ 1	3 'Prismatic'	0,7
{01 $\bar{1}$ 1} 6		$\langle \bar{2}110 \rangle$ 1	6 'First-order pyramidal'	3
{11 $\bar{2}$ 2} 6		$\langle 1\bar{1}00 \rangle$ 1	6 'Second-order pyramidal'	-
{11 $\bar{2}$ 2} 6		$\langle \bar{2}113 \rangle$ 2	12 ' $\langle c+a \rangle$ pyramidal'	-

Figure 15: HCP slips systems, and CRSS-value of the HCP-phase in Ti6Al4V relative to pure α -titanium. Figure reference: [29].

The HCP-unit cell has a lower c/a -ratio than the archetypal hexagonal cell i.e. 1.587 compared to 1.633. This compression along the c -axis gives a closer packing of atoms in the prismatic planes. SKRIVE OM The prismatic- along with the basal planes are the primary slip planes [6].

For single crystals, the difference in CRSS-values between prismatic and basal planes is assumed to decrease as the temperature increases. The difference can even disappear at higher temperatures [30]. Low oxygen content favors high fractions of $c+a$ gliding and twinning, and sometimes the activity of basal slip systems. In the same way an addition of Al increases the prismatic CRSS-value [30].

2.8.3 BCC-Slip Systems

The CRSS-value for BCC-slip systems are generally lower than for HCP in the Ti6Al4V-alloy. No CRSS-values are included in Figure 16 because a direct comparison between the crystal structures are not available [29]. The β -phase is only stable at high temperatures, or at room temperature for heavy alloying conditions. Measurements of the CRSS-value for β -phase single crystals with equilibrium alloying contents cannot be performed because the β -phase will always coexist with the α -phase at this condition. However, the BCC-crystal structure have more independent slip systems than the HCP-crystal structure, as indicated in the last column. This implies that this BCC will deform more isotropic than HCP. This also explains the more ductile and the easier workability properties of the BCC crystal structure.

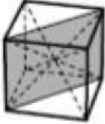
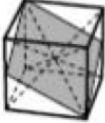
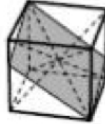
Slip plane No. of variants		Slip direction No. of variants	No. of slip systems
$\{110\}$ 6		$\langle \bar{1}11 \rangle$ 2	12
$\{112\}$ 12		$\langle 11\bar{1} \rangle$ 1	12
$\{123\}$ 24		$\langle 11\bar{1} \rangle$ 1	24

Figure 16: The BCC-unit cell have more isotropic mechanical properties compared to the HCP-unit cell because of more active slip systems.

Slip Bands

The crystal lattice is said to be perfectly restored after slip has taken place, ch. 4.4 [26]. The atoms moves a whole atomic distance along the slip plane and will produce a step in a polished metal surface. Slipbands can be seen as relatively straight parallel lines on a polished surface. Slip normally occurs most readily in the most densely packed atomic planes and directions in the crystal lattice. For HCP this corresponds to the basal plane, while BCC does not actually have a close packed plane. The BCC-unit cell have instead several planes with very similar densities. They are given in Figure 16. The limited number of slip systems in HCP is the reason for the extreme orientation dependence and low ductility in HCP-crystals.

Deformation Twinning

A twin is a region of the crystal where the lattice is mirrored across the twin plane. Twinning is also an important deformation mechanism in crystals having a limited number of slip systems, such as the HCP crystal. According to ch. 2.4.2 Lütjering [2], twinning plays a major role in deformation of pure titanium with low oxygen concentrations. Increased concentrations of Al and O suppress the occurrence of twinning. Twinning deformation modes are of most importance for plastic deformation and ductility at low temperatures if the stress axis is close to parallel with the c-axis. For this stress axis the dislocations in the basal plane cannot move. The most frequently observed twins are the $\{10\bar{1}2\}$. They have a very low twinning shear compared to $\{11\bar{2}1\}$. The $\{11\bar{2}1\}$ twinning mode is illustrated in Figure 17 below. Twinning like slip, must occur through the movement of dislocations. The Burgers vector of these dislocations must have the magnitude and direction of the shear between the successive planes [31].

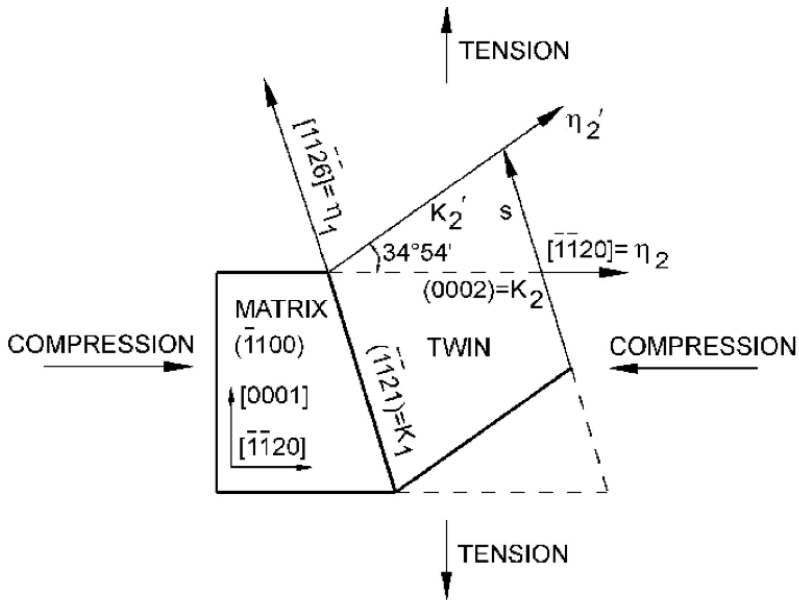


Figure 17: Shape change by $\{11\bar{2}1\}$ twinning. Lütjering ch. 2.4.2 [2].

Orientation Dependence of the Resolved Shear Stress for Slip and Twinning

In Figure 18 can a plot of the variation of Schmid factor with angle ϕ between the c-axis and the tensile stress axis for some slip and twinning modes in titanium be seen. Basal slip have no resolved shear stress at 0° and 90° orientations, but is a dominating deformation close to 45° . This is represented by the shaded area. For prismatic slip the resolved shear stress on the single slip system $(01\bar{1}0)[2\bar{1}\bar{1}0]$ varies from maximum when the stress axis is normal to the c-axis to zero when the stress axis is parallel. Further it can be seen from the figure that no twinning of $\{10\bar{1}2\}$ will occur for a tensile axis normal to the c-axis, while many twin systems may occur when the tensile axis is parallel to the c-axis [32].

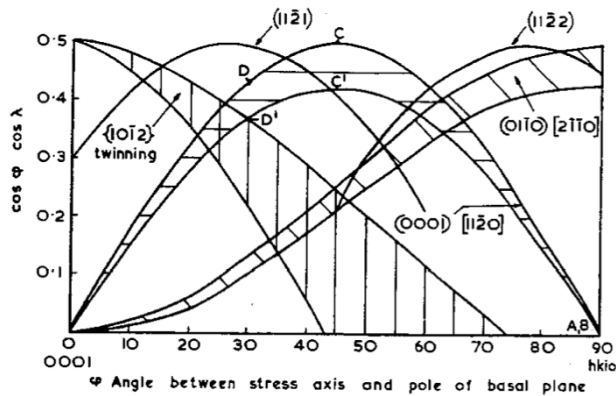


Figure 18: Variation of Schmid factor, $m = \cos\phi \cdot \cos\lambda$, for different orientations. Both slip systems and twin planes for different rotations of the HCP-unit cell are given. Shaded areas corresponds to orientation for dominating slip or twinning. Figure from [32].

2.9 Microstructural Effects

According to ch. 5.2.1 in Lütjering [2] the most important microstructural parameter determining the mechanical properties, for $\alpha+\beta$ lamellar microstructures is the α -colony size. The strength of the Ti6Al4V-material was further said to be dominated by microstructural effects compared to solid solution strengthening. The influence of the different microstructures present in the DMD-material on mechanical properties will be addressed in the following sections.

2.9.1 Dislocation Mobility

P. Castany et al.[33] performed in-situ TEM deformation experiments on a Ti6Al4V-alloy. They observed that dislocations can be emitted from α/β -interfaces and take a preferential orientation along their screw direction i.e. Burgers vector parallel to the dislocation line. All dislocations observed had an $\langle\bar{2}110\rangle$ -type Burgers vector and glide essentially in prismatic or basal planes. However, basal glide is slightly favoured in lamellar colonies because of the compatibility stress due to the α/β - interfaces. Calculation of the Schmid factor verified this, the prismatic glide system had a Schmid factor of 0.37 and the basal glide system 0.4. They also concluded that α/β -interfaces in lamellar colonies are not obstacles controlling the dislocation motion, but rather the lattice friction on screw dislocations. The high lattice friction is resulting from the three dimensional core structure of the screw dislocation. This is also responsible for the strengthening in lamellar colonies.

The α -colony size is said to influence the effective slip length in lamellar microstructures ch. 5.2.1 Lütjering [2]. The two phases have to deform independently inside colonies, but slip can easily be transferred across incoherent α/β -interfaces. The explanation for this is that the slip systems in each phase are parallel or close to parallel, as given by the BOR.

Effect of α -Colony Size on Fracture Mode and Ductility

Increased cooling rates across the β -transus temperature lead to decreased α -colony size. Figure 19 below illustrate its effect on YS and ductility. The sharp drop after the peak in the elongation curve is due to the change in microstructure from lamellar to martensitic microstructure. The martensitic microstructure is only expected in the top layer of a DMD-block because of the highest cooling rates are located there. However, this martensitic microstructure is not considered as a problem for the ductility in the DMD-material because the top layer is always machined away from the block. The change in ductility across the peak also lead to a change in fracture mode. At low cooling rates the fracture surface consist of dimples after transcrystalline fracture mode. At higher cooling rates a ductile intercrystalline dimple type of fracture occurs along the continuous α -phase at prior β -grain boundaries. The effect of primary α -phase on fracture mode and ductility is related to the preferential plastic deformation in these areas where premature crack nucleates [2]. Another explanation for why smaller α -colonies gives several improved mechanical properties has to do with the reduced accumulation of dislocations at each grain boundary during deformation. High densities of dislocations are sites where crack may initiate.

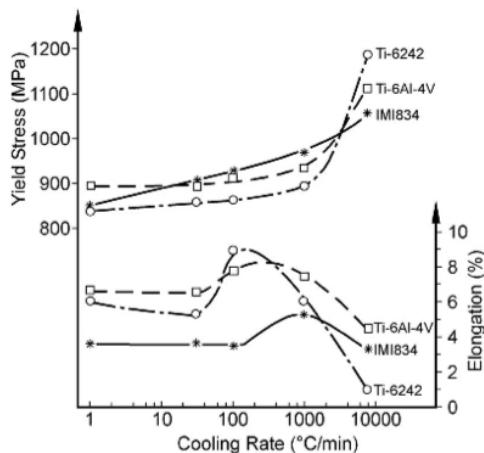


Figure 19: The figure illustrate that a decrease in α -colony size after faster cooling rates have significant influence on ductility and YS. Figure reference: ch. 5.2.1 Lütjering [2].

In contrast to the improved YS and ductility with decreased α -colony size as discussed above, the macrocrack propogation resistance and the fracture toughness are improved with larger α -colony size. This effect are probably due to increased crack roughness and crack-closure phenomenon for coarser lamellar microstructures ch. 5.2 Lütjering [2].

Elastic modulus

The elastic modulus is intermediate for Ti6Al4V among titanium alloys, but relatively low compared to other high-strength materials, ch. 5 [11]. Low carbon steel (ASTM-A36) have for instance twice as high elastic modulus, i.e. 200GPa. The elastic modulus is also very dependent on the texture of the material i.e. dominated by the average orientations of the α -grains. The literature reports values between 100-130GPa dependent of the orientation of the α -grains relative to the tensile direction. An elongation of up to 0.8% can also be accommodated elastically in the Ti6Al4V-alloy.

Strain Hardening Properties

Zn is a HCP-material which only can absorb deformation on the basal plane. This is in contrast to titanium which also can have duplex slip systems. This make Zn the ideal material for observing stress-strain curves without work hardening. HCP-materials do not work harden to the same extent as face cubic materials because dislocations in face cubic materials interacts much more frequently than in HCP. The ability to generate new dislocations and to increase the dislocation density is also lower in HCP. Both mechanisms are responsible for work hardening.

β -Grain Orientation and Anisotropy after DMD

Anisotropic mechanical properties are reported after tensile tests of the DMD-material. According to [14] can strain at failure be 2-3 times larger in the vertical direction compared to horizontal direction. The differences in UTS and strain at failure was said to be related to the coarseness of the α -lamellas and the orientation of the elongated prior β -grains. Another explanation for the smaller strain at failure for the horizontal tensile tests was also said to result from more β -grain boundaries for such orientations i.e. the β -grain boundaries are potential sources of failure.

Paul Colgrove et. al. [34] investigated the tensile properties of the DMD-material before and after rolling. They reported the improvements in Table 1 for the deposition direction after rolling. They claimed that even more improvements are likely for the vertical direction. The explanations for the improvements is that rolling of the microstructure in the β -region of the phase diagram will introduce nucleation sites. This will induce recrystallisation when layers are reheated during the subsequent deposition. This means that not only the average β -grain size is decreased but the α -lamella length and width will also be decreased. Other successful methods which can improve the mechanical properties of the DMD-material are presented in section 10.18 of the appendix .

Table 1: Improvements in mechanical properties after rolling. Analysis of the microstructures showed that the average β -grain size had decreased from several mm to $\sim 130\mu\text{m}$. Table from [34].

<i>Condition</i>	<i>YS (MPa)</i>	<i>UTS (MPa)</i>	<i>Elongation (%)</i>
Before Rolling	865	965	8
After Rolling	911	1006	11.5

Crack Propagation in Primary α -Phase

Impact tests of a butt welded Ti6Al4V-alloy have revealed that impact toughness can be 50% higher in the weld-zone compared to base material or the heat affected zone (HAZ). The weld-zone of Ti6Al4V is associated with large prior β -grains and the highest microhardness values which oppose the fact that this zone should have a large toughness value. The explanation for the improved toughness in this zone compared to the base material and the HAZ, is associated with the reduced amount of primary α -phase along prior β -grains. Microcracks can nucleate and grow relatively easy in the primary α -phase. Because of the homogeneous microstructure in such regions the crack also meet very few obstacles. The amount of primary α -phase is believed to be higher in the HAZ because of a prolonged exposure to temperatures in the two phase region $\alpha+\beta$ [35]. The more chaotic basketweave microstructure which is generally obtained in the fusion zone is also attributed to higher impact-values [36].

2.9.2 Effect of Globular α -Phase on Ductility

Globularization may be relevant for the DMD-material during subsequent heating by adding of new layers since the process spend relatively long time at elevated temperatures within the $\alpha+\beta$ -region of the phase diagram. Jin Young Kim et al. [37] concluded that the degree of globularization of α -phase is strongly dependent on the initial size of the lamellar structure. They observed that thick lamellar microstructures was more difficult to transform to homogeneous equiaxed structures than thin lamellar microstructures. They also observed that the fraction of globular α -phase was larger after thermomechanical treatment i.e. forging at subtransus-temperatures compared to only recrystallization heat treatments at the same temperatures. The explanation for this is the softer β -phase deform more readily than the α -lamellas in lamellar microstructures. This introduces dislocations to the interface between the phases where recrystallization may be initiated when heat treated. No external deformation is introduced to the lamellar DMD-material during processing but very fine lamellas in some parts of the microstructure may store enough residual stresses after transformation to favour globularization of α -phase. The $\alpha+\beta$ titanium alloys with lamellar structure have superior fatigue properties and creep resistance compared to equiaxed and bimodal structures. But a conversion from lamellar to the equiaxed or bimodal structures will increase the ductility significantly. For instance was the elongation improved from 13-18% by a gradually coarsening of the α -phase by different heat treatments in the $\alpha+\beta$ -region of the phase diagram [38]. See also Table 38 in the appendix for comparison of lamellar, bimodal and equiaxed microstructures with respect to ductility.

Effect of Oxygen Concentration Gradients on Formation of Ti_3Al -phase

Age hardening can occur for Ti6Al4V at temperatures between $500\text{-}550^\circ\text{C}$ by formation of intermetallic Ti_3Al -phase. The formation of this phase is promoted in O-rich regions of the microstructure such as the primary α -phase. The α -phase can solve more oxygen than the β -phase. When α -platelets are formed directly from O low β -phase upon cooling, this secondary lamellar α -phase will also be low on O. As a consequence of lower O-concentration this secondary α -phase will not respond as well to age hardening as the primary α -phase. This effect is called the partitioning effect where the primary α -phase generally have higher strength than the lamellar microstructures because of the age hardening effect of Ti_3Al -phase. However, this effect is of greater importance for higher concentrations of primary α -phase relative to α -lamellas. The effect is for instance more relevant for bimodal microstructures but this effect may also be present locally in lamellar microstructures[19].

Deformation Modes of HCP and Influence of Oxygen Concentrations

The lowest CRSS-values are generally obtained for the prismatic planes in interstitial free titanium. This value can be increased by large O-concentrations. The solubility of O in α -titanium is relatively large $\sim 30\%$. The activation of pyramidal slip systems may become comparable or even preferred to prismatic planes. O act as a lattice hardener in transition metals. Churchman presented a model which could help to predict where O and N atoms occupies octahedral interstices and interfere with the different slip systems [39].

Welsch found that during room temperature deformation of Ti6Al4V samples containing $0.22\text{wt}\%$ O, the samples produced predominantly planar pyramidal deformation only after aging at 350° [40]. The 350°C aging temperature is the lowest end of the oxygen relaxation peak in titanium measured by internal friction methods, and is believed to allow only very limited rearrangement of O in the titanium lattice. None of the metallic elements have any diffusional mobilities at this temperature [41], [42].

2.10 The EBSD-Technique

Set-up and Description of the Technique

EBSD-investigations are always conducted on a tilted specimen. This operation is performed to increase the fraction BSE from the atomic planes in the specimen surface. The EBSD-detector are placed in proximity to the sample surface to collect most of the BSEs. The BSEs are a result of Bragg-diffraction with the atomic planes in their uppermost 50nm of the sample surface. A regular SEM can be equipped with an EBSD-detector and corresponding software such as the NORDIF 1.4.0. This section will briefly introduce the main components and the set-up for the EBSD-technique.

The EBSD-detector also called the phosphor screen is a central component in the technique. This is where the EBSPs are generated and imaged. The EBSPs or Kikuchi-bands are a result of phosphorescence. What the EBSD-detector actually does is to convert an electronic signal to light which can be imaged with a high-speed camera. See Figure 20 for the EBSD-detectors location inside the SEM-vacuum chamber. The EBSD-detector used during this investigations was a NORDIF UF-300 coupled to NORDIF 1.4.0 software. The software take control of electron beam and store the EBSPs directly to hard disc. The storing of EBSPs on a hard disc enables repeated indexing. This was for instance utilized for indexing with and without the Ti_3Al -phase in this investigation.

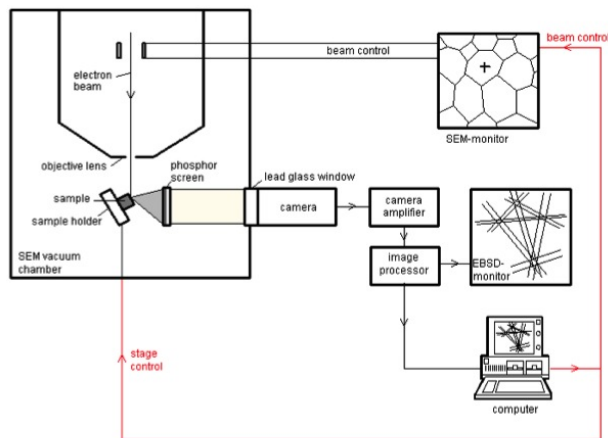


Figure 20: The different components and set-up of the EBSD-technique [43].

Advantages and Challenges

EBSD is a technique that can be used to examine many different characteristics with polycrystalline materials. It is also a flexible technique with respect to what information that can be obtained. This makes it a suitable technique to characterise the relatively new DMD-material. Phase distributions, grain boundary types, texture and morphology of grains are only some information that can be obtained. Since the technique rely upon imaging of EBSPs which are very sensitive to deformation, the technique is also suitable for qualitatively determining deformation and deformation mechanisms. This was utilized during the in-situ experiments performed in this work. However, the EBSD-technique is limited by the large pattern source volume of approximately 25-100nm. This is insufficient to analyse new nanostructured materials. But new transmission EBSD or SEM-transmission Kikuchi diffraction can have a spatial resolution better than 10nm [44].

NORDIF 1.4.0 Software

Before EBSD-investigation can start must the optics of the SEM be adjusted. The most important procedures regarding the SEM-optics are given in section 10.5 in the appendix. The right magnification of the SEM, tilt angle of the specimen and acceleration voltage must be given as an input values to the NORDIF 1.4.0 software. The acquisition- and calibration settings must be optimized for the given probe current condition. See section 10.6 in the appendix for the most frequently used acquisition and calibration settings in this investigation and the corresponding probe currents. Before starting an EBSD-scan, the region of interest (ROI) must be selected along with a suitable step size of the electron beam. The latter can be selected from the formula 2 below which present a relationship between the optimum magnification and the step size for the SEM. This was based on suggestions in paper [45]. For instance selecting a smaller step size than suggested by this equation may lead to less indexed points especially at grain boundaries. The explanation for this is that the data acquisition board generate electronic noise and vibration problems.

$$Step\ size(nm) = \frac{80246}{Magnification} \quad (2)$$

2.10.1 Effect of Probe Current

According to Y. Chen et. al. [45], to obtain a faster acquisition speed a higher probe current is needed to maintain the signal to noise ratio on the the phosphor screen. Higher intensity of electrons hitting the specimen surface at a given time increases the probability of having more Bragg-diffracted electrons from atomic planes in the sample surface. This is beneficial since the CCD-camera inside the EBSD-detector can be runned with "reduced" quality on the acquired images resulting in a shorter

acquisition time of EBSPs. Reduced quality means lower resolution and/or higher frame rate updates per second. However, the spatial resolution becomes worse by increasing the probe current because the beam size increases correspondingly. The relationship between the probe current and the spatial resolution is given in Figure 78 in the appendix. The formula 3 below can be used to determine the spatial resolution from the number of bad points in an IPF-map and to find a suitable spatial resolution for the respective material. The spatial resolution is relevant for the DMD-material consisting of very fine lamellas ($<10\mu\text{m}$) for them to be accurately resolved along grain boundaries.

$$R = \frac{N_{BP}D_s \sin\theta}{\frac{H}{D_s}} = \frac{N_{BP}D_s^2 \sin\theta}{H} \quad (3)$$

N_{BP} is the number of bad points e.g for a predefined Confidence Index (CI) <0.08 , H is the height of the scan area, D_s is the step size in nanometers, and θ is the angle between the grain boundaries and the horizon. This equation assumes that all non-indexed points are due to overlapping patterns at the grain boundary. Simple measurements of the probe current can be performed by either using a Faraday cup directly, or measuring the absorbed current from an absorbed current meter coupled to the stage inside the SEM.

Calculation of Probe Current for Horizontal Sample

For an horizontal sample equation 4 represents the relationship between the different fractions of the electronic signals that can be detected in a SEM. As seen from the equation is the probe current i_p split into three fractions: i_{se} =secondary electrons, i_{be} =backscatter electrons and i_{ab} =absorbed current or sample current.

$$i_p = i_{se} + i_{be} + i_{ab} \quad (4)$$

Equation 4 can further be decomposed into:

$$i_{se} = \delta \cdot i_p \quad (5)$$

$$i_{be} = \eta \cdot i_p \quad (6)$$

Where η and δ are the fraction BSEs and SEs, respectively. δ is independent on the atomic number of the specimen. A typical value of δ is 0.1 for 20kV acceleration voltage. In contrast to δ is η dependent on the atomic number. This can be seen from equation 7 below.

Z_i is the atomic number of the elements present in the sample and C_i is the weight percentages (wt%) of the elements in the alloy. Calculation of η for the Ti6Al4V-alloy will be presented below.

$$\eta = -0.0254 + 0.016 \cdot Z - 1.86 \cdot 10^{-4} \cdot Z^2 + 8.3 \cdot 10^{-7} \cdot Z^3 \quad (7)$$

$$Z = \sum C_i \cdot Z_i = 0.80 \cdot 22 + 0.06 \cdot 13 + 0.04 \cdot 23 = 19.3 \quad (8)$$

$$\eta = 0.22 \quad (9)$$

Insertion of η and δ into equation 4 will give the following relationship:

$$i_p = \frac{i_{ab}}{(1 - 0.1 - 0.22)} = \frac{i_{ab}}{0.68} \quad (10)$$

Equation 10 can be solved for i_p by measuring i_{ab} from an absorbed current monitor coupled to the stage inside the SEM. In Figure 27 can the NORDIF absorbed current meter used in this investigation be seen.

Calculation of Probe Current for Tilted Sample

When tilting the specimen prior to EBSD-investigation, the fraction of the different electronic signals in equation 4 will be altered while i_p remains constant after tilting. Tilting is always performed before EBSD to increase i_{be} , the only electronic signal used for EBSD. To simplify the calculation can i_p be calculated directly from a tilted sample by introducing the constant K below. For instance will a measured i_{ab} =38.5nA on a horizontal specimen correspond to approximately i_p =56nA from equation 10. After tilting the i_{ab} drops to 15nA. K can then be calculated:

$$K = \frac{i_{ab}(tilt)}{i_p} = \frac{15nA}{56nA} = 0.267 \quad (11)$$

K was used to calculate the i_p -values presented along with the EBSD-results later in this report.

Deposition of Hydrocarbons at the Specimen Surface

The origin of hydrocarbon contamination at the specimen surface is due to the electron beams affinity to the molecules in the residual gases in the specimen chamber, and other contaminants present in the specimen chamber of the SEM. The thickness of the hydrocarbon layer is dependent on exposure time and the probe current magnitude.

Y. Chen et. al. [45] concluded that contamination is only a problem when performing repeated scans of the same area at the specimen surface, due to built-up of hydrocarbon layer. They experienced that the percentage indexed points and IQ-value dropped quickly after four scans for a probe current of 33nA, vacuum degree of $6 \cdot 10^{-5}$ Pa and frame rate of 140 patterns per seconds. They also reported that the fraction indexed points stayed constant as the step size decreased from 50nm to 1nm. This was surprising findings because of the following arguments. The pattern quality was expected to be strongly influenced when the step size is significantly smaller than the diameter of the contaminated area. The idea was to select a larger step size to move away from the contaminated areas and thereby improving the pattern quality. But this was proven to not be right. Repeated EBSD-scans are especially relevant for in-situ investigations to observe the deformation mechanisms at different strains. For such investigations may also hydrocarbons contribute to lower the overall quality parameters of the EBSD-map in addition to the deformation introduced to the material.

The reason for why this is contamination layer is unwanted is because the BSE must pass through a foreign layer of hydrocarbons. This can lead to a lower fraction indexed points at a later stage. To reduce this problem it is always desired to have as low vacuum as possible. For instance did the SEM pump vacuum during the night for alle in-situ experiments performed in this investigations.

2.11 TSL OIM Data Collection 5.32 Indexing Software

The EBSPs stored on hard disc must be indexed by the TSL OIM Data Collection 5.32 indexing software before the microstructure can be analysed in the OIM Analysis 6.0 software. In short does this software convert a large pattern.dat-file to smaller osc-file i.e. from gigabytes to megabytes. The following sections will present the most important information regarding these softwares.

Pattern Center

After the ROI is selected in the NORDIF 1.4.0 software a set of calibration points must also be selected before an EBSD-scan can be runned. A minimum of four calibration points are selected, one in each corner of the ROI. Generally are more calibration points selected because it is very likely that a calibration points contains either zone axis or overlapping patterns at grain boundaries. Such badly selected calibration impair the overall quality of the IPF-map drastically. The DMD-material contains a large fraction grain boundaries which make this selection of calibration points challenging. The calibration points only function is their reference for the later interpolation and indexing sequence. When loading the pattern.dat file in this software, the first thing the software ask for is the X-, Y-, Z-coordinates of the calibration points. The coordinates are referred to as the pattern center, which is given in percentage of a distance. The area of the CCD-chip of the EBSD-detector restricts the X- and Y-distance, while the Z-distance is the length from the tilted specimen surface to the phosphor screen. It can be observed that the Z-distance slightly varies $\sim 1-2\%$ between the different calibration points i.e. the lower calibration points have a smaller Z-coordinate than the ones on the top of the ROI. The explanation is the shorter distance from the phosphor screen to the lower part of the specimen contra the upper part. However, it is important to note that the camera length Z, is relatively constant for a given SEM installed with an EBSD-detector. The camera lengths of the Hitachi microscope and the Zeiss microscope used are given in Table 25 in the appendix.

Hough Transformation

The theory about the Hough-transform has been described in detail elsewhere and the reader is referred to [46] for more information. The Hough transformation settings used during this investigations are presented in the Table 24 in the appendix. In addition to Hough transformation settings must the expected phases in the material be selected before indexing. If the database does not contain information about the phase, the software enables "building" of new phases. This was performed in this investigation, see section 4.5 in the experimental part of the report for required input parameters to the software.

2.12 TSL OIM Analysis 6.1 Software

It is important to note that OIM Analysis 6.1 software is a very large program with functions beyond the scope of this work. Therefore, only the most fundamental parameters will be presented here. The software enables researchers to analyze polycrystalline materials in details. This software uses the indexed EBSPs from TSL OIM Data Collection 5.32 Indexing software to create different types of maps to visualize the grains and phases present in the material. The mapping functions will not be introduced here but a short description can be found in previous work, section 6.9.5 [47]. In this section will the fundamental quality parameters of the EBSD-map be presented. Somehow they are the fundamentals to understand the mapping functions in the same software.

2.12.1 Quality Parameters of EBSD-map

The confidence index (CI), image quality (IQ), and Fit parameters can somehow be called quality marks on the EBSPs and of the final EBSD-map after indexing. Highly deformed materials generally score lower on these values than recrystallized materials because of the more twisted and diffuse EBSPs generated. It is important to note that also grain boundary area, sample preparation procedure, skills of the SEM/EBSD-operator and internal stresses after solidification of the material plays a role on these parameters. Therefore, they can be considered as some of the most important results obtained from this software. In addition are they used as a basis to create different maps in the software. The parameters will hereafter be referred to as the quality parameters of the EBSD-map. This includes all three parameters. The three parameters will be described below.

CI

This parameter is calculated during automated indexing. For a given EBSP several possible orientation of the grain is possible orientations. The software give scores to the different orientations by counting correctly indexed triangles in the EBSPs. The triangles are formed by intersection of three zone axes in the EBSP. The orientation with highest score is ranked first and will be the indexed orientation. The CI ranges from 0 to 1. The formula for calculating CI is given in the appendix section 10.9.

IQ

The IQ-parameter is a scalar value measured for each diffraction pattern collected regardless of index results. Essentially is IQ related to the brightness level of a diffraction bands above a normalized background. The parameter is affected by the diffraction intensity for a phase, dislocation/crystallographic defects, density, and orientation of crystals. IQ-maps are generally greyscale maps that appear similar to SE-images in the SEM, but are generally coarser and more contrastful.

Stripes after grinding and grain boundaries are examples of areas which normally appears dark in such maps [48].

Fit

The Fit parameter defines the average angular deviation between the recalculated bands and the detected EBSPs. The closer to zero the Fit-value is the better result. However, like the other parameters above this value is also very dependent on the deformation of the lattice e.g. after sample preparation.

3 Materials

The fully lamellar DMD Ti6Al4V-alloy used for this investigation was provided by NTiC. Two blocks with two different ITs parameters were delivered. They are referred to as T200 and T600. Their chemical composition can be found in the Tables 2 and 3. The dimensions of the blocks were $30 \cdot 15 \cdot 3 \text{ cm}^3$, approximately. The geometry of block T200 right after production at NTiC can be seen in Figure 21. The blocks consists of forty layers in total in the building direction Z, and three parallel strings in the Y-direction i.e the width of the blocks. In the lower part of the image the rolled bimodal substrate plate of same Ti6Al4V-alloy grade can be seen. The blocks were produced without alternating deposition direction i.e. deposition occurred only along the positive X-direction in the image. The built-height of one layer measures 4-6mm.

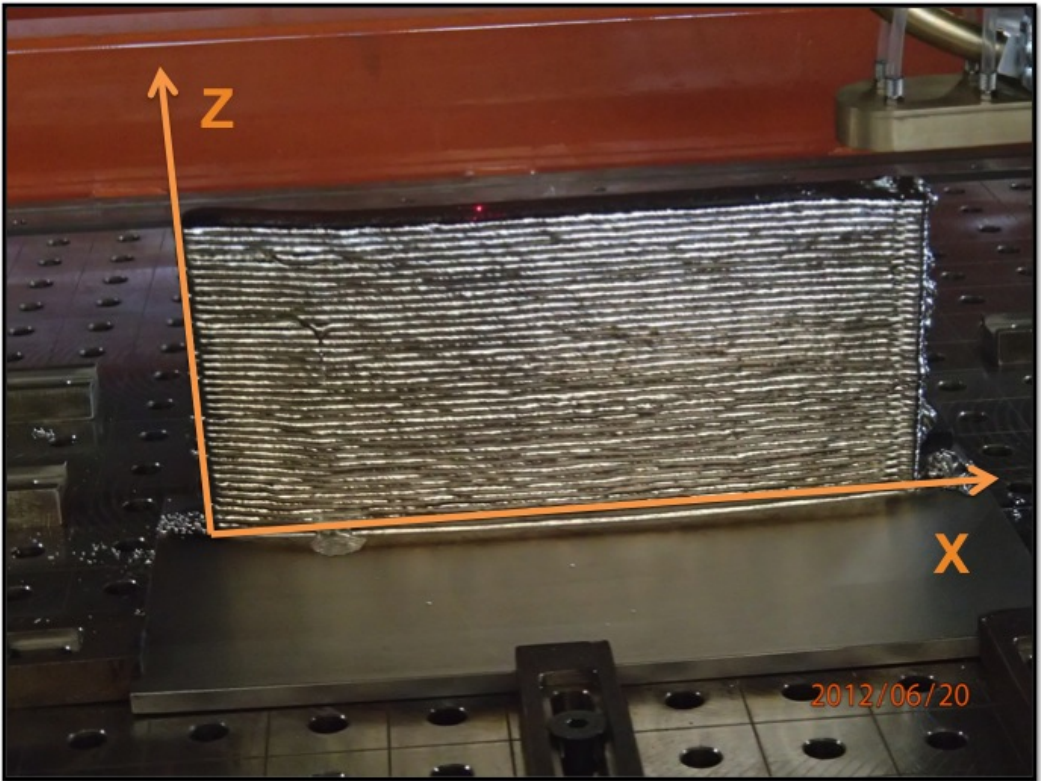


Figure 21: Block T200 with corresponding coordinate axis attached.

3.0.2 Interpass Temperature

The IT is defined as the temperature of the material just prior to the depositing of an additional pass. To achieve the desired IT, a waiting-time must be applied between each pass. For the case of block T600 to achieve a temperature in the range 500-700°C, a waiting time of 8-30s was applied. And for the case of block T200 to achieve a temperature <200°C, a waiting time of 190-270s was applied. If no additional cooling supplies are added in the production of the blocks and they have the same geometry, this corresponds to a 24X faster production time of block T600 compared to T200. This information is based on formula 1 presented in section 2.4.1.

3.0.3 Chemical Compositions

The chemical compositions of block T200 and T600 are given in Table 2 and 3, as measured by SINTEF Raufoss Manufacturing. The chemical compositions were according to the specification SAE AMS 4911L for titanium plates. The compositions were reported to be fairly uniform within the blocks.

Table 2: Mean chemical composition in block T200.

<i>Element</i>	<i>Mean composition</i>	<i>Reference: SAE AMS 4911L</i>
Al	5,7%	5,50-6,75%
V	3,93%	3,5-4,5%
H	38ppm	150ppm
O	0,177%	0,20%
Fe	0,18%	0,30%
C	0,022%	0,08%
N	0,112%	0,05%

Table 3: Mean chemical composition in block T600.

<i>Element</i>	<i>Mean composition</i>	<i>Reference: SAE AMS 4911L</i>
Al	5,72%	5,50-6,75%
V	3,94%	3,5-4,5%
H	39 ppm	150 ppm
O	0,18%	0,20%
Fe	0,18%	0,30%
C	0,020%	0,08%
N	0,12%	0,05%

3.0.4 Reported Differences in Microstructure

SINTEF reported that block T600 may contain more of the primary α -phase compared to T200. This phase is indicated by the arrow in Figure 22. Both images are taken from a prior β -grain boundary for comparison. Hopefully can this work help to answer if this phase is the only difference between the block leading to the different ductility. The prior β -grain boundary is located slightly more to the right in the right image.

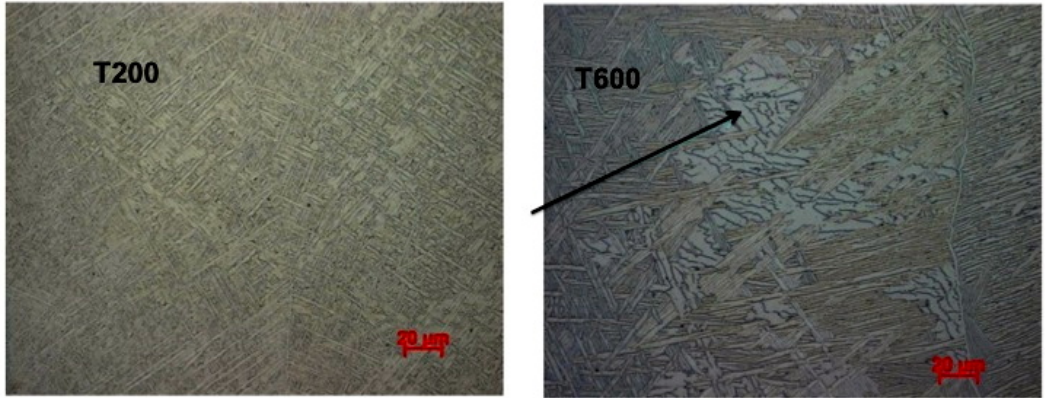


Figure 22: There are some evidence for more primary α -phase in block T600 indicated by arrow. This phase may have an influence on ductility.

3.0.5 Mechanical Properties

SiINTEF reported the mechanical properties in Table 4 and Table 5 for the two respective blocks. It can be seen from tables that the elongation was increased with higher IT for the deposition direction, while the blocks had relatively similar strengths. When comparing the tables, the strength values are generally higher parallel to the deposition direction compared to building direction, while the elongation is higher in the building direction. The deformation mechanisms behind the impaired ductility observed in the deposition direction is the motivation for the in-situ experiments performed in this work. In addition were all strength-values for the DMD-material above the limits in the B381 standard for Ti6Al4V forgings, while the ductility was reported to be below the limit of 10%.

Table 4: Mechanical properties after tensile tests in the deposition direction of T200 and T600. Compared to mechanical datas in standard specification B381 (standard for forged titanium products used by airplane manufacturers), the blocks perform well with respect to strength but the ductility is a few percentage behind. The numbers are rounded to nearest ten.

<i>Mechanical Properties (Deposition direction)</i>	<i>T200</i>	<i>T600</i>	<i>B381</i>
Ultimate Tensile Strength, UTS (MPa)	985	978	895
Yield Strength, YS (MPa)	919	918	828
Elongation to breaking point (%)	5	8	10

Table 5: Mechanical properties after tensile tests in the building direction of T200 and T600. Compared to mechanical datas in standard specification B381 (standard for forged titanium products used by airplane manufacturers), the blocks perform well with respect to strength and ductility. The numbers are rounded to nearest ten.

<i>Mechanical Properties (Building direction)</i>	<i>T200</i>	<i>T600</i>	<i>B381</i>
Ultimate Tensile Strength, UTS (MPa)	949	930	895
Yield Strength, YS (MPa)	888	874	978
Elongation to breaking point (%)	10	9	10

3.0.6 Stress Relief

After deposition the blocks were stress relieved in a vacuum furnace at 700°C for two hours before they were furnace cooled to 500°C. At the end of the stress relief heat treatment the components were cooled by convective nitrogen gas to room temperature. See Figure 79 in appendix for temperature-time curve.

3.0.7 Disposition of the Material

After previous work [47] the remaining material had to be disposed to the different experiments. Figure 23 illustrate the different locations of the material used during the experimental part of the work. The orange marked parts was used to extract in-situ tensile specimens, the blue part were used for the macroetching experiments to reveal the solidification structure, and the green parts was further sectioned to smaller EBSD-samples. The following sections will explain the different experiments performed in this work.

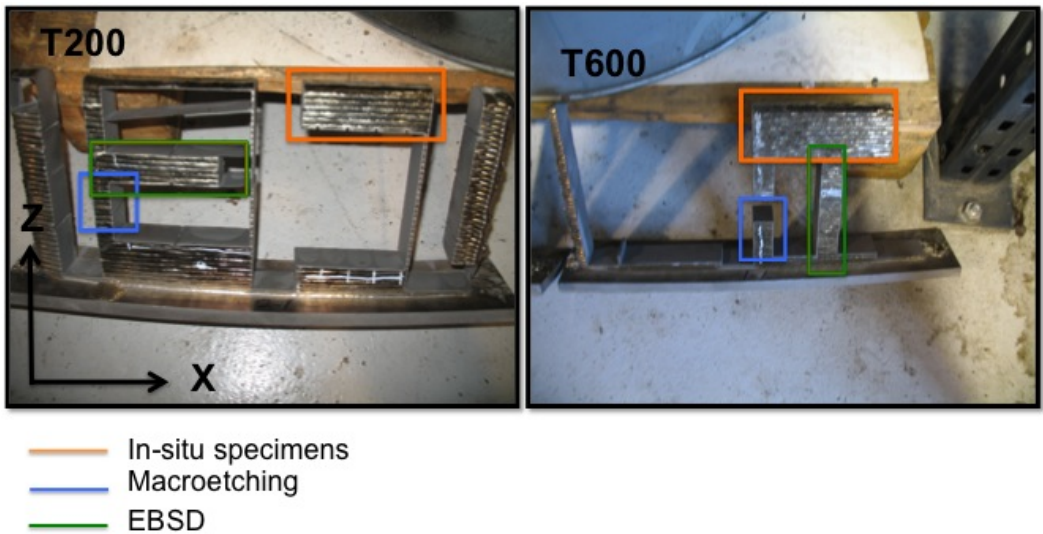


Figure 23: Material-disposition

4 Experimental

A good and comprehensive description of the applied experimental techniques is essential for understanding the results obtained in this work. Therefore, the following sections will describe the sample preparation and the operation parameters for the equipment used in details.

4.1 Sample Preparation for General Metallographic and EBSD-Analysis

This section covers the preparation sequences for the non-tensile specimens. These were analysed to become familiar with the microstructure, and to determine representative areas of the microstructure for scans during the later in-situ tests. The following procedure was proved successful in previous work. This sample preparation is mainly based on this previous work [6]. But some improvements has been made. The color-etching with Wecks reagent is new, and the ion milling parameters has been improved.

4.1.1 Cutting

For initial characterisation of the material, small samples measuring approximately 10mm·20mm·4mm were extracted from the received blocks. The roughest cutting was performed by water-jetting and bandsaw at Finmekanisk Verksted, NTNU. Further cutting into smaller specimens were performed by using a Struers Discotom 5 cutting machine with Struers abrasive disc type 20S25 for ductile materials. The rotation of the cutting wheel was kept just above 1000rpm, while feed rate was kept constant and quite high, estimation: 1mm/s. The Struers Discotom 5 has water cooling, which is necessary to avoid alteration of the microstructure by extensive heating in the cutting-region.

4.1.2 Grinding

The roughest grinding sequence with SiC-paper was performed on a Struers Rotoforce-4 apparatus. The finer grinding was performed on a Struers Tegra combined grinding and polishing apparatus. The chosen procedure for sample preparation was based on suggestions in [49].

Table 6: Parameters used for grinding. The forces are selected in the display of the apparatus and are given as per sample. RPM=rotation per minute.

<i>Step</i>	<i>Grinding Surface</i>	<i>Time</i>	<i>Force</i>	<i>RPM</i>	<i>Lubricant/Suspension</i>
1. Rough	320 μ m SiC paper	5min	25N	300rpm	Water
2. Fine	MD Largo (Struers)	10min	25N	150rpm	9 μ m grit Diapros

4.1.3 Polishing

To achieve a mirror-like surface, chemical-mechanical polishing was performed on the Struers Tegra apparatus, with the parameters given in Table 7. OPS is an alcohol-silica suspension of grit $0.4\mu\text{m}$. H_2O_2 (Hydrogen Peroxide) was added as an oxidising agent. This is known to contribute to removal of deformed layers during polishing of Ti.

A rinsing step with water was added to remove traces of the OPS-solution from the polished surface. See Table 8 for concentration and volume of the suspension/chemical.

Table 7: Parameters used for polishing. The forces are selected in the display of the apparatus and are given as per sample. RPM=rotation per minute.

<i>Step</i>	<i>PolishingSurface</i>	<i>Time</i>	<i>Force</i>	<i>RPM</i>	<i>Lubricant/Suspension</i>
1	MD Chem cloth (Struers)	10min	15N	150rpm	OPS + H_2O_2
2	MD Chem cloth (Struers)	1min	10N	150rpm	Water

Table 8: The mixing ratios between the chemicals used in step 1 Table 7.

<i>Suspension/Chemical</i>	<i>Concentration</i>	<i>Volume (%)</i>
OPS	10%	90%
H_2O_2	35%	10%

4.1.4 Etching and Macroetching

The Kroll-etch given in Table 9 was mainly used for the macroetching experiments of the different planes of the DMD-blocks. The same grinding and polishing sequence as presented in section 4.1.2 - 4.1.3 was used for these specimens. A regular digital camera with zoom objective lens was used for the macroetching photos presented in appendix section 10.4. The same Kroll-etch was used to reveal deformation on the in-situ specimens by lightmicroscope (sometimes Weck's reagent for color etching were used). See Table 9 and 10 for chemicals and etching time. Since etching destroys the surface for later EBSD-investigation, the etched samples were dedicated for light microscopy and SEM-purposes only. After etching the samples were immediately rinsed in ethanol and then water.

Table 9: Chemicals in Kroll-etch. Samples were submerged for 8 seconds

<i>Kroll's etch</i>
2ml HF
10ml Nitric Acid
88ml Water

An additional etch was sometimes used to reveal the optical anisotropy of the HCP-phase platelets, and to get a color effect by polarized light.

Table 10: For a stronger etchant effect, Weck's reagent was used subsequently to Kroll. Samples were submerged for 25s.

<i>Modified Weck's reagent (color etch)</i>
100ml Water
25ml ethanol
2g ammonium bifluoride NH_4FHF

4.1.5 Cleaning

After finishing the grinding and polishing steps, a thorough rinsing in a ultrasonic bath of acetone was performed for 10min. Samples were then flushed with ethanol. As a final cleaning before insertion into SEM the specimens were plasma-cleaned in a Fischione Model 1020 plasma cleaner for 10min. To avoid stains from fingertips the samples were handled with rubber gloves after this step.

4.1.6 Ion Sputtering

Ion sputtering can be used as a stand-alone final surface preparation after mechanical polishing. In previous work [6] it was used more as a rinsing than an eroding process. In this work the ion milling sequence was added to the chemical-mechanical polishing to improve the average quality parameters of the EBSD-map for the DMD-material. From previous work the quality of the EBSD-maps was regarded as relatively low. See project work [47]. The parameters used in the Hitachi M-3000 ion mill are presented in Table 11 below.

Table 11: Parameters used for the Hitachi M-3000 ion mill.

Accelerating voltage	4
Tilt angle	80
Eccentricity	3mm
Time	30min
Mode	2 (10 rpm and 360° rotation)
Gas flow	$0.09\text{cm}^3/\text{min}$

4.2 Specimen Sampling of In-situ Tensile Specimens

In previous work [47], the main idea was to investigate the DMD-material in all crystallographic planes relative to the deposition direction X with the EBSD-technique. In this work, this was not considered as the main focus. In this investigation the idea was to reveal differences between the blocks by investigating regions surrounding the β -grain boundaries. The explanation for this is that the prior β -grains were according to theory the location where, differences are likely to be detected. Primary α -phase and α -colony size are both microstructures that forms at β -grain boundaries which can be compared when selecting β -grain boundaries as a ROI.

Nine in-situ. tensile specimens from each block were extracted by spark cutting at Nomek Ranheim. Figure 24 illustrates the location of the in-situ tensile specimens in each block. The T200 tensile specimens were located higher up in the block. Note that the size of the β -grains are several millimeters long in deposited materials, and may therefore be present in adjacent in-situ tensile specimens. The tensile specimens were extracted from the blocks such that they could be tensiled along the deposition direction X, and investigated by their XZ-planes. See attached coordinate axis in the image. The geometry of the in-situ. tensile specimens can be seen in Figure 25.

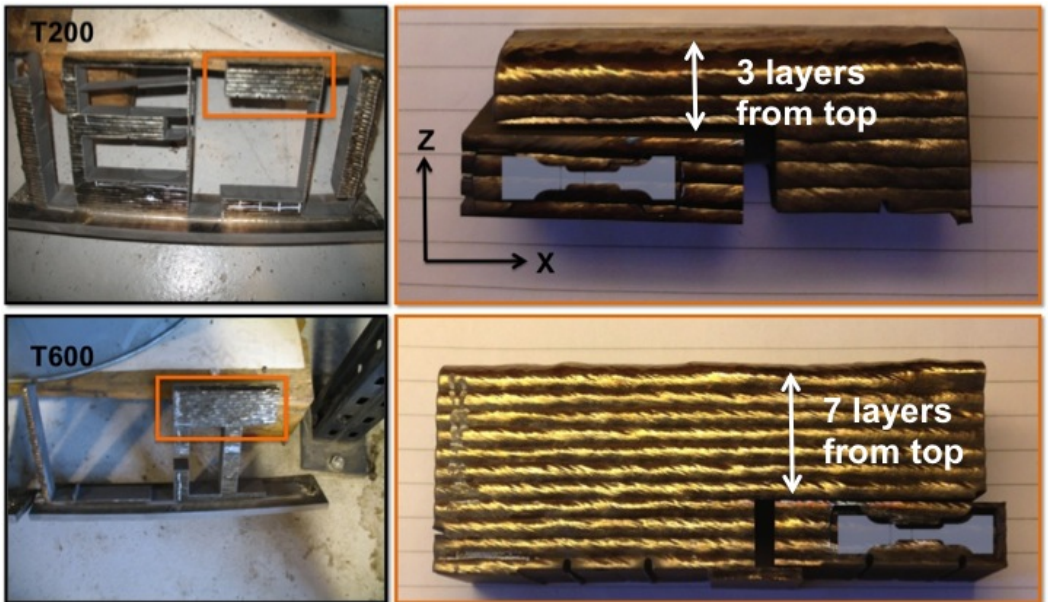


Figure 24: The In-situ specimen test locations in block T200 and T600. The nine in-situ specimens are located parallel to each other into the plane of the image.

4.2.1 Preparation of In-situ Tensile Specimens

The in-situ. specimens were attached to a plexi glass plate with double-sided tape before sample preparation to enable grinding and polishing by hand. See Figure 26 below for in-situ specimens glued to the plexi glass plate. The specimens were located at each end of the plexi glass plate to create a stable fundament during grinding. The same sample preparation procedure as presented in section 4.1 were followed for the in-situ- tensile specimens. Before ultrasonic bath and plasma cleaning, the specimens had to be detached from the plexi glass plate.

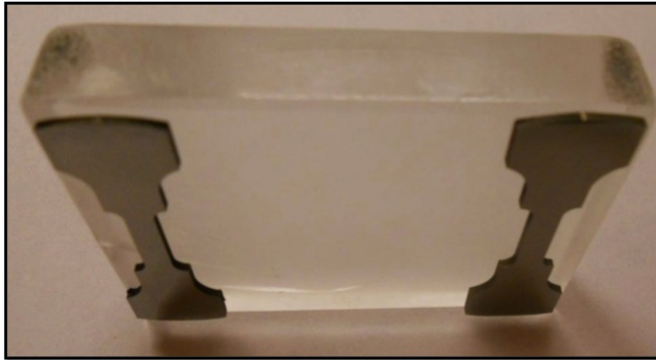


Figure 26: In-Situ specimens glued to a plexi glass plate by double sided tape. Image Ref.: [6]

4.3 SEMs

Two different SEMs were used, Hitachi SU6600 Variable Pressure Schottky FE-SEM and the Zeiss Gemini Ultra 55 Limited Edition. For the initial EBSD-investigations, to get familiar with the different microstructures present in the material and to find good SEM-settings for the respective material, the Hitachi microscope was the selected instrument. The reason for this selection is that this microscope is easier to switch between different condensor-lens conditions which also gives different probe currents. The Zeiss microscope was the selected microscope for in-situ. tensile experiments because of the large specimen-chamber which allows insertion of in-situ tensile stage. See section 4.4 for in-situ tensile equipment used.

Operation Parameters for the Hitachi Microscope

The NORDIF Absorbed Current Meter in Figure 27 was frequently used in this investigation. It is mounted to the stage of the Hitachi microscope and make calculations of the probe current magnitude possible. The equation used for the probe current calculations was presented in section 2.10.



Figure 27: The NORDIF Absorbed Current Meter used to calculate the probe current in the Hitachi Microscope.

Table 12: Operation parameter of the Hitachi microscope. This SEM is built for probe currents as high as $>200\text{nA}$.

Accleration voltage	20kV
Probe current	-43 to -85nA
Working Distance	26mm
Tilt angle	70°
Aperture	Large analy
Magnifiaction	150-2000X

Operation Parameters for the Zeiss Microscope

To deal with the lower emission current from the filament in the Zeiss microscope compared to the Hitachi SU6600, this microscope was always operated at maximum probe current conditions during the in-situ experiments. Highest possible probe current was ensured by the largest aperture size of $300\mu\text{m}$ and the high current mode-function in the software. This conditions gave the probe current-values given in Table 13. To ensure highest possible system vacuum to reduce problems with hydrocarbon-deposition on the sample surface during the experiments, the tensile stage was mounted a day before the experiments were performed to pump vacuum. The vacuum achieved after pumping during the night is also given in Table 13. However, even its not recommended can in-situ experiments be performed after only 10-15min vacuum pumping if its desired to perform experiments within the same day. The filament can be turned on for a vacuum as high as $7.6\cdot 10^{-5}\text{Torr}$. This will increase the hydrocarbon-deposition drastically.

Table 13: Operation parameter of the Zeiss microscope

Accleration voltage	20kV
Probe Current	-37nA (maximum)
Working Distance	23-24mm
Tilt angle	70°
Aperture	$300\mu\text{m}$
Magnifiaction	150-1000X
Vaccum	approx. $2\cdot 10^{-6}\text{Torr}$

4.4 In-situ Tensile Equipment set-up

In the upper image to the right can the Zeiss Gemini Ultra 55 Limited Edition microscope used for the in-situ experiments be seen. Inside the specimen chamber of the SEM at position 1, was the in-situ tensile stage in image 2 mounted. See larger image of the stage in section 4.4.1. The different parts of the tensile stage is also described in section 4.4.1. To the left in the upper image can the control unit box and PC used to operate the tensile stage be seen. This PC was installed with a traction software which logged the stress and strain during tensile-tests. The stress-strain curves from this software will be presented along with the results later in this report.

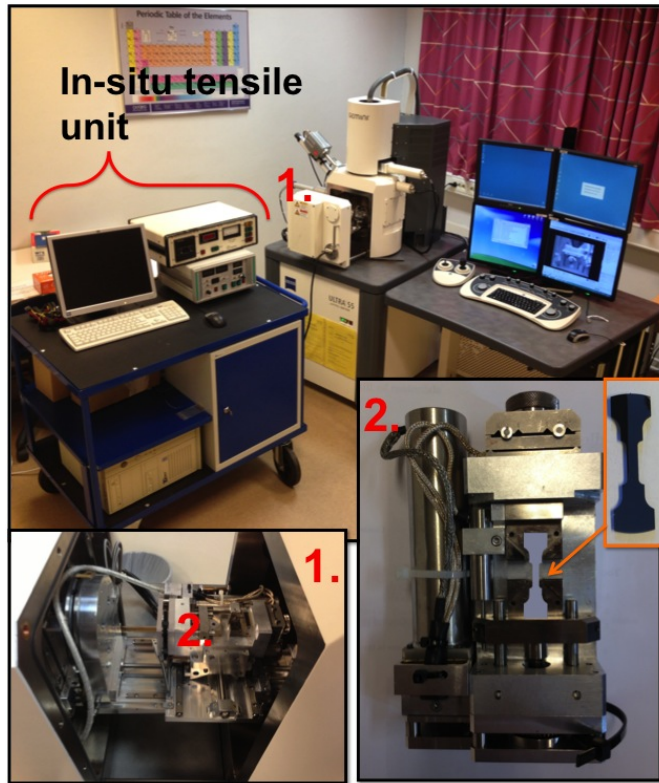


Figure 28: The equipment used for the combined EBSD+ in-situ tensile test performed.

The tensile test can be stopped at any desired elongation to capture EBSD-images of the microstructure. In reality this is a semi-in-situ experiment, because EBSD-images are acquired after tensile and not during tensile-tests. Interruptions were conducted by stopping the motor after the input-values for elongation given to the traction-software.

4.4.1 In-situ Tensile Stage

The in-situ tensile stage is run by a low-g geared electrical motor which allows monotonic tensile tests. The displacement speed of the movable ramp in Figure 29 was selected to be $10\mu\text{m/s}$. The dimension of the stage measures approximately $17\text{cm}\cdot 10\text{cm}\cdot 4.5\text{cm}$.

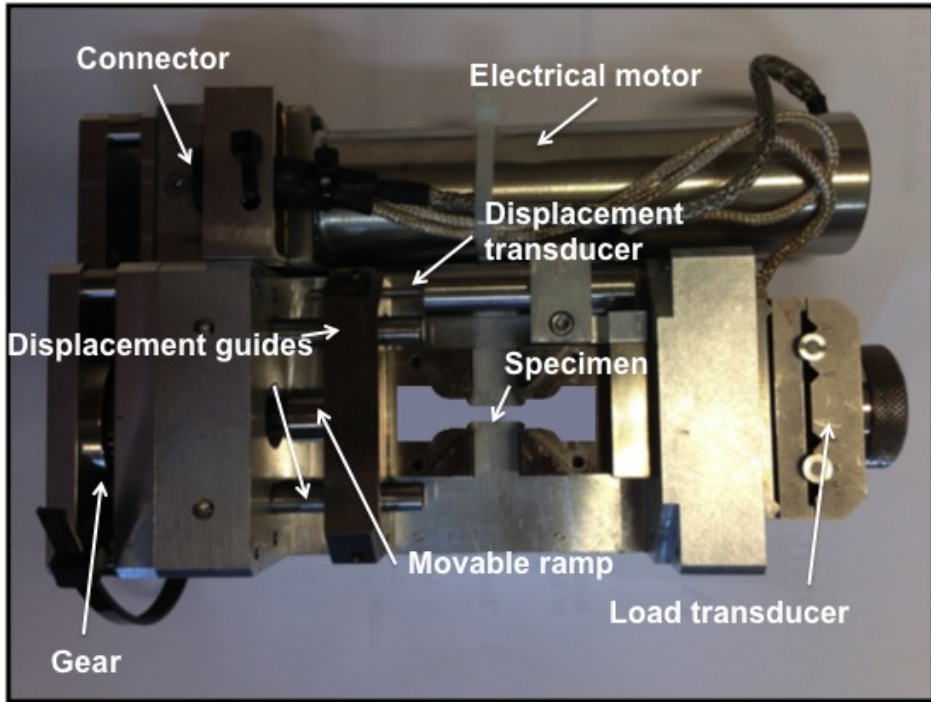


Figure 29: Desired elongation was instructed to the in-situ tensile unit See Figure 28 to run the motor of the tensile stage.

4.5 Indication of Phases by XrD-Analysis

According to phase diagrams in section 2.3.1 and 2.3.2, three phases can be expected in the Ti6Al4V-alloy. α , β and the intermetallic phase Ti_3Al . Since EBSD only can distinguish between phases in the uppermost 50nm of the surface of the material this method is not very suitable for finding minority phases. X-ray diffraction have a much larger interaction volume, approximately $8\mu\text{m}$ for Ti6Al4V (at 40kV acceleration voltage). This increases the probability of finding minority phases. Since only small amounts of Ti_3Al phase can be detrimental for mechanical properties it is important to detect this phase.

Remaining phases at the surfaces of the samples after the sample preparation can also be detected by XrD, and tell us how successful the cleaning of samples was before EBSD-investigations. Since remainings of lubrications and suspensions may impair BSE-signals this is also important information which can be detected by XrD. Samples was prepared for XrD by the same sample-preparation procedure as for EBSD, see section 4.1. The XrD was performed on solid samples (XrD are generally performed on powder samples).

Updating TSL OIM Data Collection 5.32 Database for new Ti_3Al -Phase

Indexing of EBSD-scans with and without Ti_3Al -phase were also performed to reveal the phase. The indexing database did not contain information about the phase and had to be updated for the lattice parameters given in Table 14 in the below. Lattice parameters from [50].

Table 14: Lattice parameters and angles of the Ti_3Al unit cell. The hexagonal unit cell can be seen in Figure 4 in the theory Section 2.3.1.

<i>Lattice Parameter</i>	<i>Unit cell angles</i>	<i>Atomic Coordinates</i>
a: 5.614Å	α : 120°	X: Ti: 0.16667, Al: 0.33333
b: 5.614Å	β : 90°	Y: Ti: 0.33333, Al: 0.66666
c: 4.665Å	γ : 90°	Z: Ti: 0.25, Al: 0.75

5 Results

5.1 Macroetched Samples

Macroetching at different planes were performed to get a 3D overview over the solidification structure before investigations at higher magnification by EBSD. The observations from the etching-experiments are summarized in Figure 30 below. This sketch is based upon the macroetched samples in Figure 80 of the appendix.

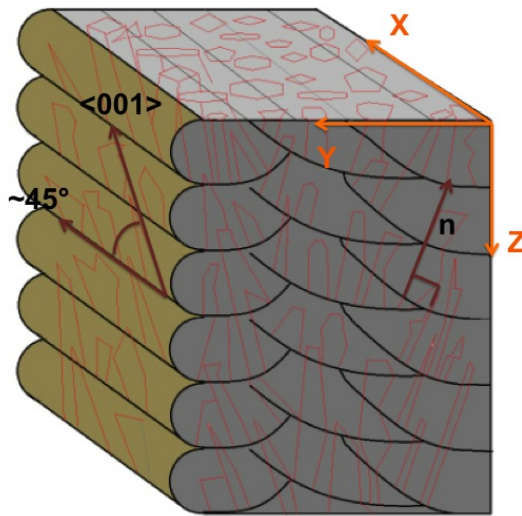


Figure 30: Illustration of the solidification structure observed in the DMD-material.

It could be observed that the XY-plane contained an almost equiaxed grain morphology, indicating that the β -grains were imaged close to parallel with their growth direction $\langle 001 \rangle$. Further, it could be observed in the XZ-plane that the grains had a weak tilting towards the deposition direction X (approximately 45°). The blocks investigated were made by deposition of material only along the positive X-direction. However, alternating deposition directions can be implemented in the DMD-process. In either case will the grains tend to inherit the orientation from β -grains in previous deposited layers and grows directly through the fusion line. The fusion line are indicated with black bulging lines in the YZ-plane of the figure. The macroetched YZ-plane also revealed that the β -grains tend to grow normal (n) to the fusion lines.

The measurements of grain sizes of the two blocks were performed in the XZ-planes where the grains have the most uniform distribution. The measurements are highly uncertain and was calculated by counting the total numbers of grains divided on

the area of the XZ-plane i.e. $2.5\text{cm}\cdot 2\text{cm}$. T200: 106 grains corresponds to an average grain area of 0.047cm^2 . T600: 87 grains corresponds to an average grain area of 0.0575cm^2 . Even in light microscope are the different grains hard distinguish and makes measurements uncertain.

5.2 EBSD+In-situ Tensile Results

The positions of the EBSD-scans are indicated with arrows on the different in-situ specimens in Figure 31 below. In total were four specimens tensiled, two specimens from each block. The darker regions origins from hydrocarbon deposition after the EBSD-scans. When comparing the different specimens at low magnifications, the T600 specimens are more locally deformed compared to the T200 specimens. It was not desired to tensile the specimens to the breaking-point during the experiments. The released energy can throw fragments and destroy expensive equipment inside the specimens chamber e.g. EBSD-detector. More detailed images of the deformation at low magnification will be presented in the next sections.

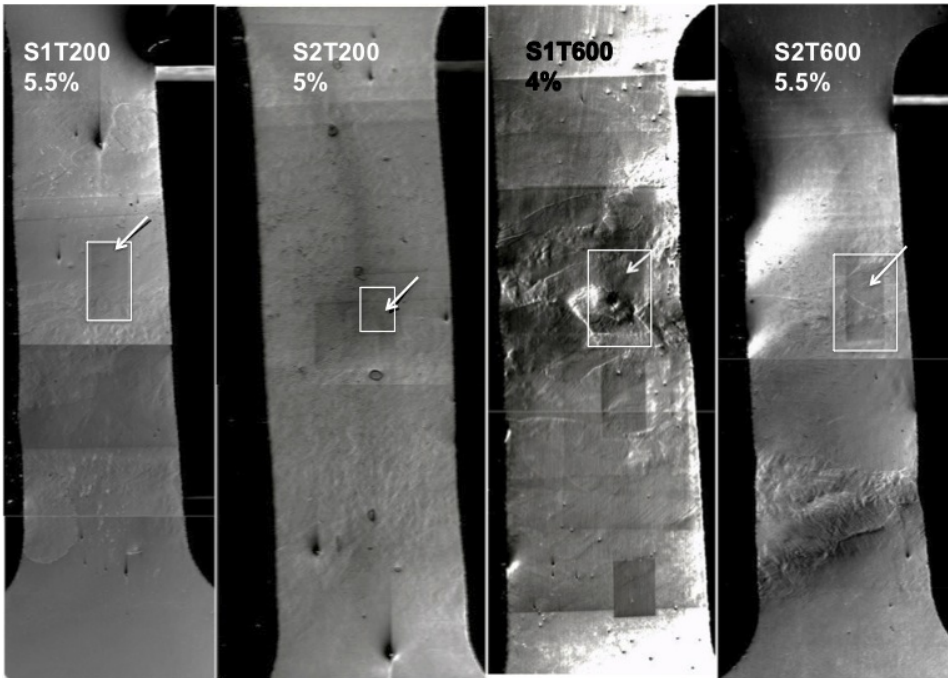


Figure 31: SE-images of the in-situ specimens after final deformation. SE-images originally at 61X magnification. (scalebar not attached because the images are out of proportion because of copy-pasting of several images).

5.2.1 Important Observations from the In-situ Tensile Tests

It is important to note that the given percentage elongation of the different in-situ specimens given throughout the results are not accurate values. For instance should the Ti6Al4V-alloy only accommodate approximately 0.8% elastic deformation according to the literature, while the stress-strain curves obtained in Figure 50 in section 5.5 indicated an elastic elongation of up to 3%. The wrongly indicated elongation by the traction-software will be discussed in section 5.5. However, it is the qualitative information from the in-situ tensile tests which is of interest.

Note that the in-situ specimens tensiled were extracted from different positions in the blocks. This was presented in section 4.2. In addition did the specimens contain different numbers of deposited layers. See Figure 32 below. The conditions for comparing the deformation mechanism are therefore not identical.



Figure 32: The T200 specimens contains two deposits, while T600 only contains one. This is expected to give microstructural variations between the specimens.

5.3 Deformation at Macro Level

The following section will present brightfield images of the in-situ specimen after deformation. The locations of the EBSD-scan could not be identified to the macroetched images because reference points in the SE-images in Figure 31 were lost after etching. However, the deformation behaviour of the specimens at a low magnification can be easily observed as generally darker areas in the brightfield images. The higher magnification images with EBSD follows in section 5.4.1.

S1T200 brightfield at 5.5% elongation

Some activity can be seen along prior β -grain boundaries in image 1. However, the specimen was relatively uniformly deformed. Close-up image of the deformed grain boundaries in 1 can be found in Figure 34.

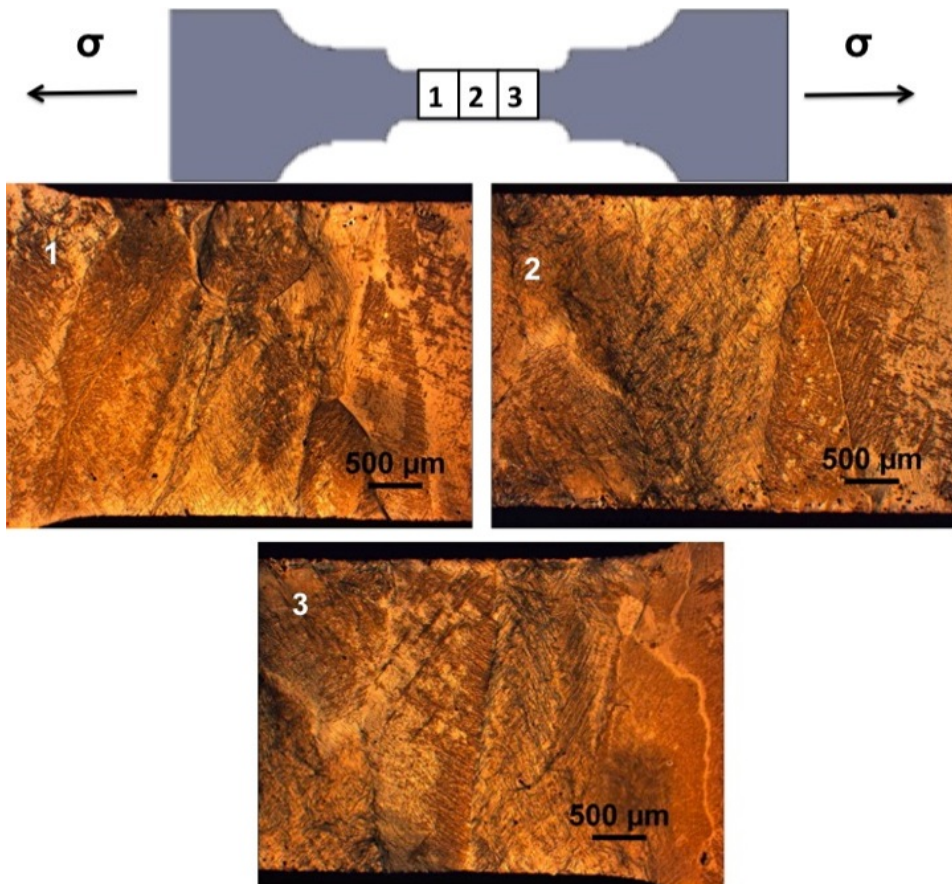


Figure 33: 2.5X Brightfield images after Kroll-etch. The position of the images are indicated in the top image of the specimen.

Close-up Image of S1T200

The deformation of this specimen was located at intersected β -grains at both top and below location of the in-situ specimen. Arrows are added to the image in deformation-rich locations. The interior of the specimen have very few visible marks.

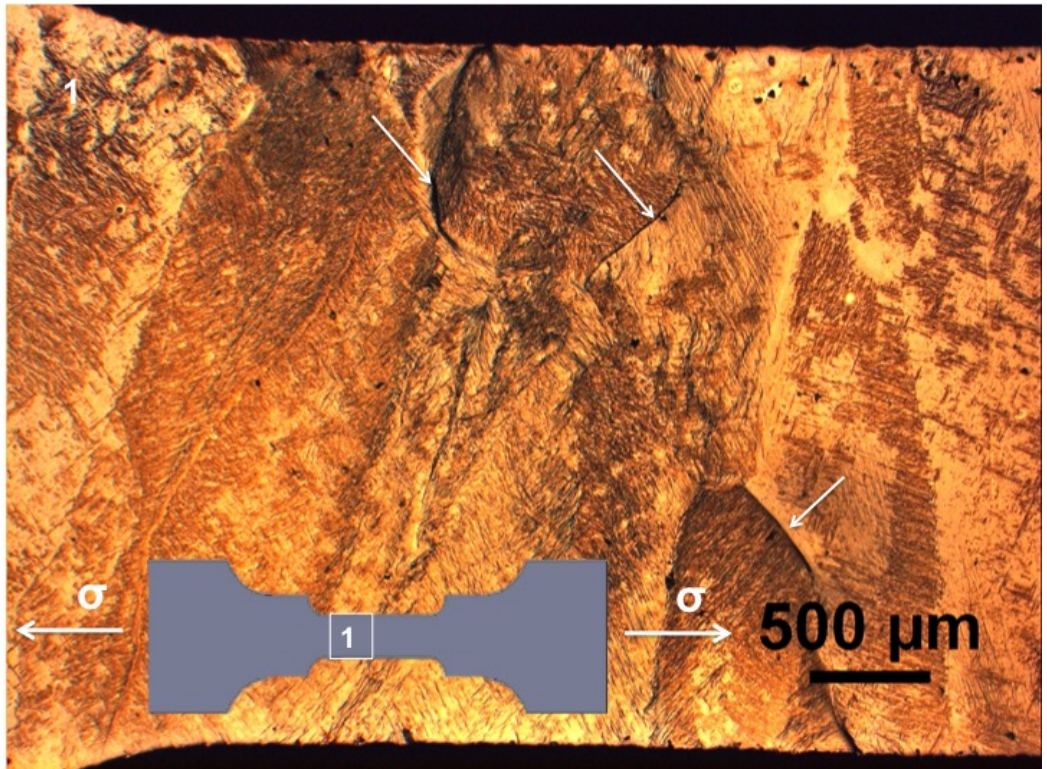


Figure 34: 2.5X Brightfield image. Note the deformation at prior β -grain boundaries.

S2T200 brightfield at 5% elongation

Several narrow columnar β -grains have their orientation transversely to the tensile-direction. They are approximately $500\mu\text{m}$ in thickness corresponding to the length of the scalebar. Their lengths seems also to be longer than the width of the specimen i.e. vertically in the image. The width of the specimens is 3mm for comparison. Little activity could be seen on this specimen at this magnification. However, the close-up image in Figure 36 indicate activity at several locations.

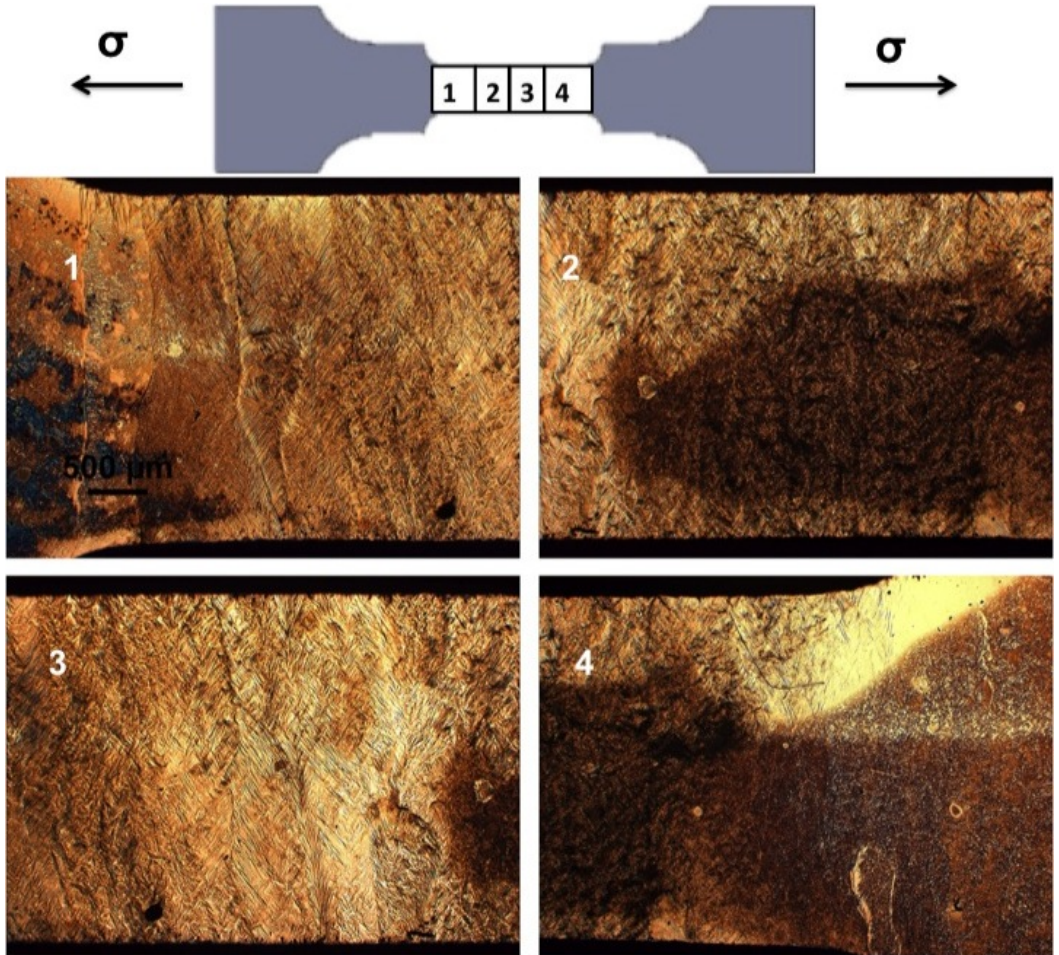


Figure 35: 2.5X Brightfield image. (The missing scalebars should be the same as in the left top image). The "shadow" in image 2 and 4 is a stain after etching.

Close-up Image of S2T200

The slipbands located in proximity to the prior β -grain boundary in the lower image below appeared to have emitted from the grain boundary and they have a weak tilting relative to the grain boundary. However, slipbands can also be observed in the interior of a β -grain to the right in the same image.

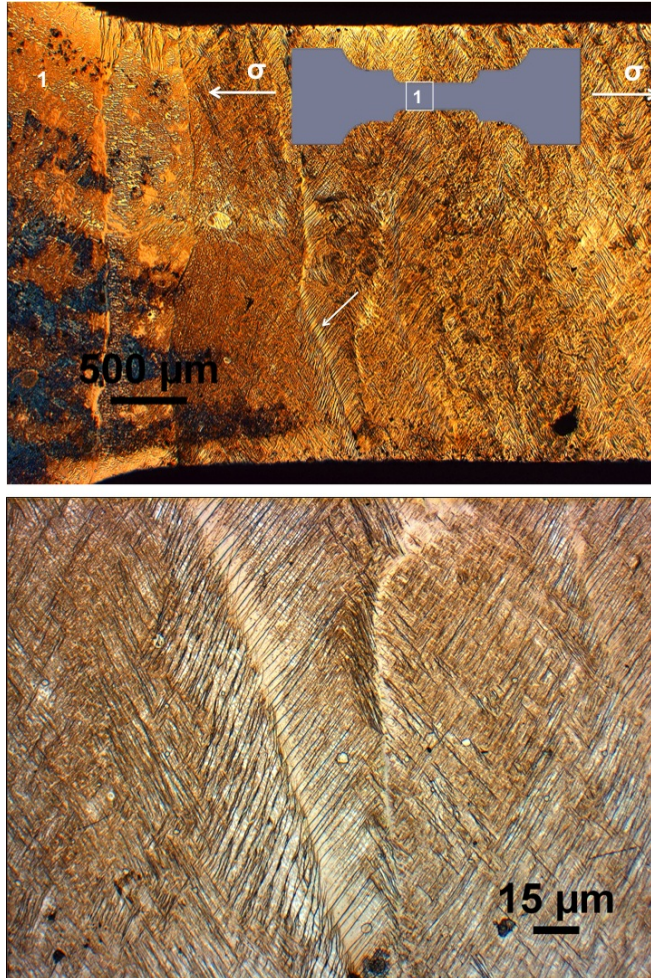


Figure 36: Top: 2.5X Brightfield image. Below: 50X. Position of 50X are indicated with arrow. Large activity on prior β -grain boundaries can be seen.

S1T600 brightfield at 4% elongation

This specimen had seemingly several different deformation mechanisms. Deformation at prior β -grain boundaries, slipbands, and a beginning crack in the lower right corner of image 2. Deformation can be seen especially in the lower left corner of 2, at the grain boundary in the center of 3, and slip bands at the diagonal of 1 and 2.

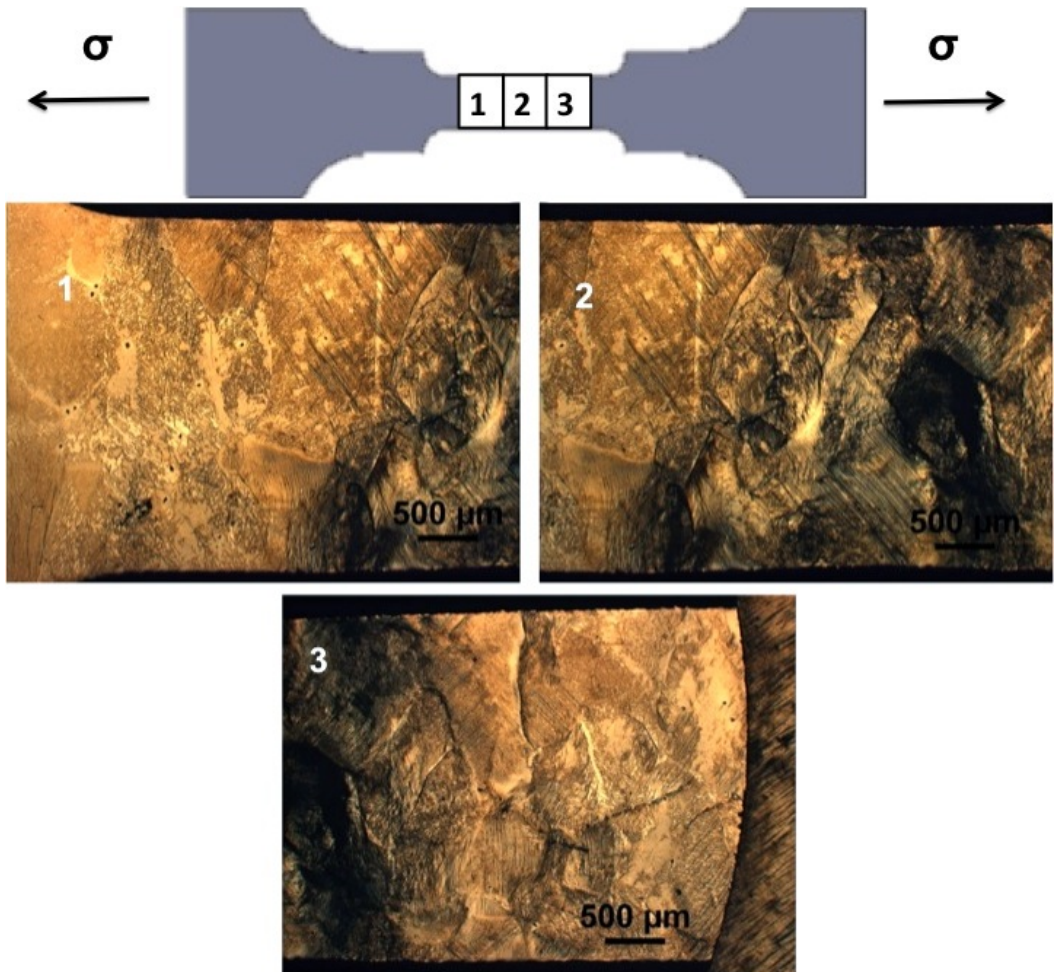


Figure 37: 2.5X Brightfield images. Several different deformation behaviours can be seen.

Close-up Image of S1T600

This specimen contained most slipbands of the four specimens. They can be seen in several locations of Figure 38. For instance in the upper and lower left corner. However, they seem to be located in proximity to prior β -grain boundaries.

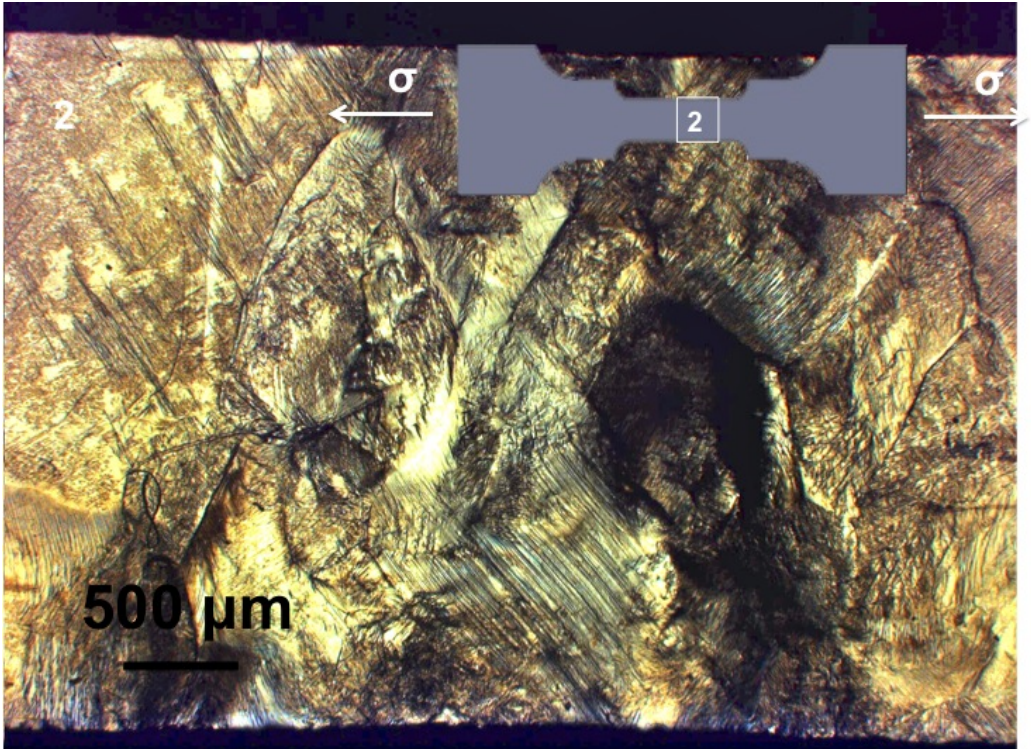


Figure 38: 2.5X Brightfield images. Note diagonal slip bands in the image and the severely deformed dark area in the lower right corner.

S2T600 brightfield at 5.5% elongation

The β -grains in this specimen were very large in some regions. Particularly in 1 measuring approximately 0.1mm in thickness. Activity can be observed at several locations along prior β -grains. However, this specimen have a very local deformation in image 4. Diffraction of the light will be seen as dark regions because of topography.

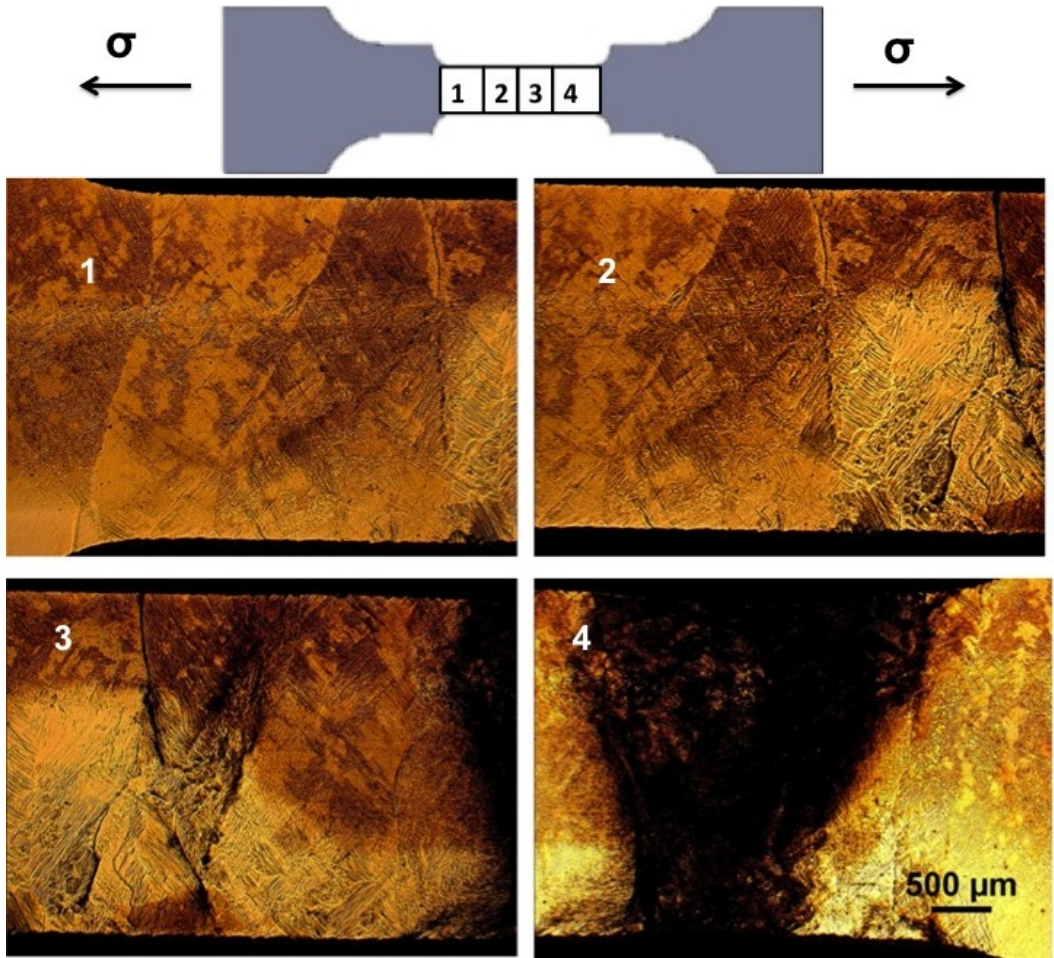


Figure 39: 2.5X Brightfield image. Note the darker areas along prior β -grains, compared to other regions of the specimens. (The missing scalebars should be the same as in the lower left image).

Close-up Image of S2T600

In Figure 40, a β -grain boundary with very distinct behaviour compared to the grain boundary in Figure 36 can be observed. This grain boundary have slip bands at only one side of the grain boundary in contrast to Figure 36 which have slipbands on both sides.

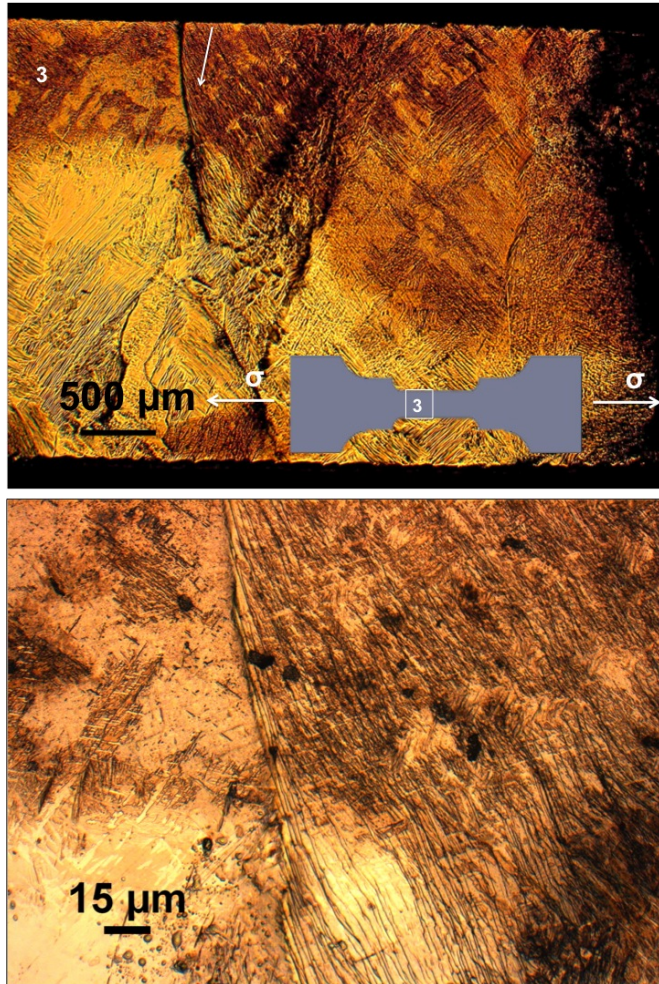


Figure 40: Top: 2.5X Brightfield image. Below: 50X. Position of 50X are indicated with arrow. Deformation tend to follow the grain boundary in this image.

5.4 Deformation at Micro Level

5.4.1 S1T200

No deformation was observed before 4.5% elongation in the IPF-maps in Figure 41 below. The first black pixels because of severe deformation of EBSPs appeared inside the very fine-grained region consisting of green and purple grains. Unindexed pixels are indicated with arrows. The homogeneous green region to the left is primary α -phase along a prior β -grain boundary.

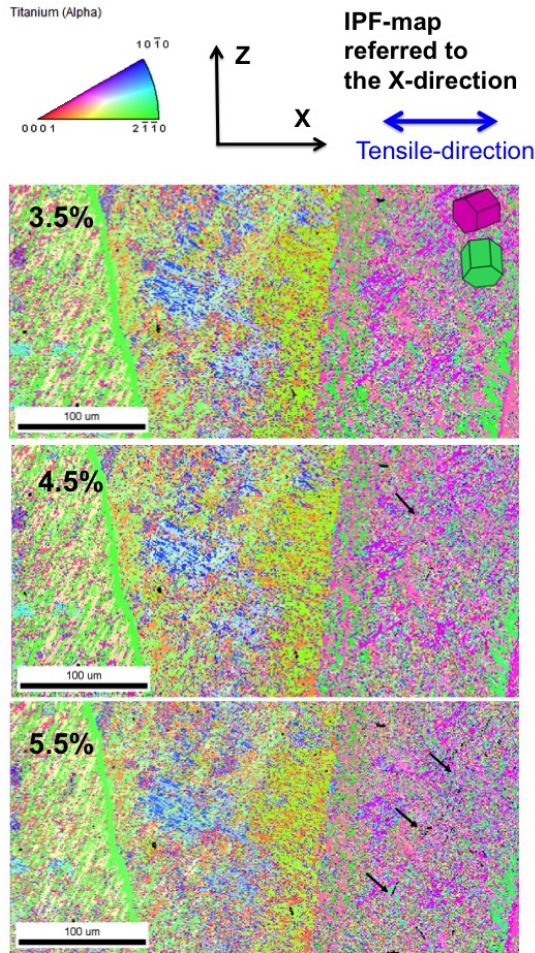


Figure 41: Magnification 150X, step size $0.8\mu\text{m}$, probe current $I_p \approx 37\text{nA}$.

The region surrounding the primary α -phase performed much better in this specimen. This can also be seen from the ROI in Figure 42. The grain combinations in the most deformed regions are given by the two unit cells.

Region of Interest S1T200

From the SE-image in Figure 42 below can the total deformation be observed more easily than by the IPF-maps in Figure 41. At 5.5% elongation, half the ROI in the SE-image is deformed, while the other half have no visible marks. The points distributed over the ROI are calibration patterns used to index the EBSD-scan in TSL OIM Data Collection 5.32 indexing software. Their function and numbers were discussed under theory section 2.11. The primary α -phase in Figure 41 is located approximately at the position of the arrow. The c-axis is oriented approximately perpendicular to the tensile direction for this phase.

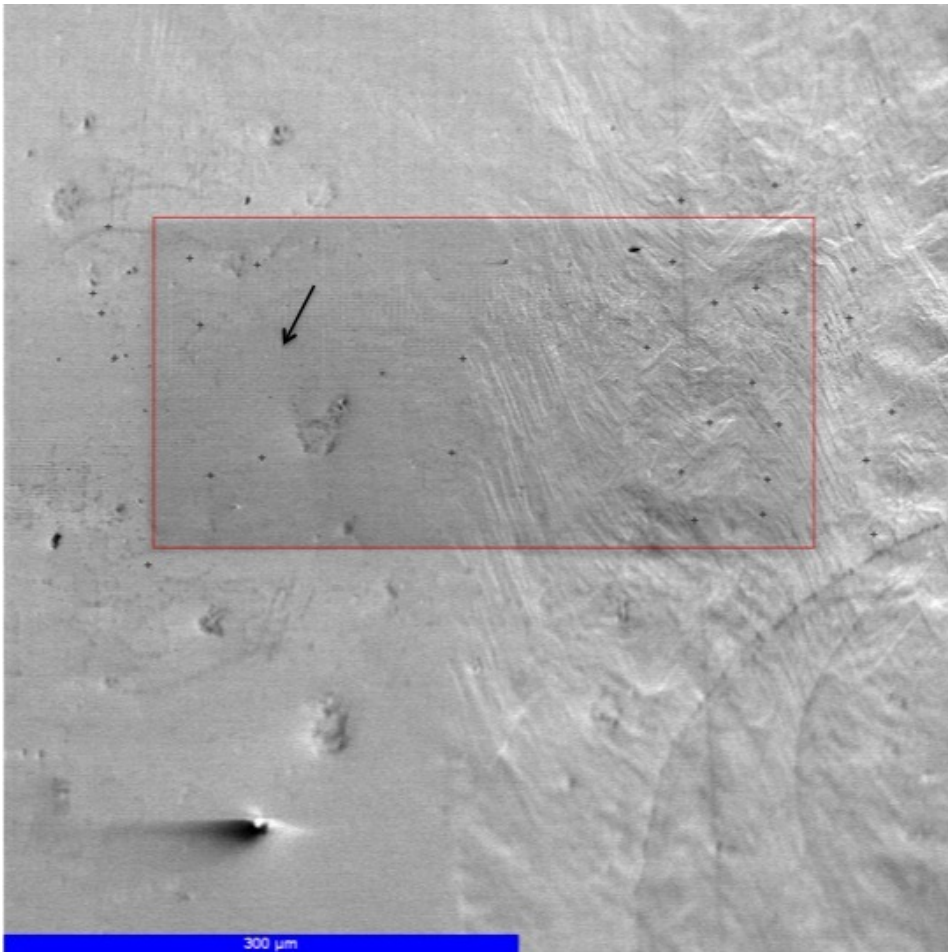


Figure 42: Magnification 150X. Topography after deformation can be more easily observed by SE-imaging.

Close-up on Deformation Mechanism S1T200

Higher magnification and smaller step size were selected to reveal the deformation mechanism behind the unindexed pixels in Figure 41. See Figure 43 below for higher magnification images. Deformation is located between green and purple grains. It can be observed that the cracks follows the interface between the green and purple grains. At position 3, several cracks have merged together where a plate with a distinct orientation have stopped their movement. The IQ-maps to the right were added for comparison. The size and extent of the cracks can generally be more easily observed from this map compared to the IPF-map. Combined they provide more information.

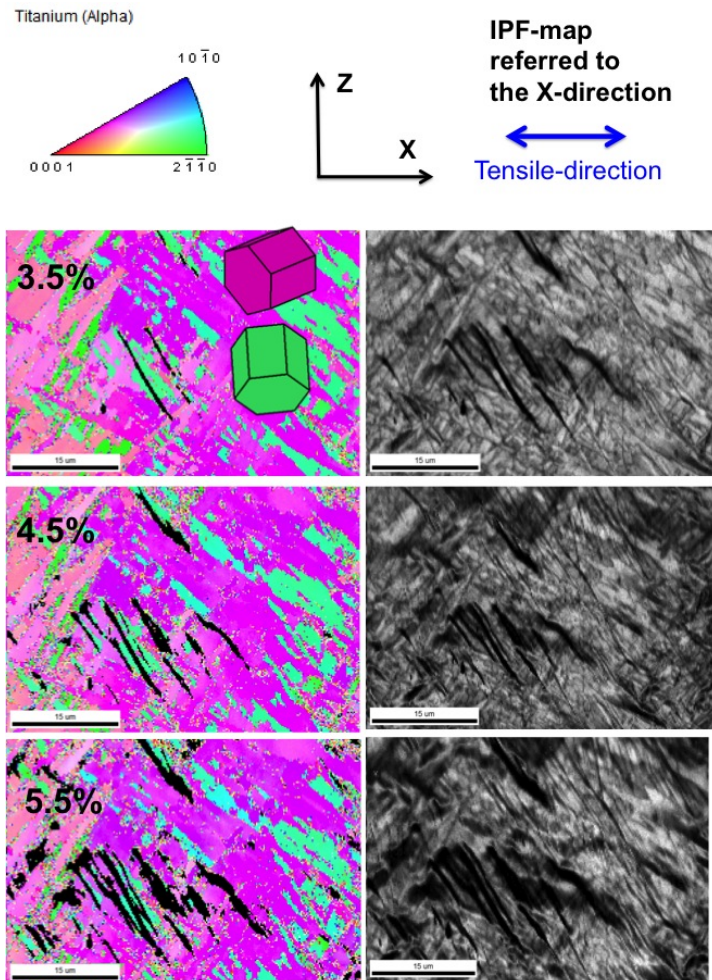


Figure 43: Close-up image of tensile specimen S1T200. Magnification 1000X, Step size: $0.2\mu\text{m}$. $I_p \sim 35\text{nA}$. Scalebar= $15\mu\text{m}$. Left: IPF-map, Right: IQ-map.

5.4.2 S2T200

A very similar area of the microstructure as in S1T200 was selected for S2T200. However, in this case was the most severe deformation located close to and on the prior β -grain boundary decorated with purple primary α -phase. Slipbands are growing from both side of the grain boundary, but only the ones located below the grain boundary are visible from the EBSD-scans. From the SE-images to right these slipbands appeared darker than the surroundings. This was in contrast to the brighter slipbands above the grain boundary which were not detected by EBSD.

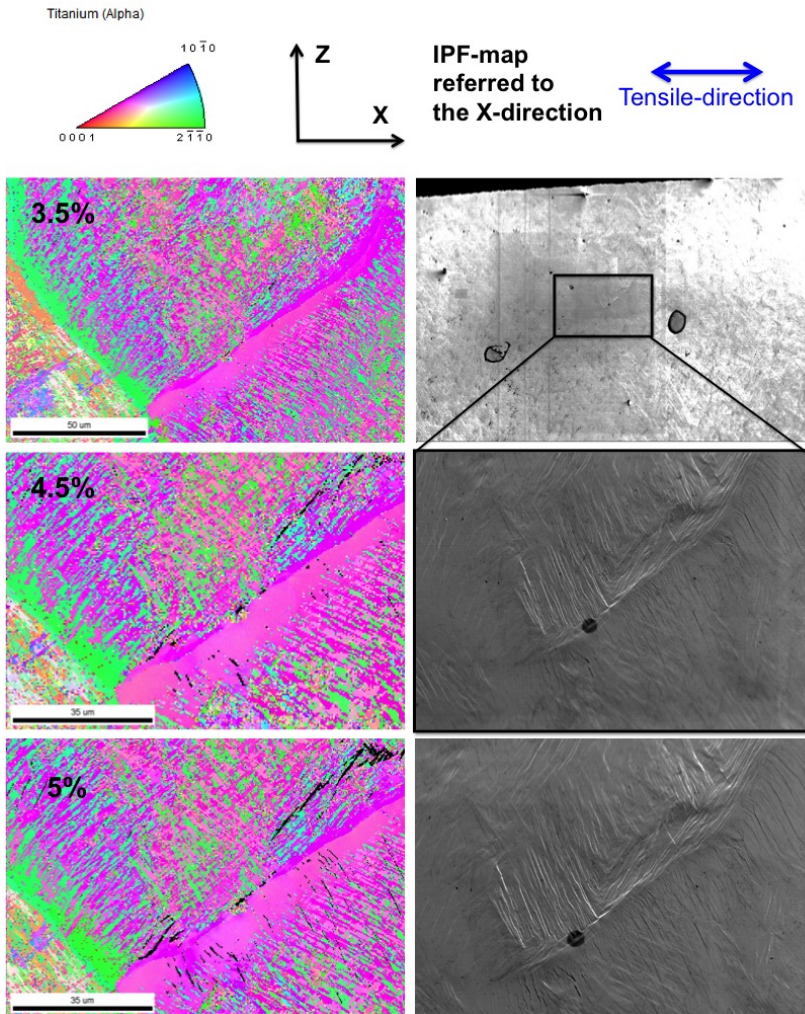


Figure 44: Top: magnification 400X, step size $0.4\mu\text{m}$. Center and below: 600X, $0.25\mu\text{m}$. Magnification SE-images: top: 100X. Center and below: 800X. $I_p \sim 36\text{nA}$. Scalebars= $50\mu\text{m}$ (top), $35\mu\text{m}$ (below).

Close-up on Deformation Mechanism in S2T200

It can be seen from the IQ-map in Figure 45 that the slipbands seems to emitted from the grain boundary and propogate through the α -colony below the grain boundary. The slip bands are following the direction of the plates inside the α -colony growing from the green grain boundary α , while the slipbands in the purple colony seems to have an independent growth-direction. The IPF-figure is not attached because it is the same as in Figure 44.

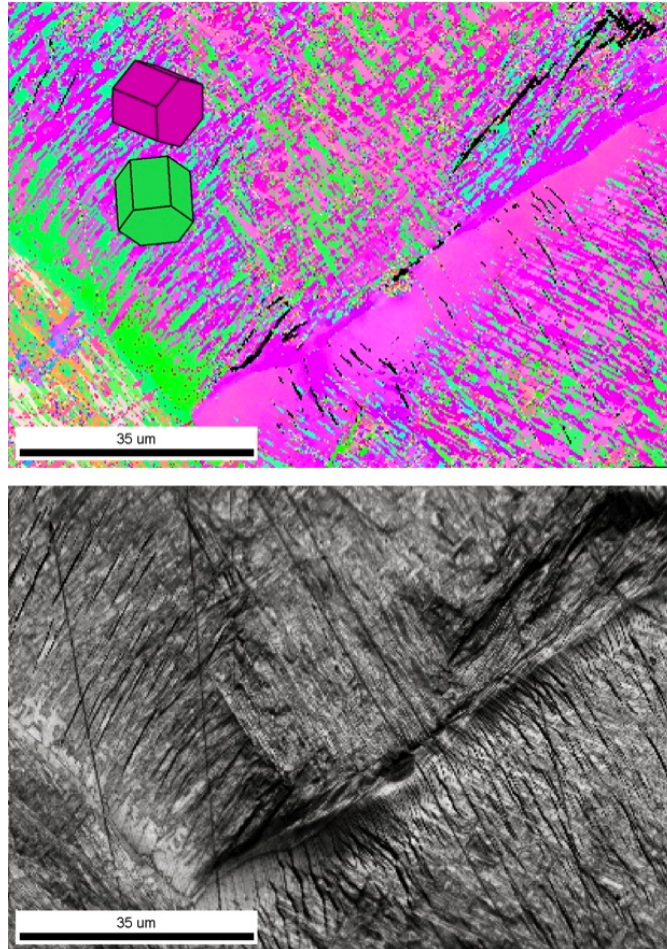


Figure 45: Top: IPF-map. Below: IQ-map. 5% elongation.

5.4.3 S1T600

The first cracks appeared at 2.5% elongation, in the region between the green-orange and blue area i.e. very close to the particle or void close to the center of the image. Deformation by slip bands are indicated with circles and other deformation mechanism with arrows. New arrows between each elongation also indicate the order of appearance of new deformation. It is clearly that slipbands visible in SE-image are not visible in the IPF-map. Note also the change in orange colour. This may be a results of deformation or slightly different indexing. Region along the largest crack in the image have a more pronounced orange colour at larger elongatons, than at shorter elongations.

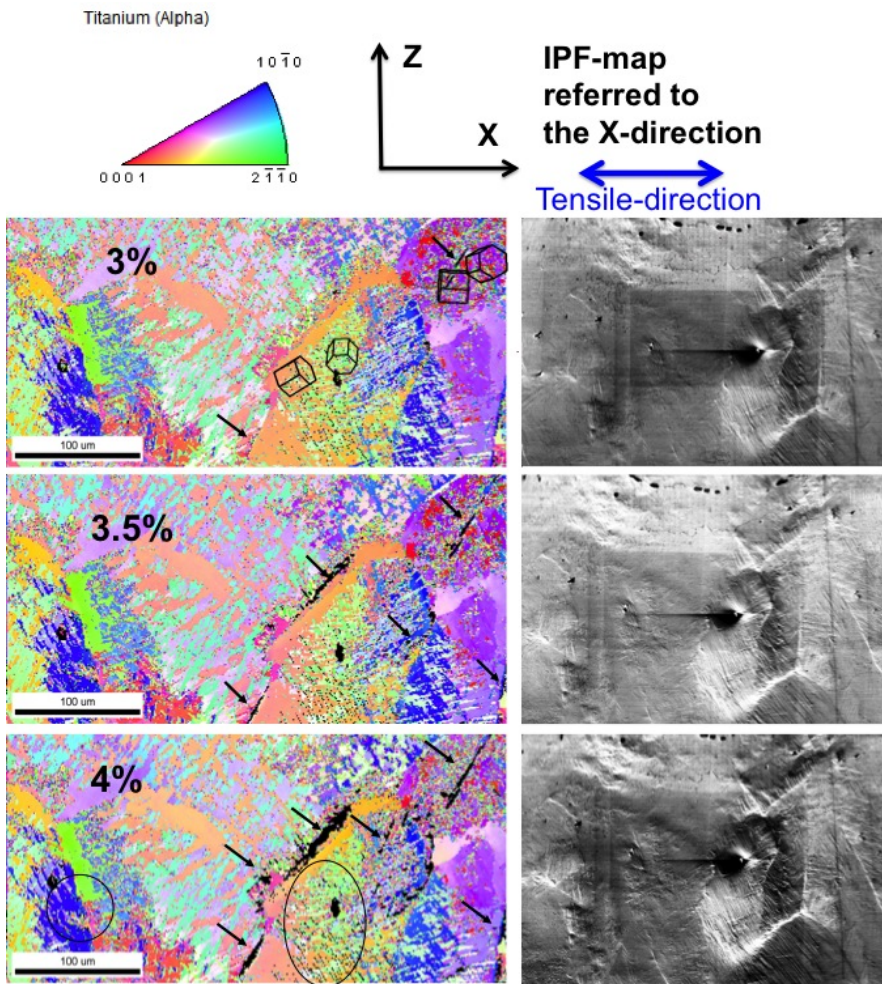


Figure 46: For all images: Magnification 150X, step size $1\mu\text{m}$, $I_p \sim 37\text{nA}$.

Close-up on Deformation Mechanism S1T600

The HCP-unit cells are drawn into the image where the most severe deformation was observed. The unit cells mark the orange, green, purple, and red grain orientations. Slip bands emitting from the large crack at the center can be easily seen in the IQ-map below. These were mainly located between orange and green grains. Note also the generally darker area in the IQ-map and the corresponding continuous purple area of the microstructure to the right in the IPF-map.

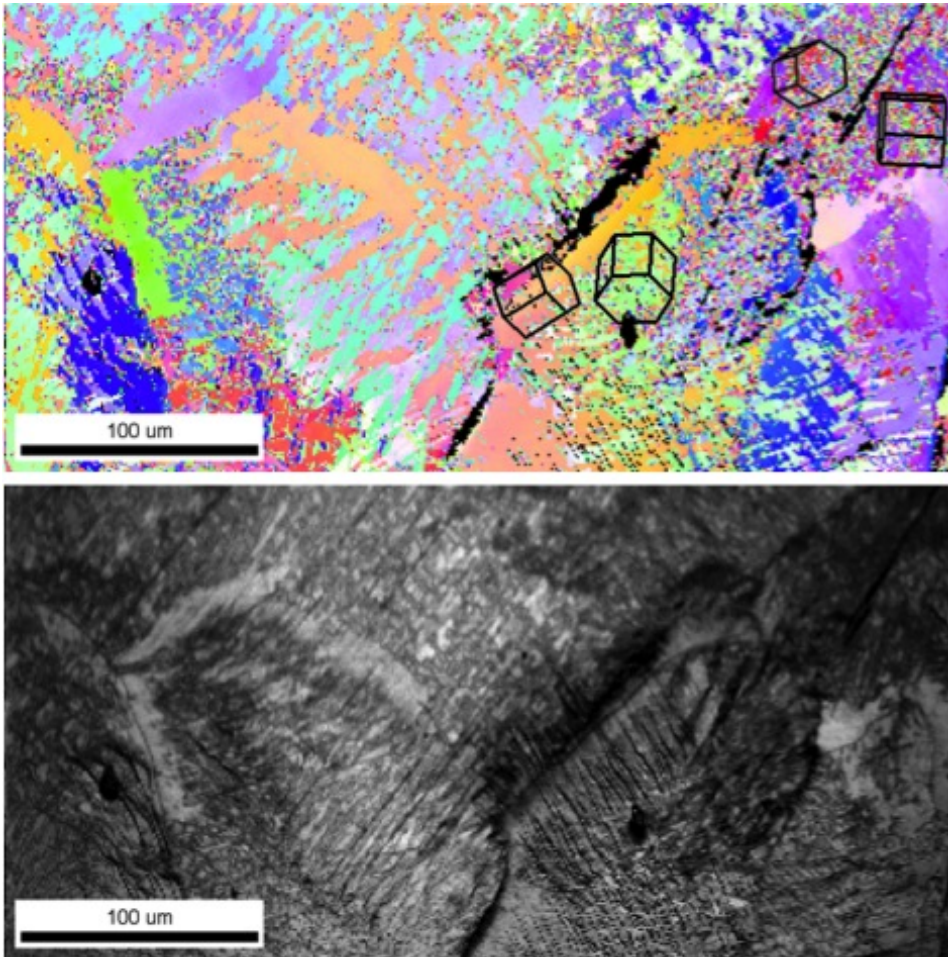


Figure 47: Top: IPF-map. Below: IQ-map. 4% elongation. 150X. The IPF-figure can be seen in Figure 46.

5.4.4 S2T600

From the SE-image to the right at 2.5% elongation can two deformation bands along prior β -grain boundaries be seen. The later deformation appeared to propagate from these two bands. The only visible deformation at 5.5% elongation in the IPF-map was located between the green and purple grain orientations in the left lower corner. An additional EBSD-scan was performed in the region marked with «colony» to have a more accurate imaging of the colony seemingly to be free from deformation. This can EBSD-scan can be seen in Figure 49 on the next page.

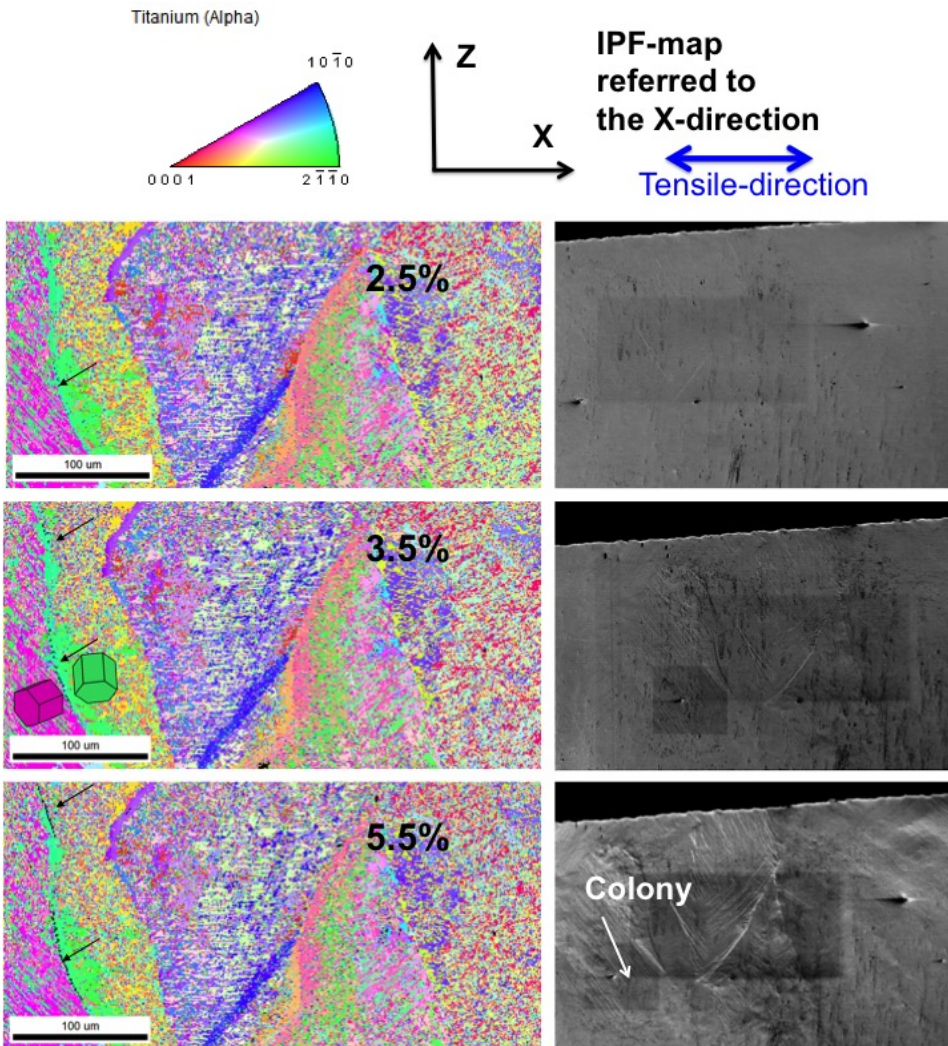


Figure 48: For all images: Magnification 150X, step size $1\mu\text{m}$, probe current $I_p \approx 37\text{nA}$.

Close-up on α -Colony and Primary α -phase

For the same grain combination of green and purple grains but different morphologies of the grains can two different behaviours be observed. No deformation could be observed within the α -colony in the top image, while deformation was observed along the grain boundary in the image below. The IPF-maps are from the same elongation of 5.5%.

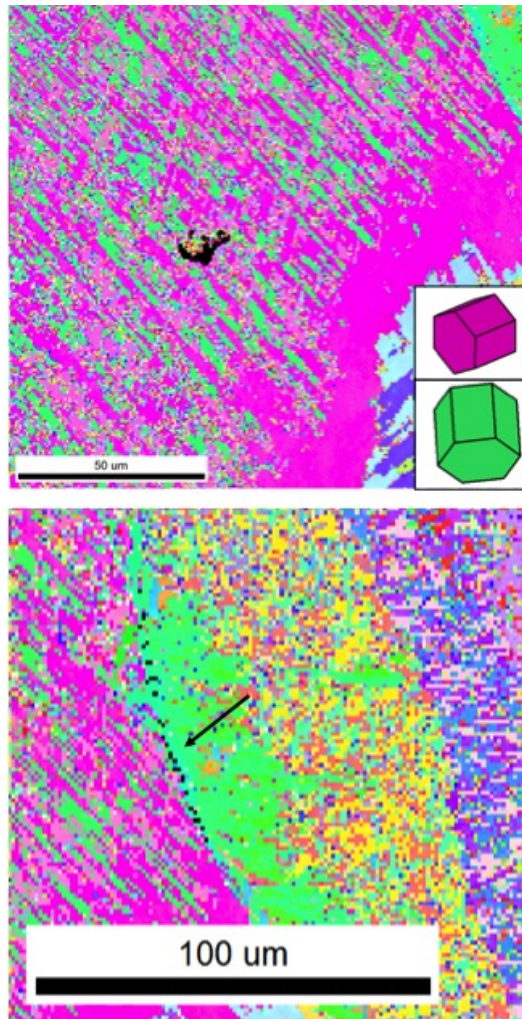


Figure 49: Top: α -colony structure, below: primary α -phase along grain boundary. 5.5% elongation. Arrow indicate unindexed pixels along the grain boundary. Magnification colony: 300X, step size: $0.6\mu\text{m}$.

5.5 Tensile Curves

S1T200 and S2T200 were tensiled to 5.5% and 5% elongations, respectively. S1T600 was stopped at 4.5% elongation. The tensile curve of S2T600 is missing due to a defect in the traction cable which lead to incomplete resetting of the control unit box. Despite the very deformed appearance of S1T600 was this the specimen which obtained the highest UTS-value of 807MPa. However, it was only slight differences between S1T600 and S2T200. The YS of the three curves appeared to be relatively similar ± 25 MPa. The stepwise appearance of the curves, and the different E-modulus will be discussed in section 5.5. Note also the large elastic deformation for the three curves.

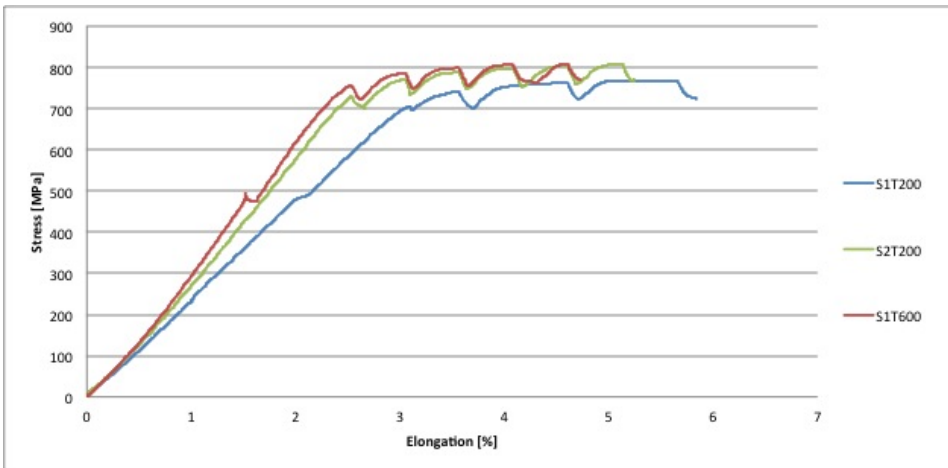


Figure 50: The tensile curves obtained after the different in-situ experiments. Tensile values from S2T600 was not logged.

5.6 Interface Region between Substrate Plate and DMD-Block

Measurements of the grain sizes in different regions of the interface were performed by the intersection method in a lightmicroscope. This was performed by counting intersected grain boundaries and divide on the displacement distance after moving across the specimen from left to right in the image. See Figure 52 on next page for larger images. The columnar β -grains length and width in region 1 were measured to be approximately 3.75mm and 0.6mm, respectively. The equiaxed grain diameter in region 2 were measuring 0.5mm in average. The fine microstructure in region 3 is the so-called bimodal microstructure. The grains here were measuring approximately 0.01mm. The fusion zone is also indicated in the illustration. According to Figure 85 in section 10.19 in the appendix can this zone measure approximately 3mm and the HAZ measure 7mm below the surface.

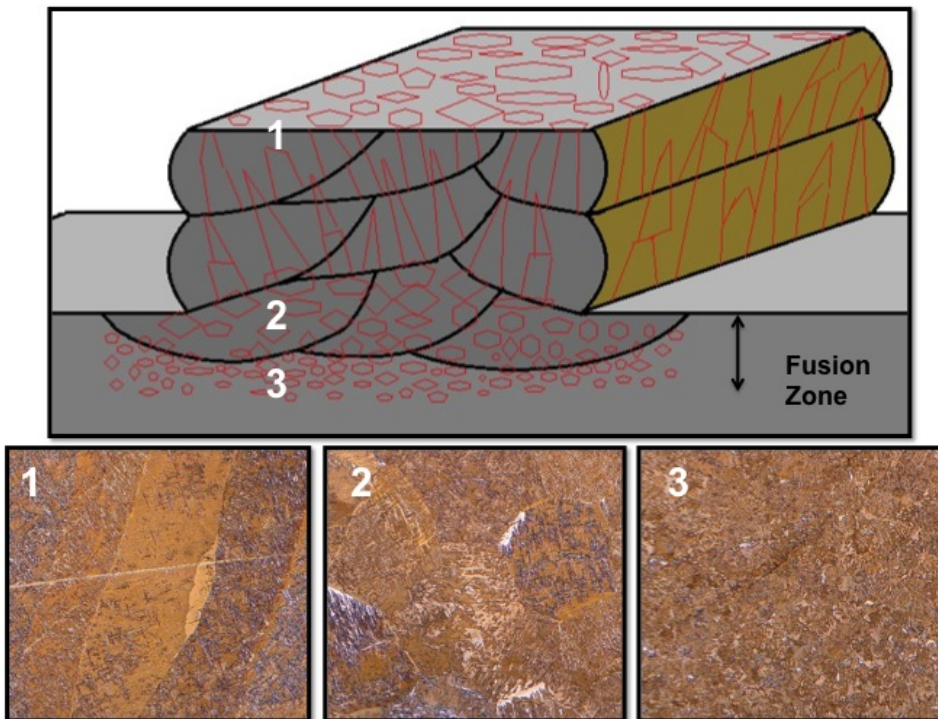


Figure 51: Illustration of the microstructures in the interface region between the DMD-block and substrate plate. Weck's reagent + Kroll etch were used to reveal the different microstructures by light microscope. Magnifications in all images were 50X.

Brightfield Images of Interface Region

The arrow in 1 indicate a grain boundary with a very thin and homogeneous primary α -phase. The indicated region in 2 may be so-called lath martensite or massive martensite which is often observed for high cooling rates of welded near- α -titanium alloys. The microstructure in the bimodal plate was very fine because of deformation induced recrystallization after hot-rolling.

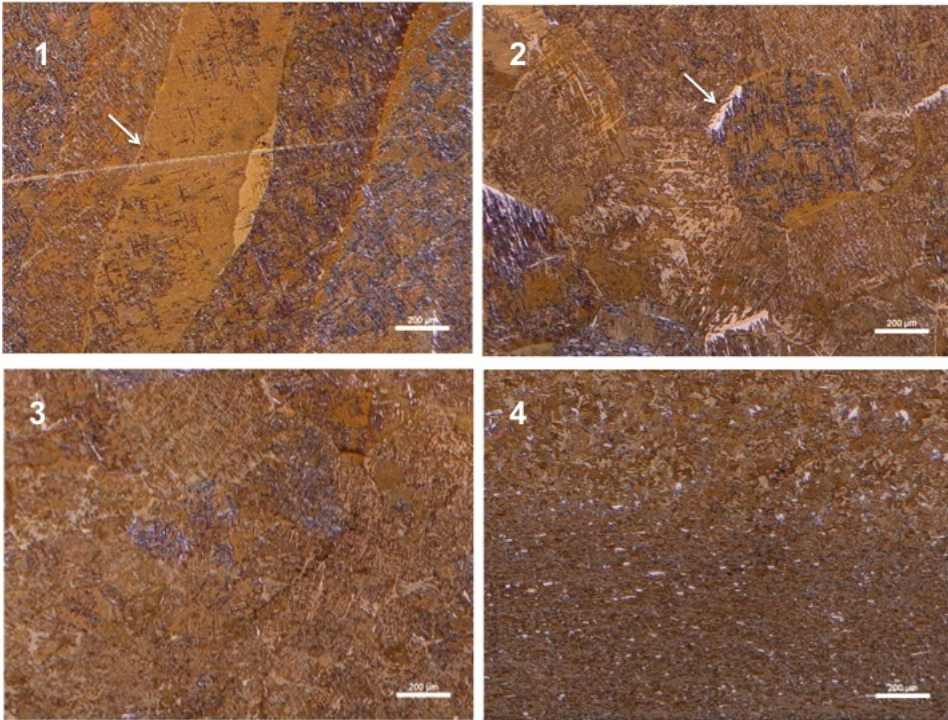


Figure 52: Magnifications 50X for all images. Etch-type: Kroll + Weck's. Scalebar =200 μm . From block T200

IPF-Maps of Interface Region

The same specimen as in Figure 51 was investigated at 100X magnification by EBSD. This was performed to observe in detail how the transformation from small equiaxed grains inside the substrate plate gradually changes into columnar β -grains. Several IPF-maps were taken at different positions of the interface. The numbering of the images appears in the same order as the numbering in Figure 51. The first columnar β -grains close to equiaxed grains, appeared to be smaller than the columnar β -grains farther away from the substrate plate. For instance did the columnar grain in 1 measure only 1mm in the Z-direction. Referred to the global axis in Figure 21. The step size used for the images below was calculated from equation (2) presented in the theory i.e. Step size (nm) = $\frac{80246}{100} = \sim 802\text{nm} = 0.802\mu\text{m}$.

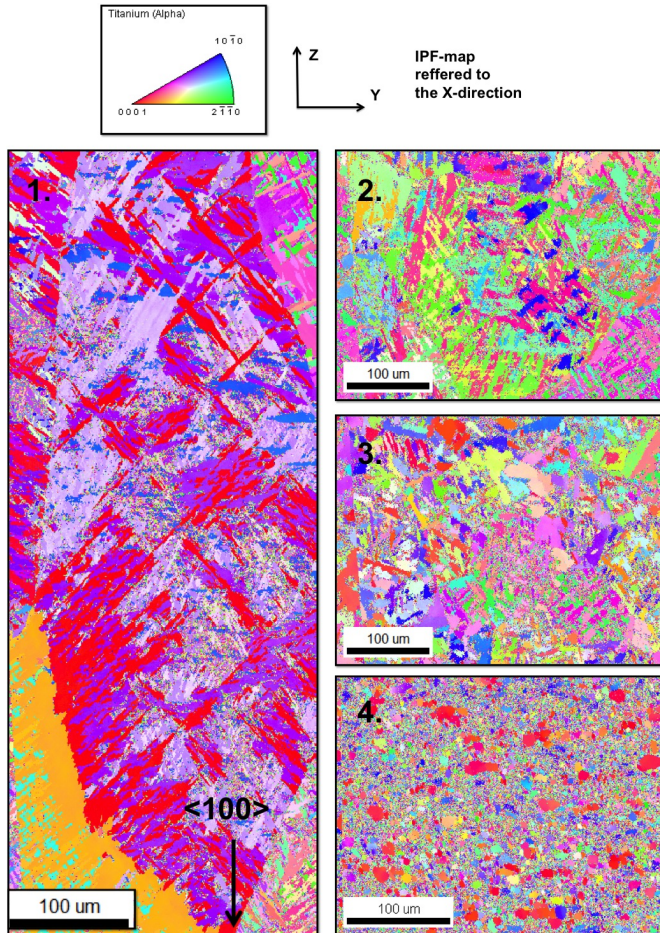


Figure 53: Magnification 100X, step size $0.8\mu\text{m}$, $I_p = \sim 84\text{nA}$ for all the images.

An artifact can be observed in image 1-3. The microstructure to the right continuously mistakingly to the left. This was caused by a defect in the hardware trigger mode in the CCD-camera system. The hardware trigger mode was replaced by a software trigger mode in the NORDIF 1.4.0 which could not have fast enough updates for the 400 frames per second used.

The microstructure transforms from very fine rolled bimodal microstructure in the plate 4, to equiaxed grains with various diameters at different position below the surface 2 and 3, before columnar β -grains and platelet microstructures appear in the block 4. See also Table 34 for quality parameters of the EBSD-maps in 1-4 after indexing.

In Figure 54 below was polefigures attached to the images, to illustrate the gradually development of texture. Clustering of points in the polefigure indicates that several grains have close orientations and that the material have a weak texture. For highly textured materials, are nearly all grains restricted to one part of the pole figure. How to interpret pole figures can be found in section 10.20 of the appendix.

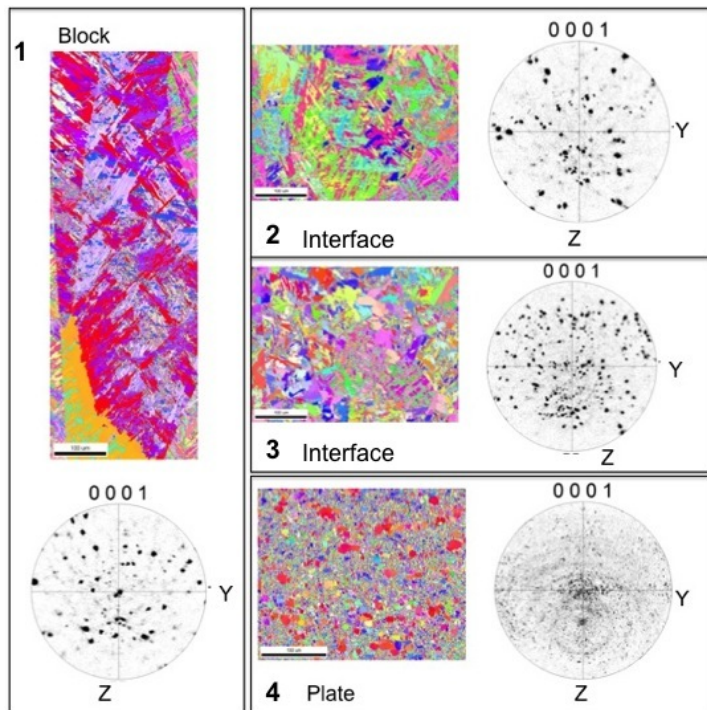


Figure 54: Development of texture between substrate plate and block. A weak texture can be seen in 1. Scalebar= $100\mu\text{m}$ for all images.

5.7 Grain Boundary α -Distribution along prior β -Grains

Measurements of the thickness of the primary α -phase in both blocks were performed, indicating that T200 had a slightly coarser grain boundary α . T200: $37.9\mu\text{m}$ and T600: $33.7\mu\text{m}$. The measurements were performed in the OIM Analysis 6.0 software by using a scalebar in the Y-direction (while keeping Z-coordinate constant) of Figure 55. See Table 26 in appendix for the measured values.

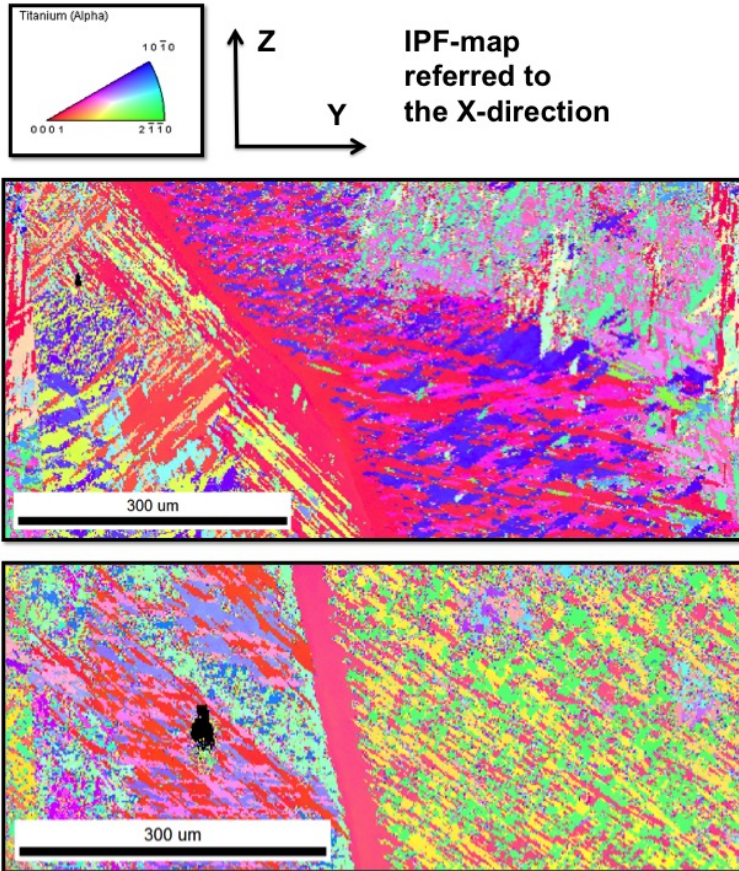


Figure 55: Top: T200. Below: T600. Magnification 100X, Step size $1.5\mu\text{m}$, $I_p \approx 43\text{nA}$. Location of both specimens was at the center of the blocks giving comparable conditions and cooling rates.

The possible BOR along prior β -grain boundaries can be seen in the lower image. The colonies are growing into the right β -grain indicating that the α -phase have a relationship with the right grain. However, the BOR is harder to observe in the top image. Plates seem to grow in both directions from the grain boundary. This is discussed in section 6.4. The α -colony structure seems also to be slightly finer and have grown longer into the β -grain before they were interrupted in T600.

5.8 Effect of Ion Milling on Quality Parameters of the EBSD-map

The ion milling parameters presented in the experimental part was used as a subsequent sample preparation to chemical-mechanical polishing to improve the quality parameters of the EBSD-map. The motivation for this was that the relatively low qualities for the parameters. EBSD-scans were performed over the same region of the microstructure before and after ion milling. The same region in the microstructure could be found by making a mark with a scalpel. Hydrocarbon deposition was considered as a negligible factor for reducing the overall quality of the parameters since the hydrocarbon layer was removed by the ion milling sequence. The deformation after the scalpel was to large to be removed by the ion milling. The effect of the ion milling sequence on a fine-grained region of the microstructure can be seen in Figure 56.

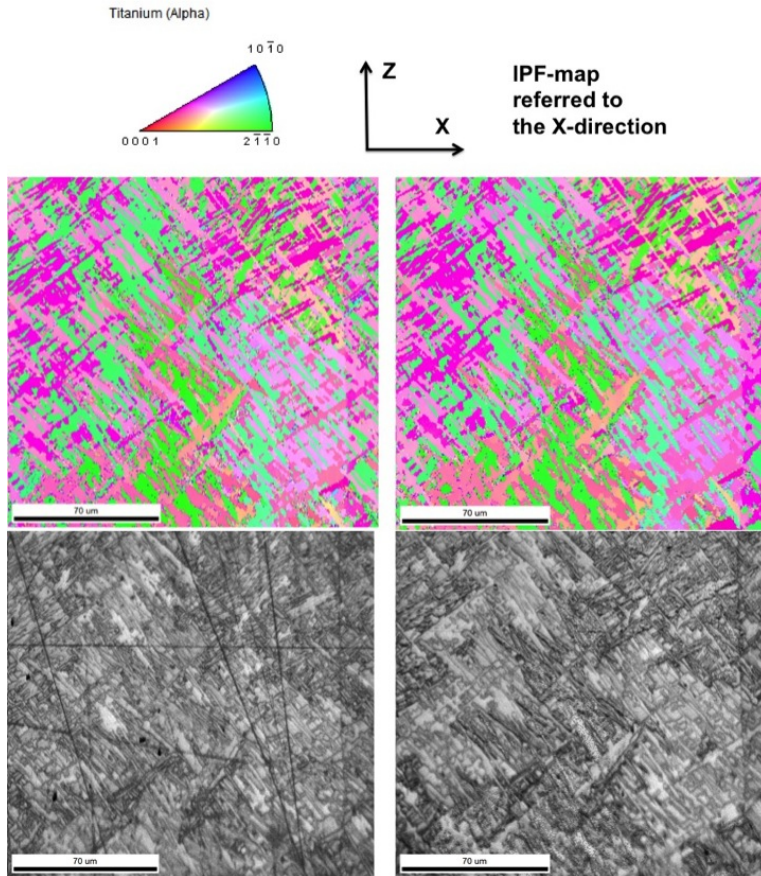


Figure 56: Left: Not ion-milled. Right: ion-milled. Magnification 400X, step size $0.5\mu\text{m}$. $I_p \approx 83\text{nA}$.

The quality parameters of the EBSD-map can be found in Table 15. Left images below is without ion milling, right image was ion milled for 30min. The effect of the ion mill could be seen as a removal of the grinding-stripes in the IQ-map. This also explains the improvement in the IQ-value in the table. However, no effect could be observed in the IPF-map. Investigated specimen was from block T200.

Table 15: The table summarises the quality parameters of the EBSD-map before and after ion milling of Figure 56

<i>Figure nr.</i>	<i>CI</i>	<i>IQ</i>	<i>Fit</i>	<i>Nr. of good points/All Points</i>
Fig 56 Not ion-milled	0.43	136.28	1.02	122393/122400
Fig 56 Ion milled 30min	0.42	149.03	0.98	122400/122400

Phase Distribution after Ion milling

For the same area of the microstructure as in Figure 56, could different phase distributions be observed before and after ion-milling took place. Especially the distribution of the β -phase in the region surrounding the grinding stripe was altered. However, the total fraction β -phase was lower after ion milling.

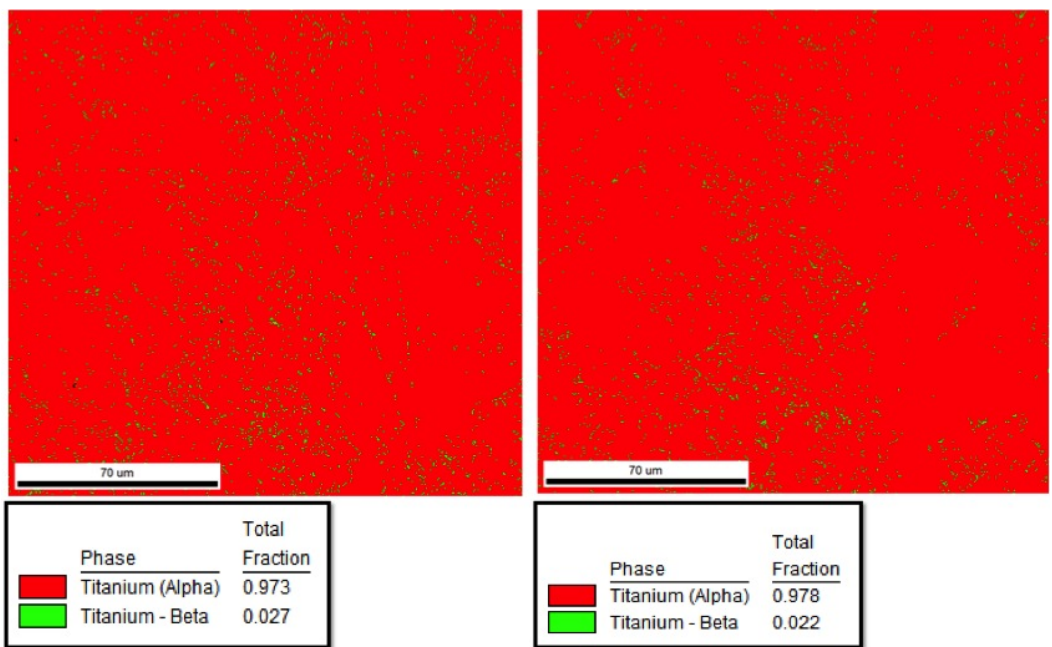


Figure 57: Left: Not ion-milled. Right: ion-milled for 30min. Magnification 400X, step size $0.5\mu\text{m}$.

Phase Distribution at High Magnification and Short Step Size

Ion milling was performed for 1.5 hours to compare the fraction β -phase in the two blocks. High magnification and short step size were selected to have an accurate imaging of the grain boundaries where β -phase should be located according to theory. The fractions β -phase after this experiment can be seen in the tables below attached to the phase distributions maps. Note that these fractions are for non-cleanup conditions in the OIM Analysis 6.0.

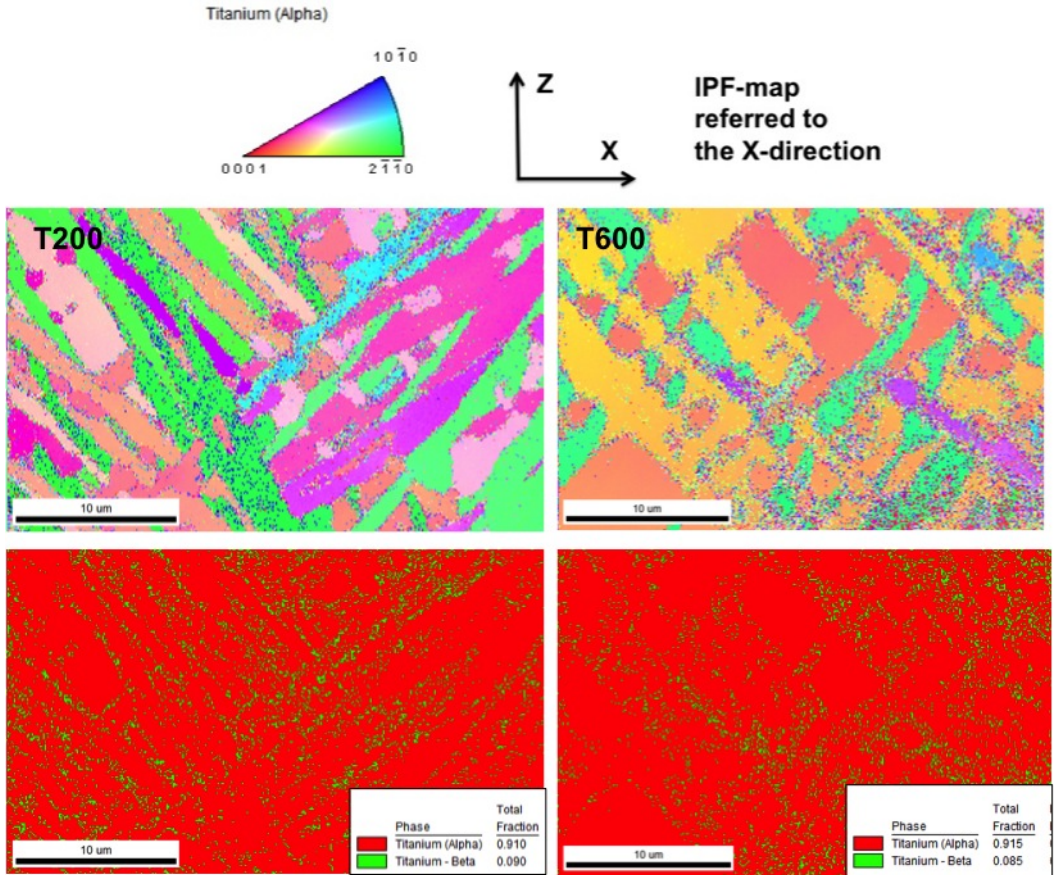


Figure 58: Top: IPF-maps. Below: Phase distribution-maps. Magnification 2000X, Step size $0.1\mu\text{m}$, $I_p \sim 60\text{nA}$.

Confidence Index of β -Phase after Clean-up

Because the β -fractions obtained in Figure 59 were seemingly very high, was even more accurate investigations performed. The EBSD-scan below was taken with the smallest step size and highest magnification used during this work. The image was also filtered with the cleanup function in the OIM Analysis 6.0. A CI-correlation was performed, for $CI < 0.08$. The remaining β -phase after filtration are therefore the most likely to be retained β -phase and not noise. The pixels indicated with the arrow have the following CI-values: 0.114, 0.114, 0.057 and 0.029. From the IQ-map, can very dark regions be seen in the same areas for the β -phase indicating large deformation in the same region. The results was obtained from block T600 after 1.5 hour ion milling with the parameters presented in section 4.1.6. The indexed β -phase was 0.2%.

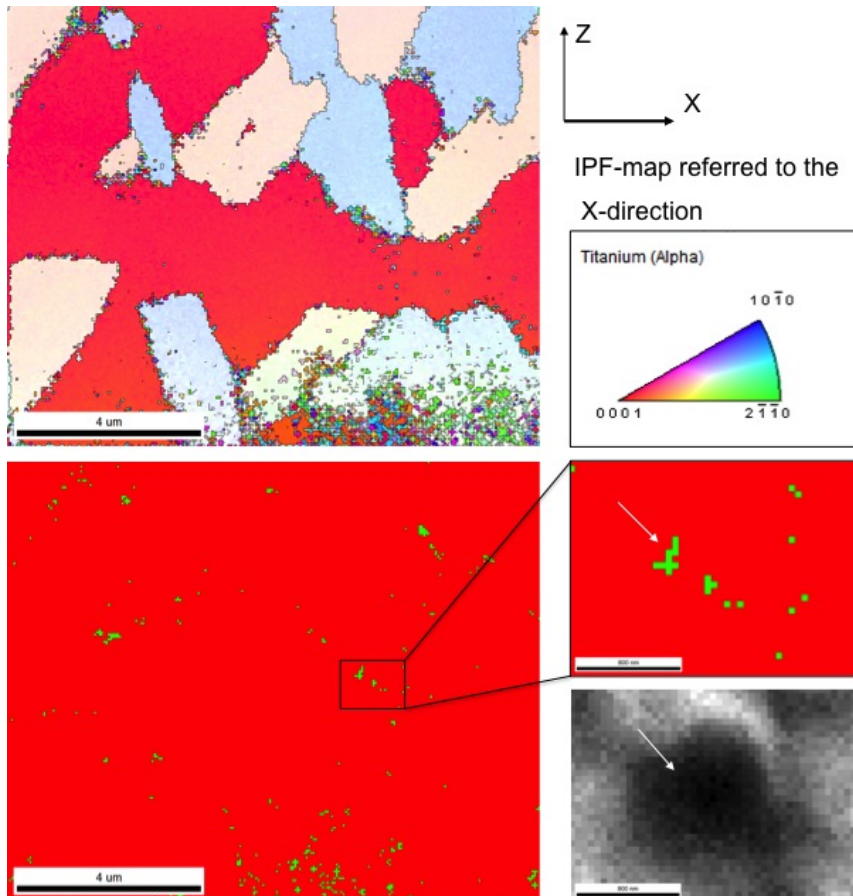


Figure 59: Top: IPF-map. Below: Phase distribution maps. Side: IQ-map. Magnification 6000X, Step size: $0.05\mu\text{m}$, $I_p=60\text{nA}$. Scalebar=800nm of cropped images

5.9 Effect of Probe Current on Quality Parameters of the EBSD-map

Different probe currents i.e. 80nA, 67nA and 50nA, were selected to investigate the spatial resolution which could give the most detailed imaging of grain boundaries. The probe current was calculated from equation 11 in the theory. To give comparable conditions were the calibration patterns of 67nA used to index all the three probe currents conditions. This was performed by copy-pasting the calibration patterns into the respective folder containing the pattern.dat-file of the different probe currents. The quality parameters of the EBSD-maps after indexing are given in Table 37 in the appendix, giving very similar values. The same region was selected and cropped for all three conditions as illustrated in the large image below. The quality parameters of the cropped images are given in Table 16. The minimum CI-value value was set to 0.01 for all conditions.

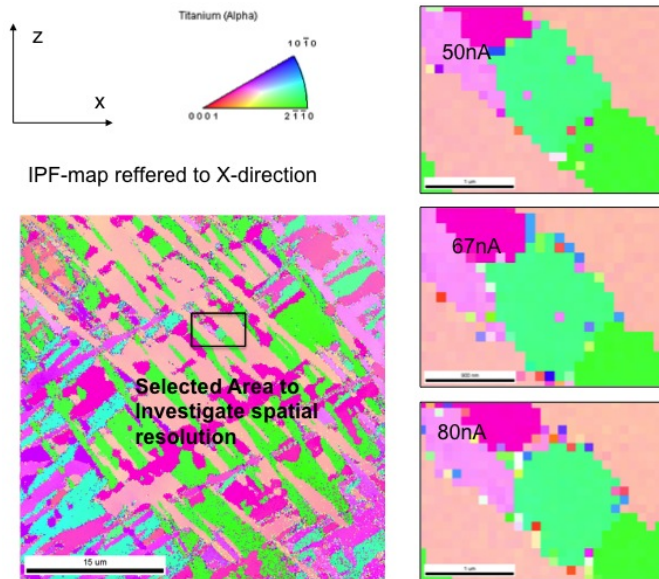


Figure 60: Step size $0.1\mu\text{m}$, Magnification 1000X. The scanning time was correspondingly altered from 5-9min by only adjusting the probe current conditions in the Hitachi Microscope. Scalebar cropped images= $1\mu\text{m}$. Specimen from block T200.

Table 16: The table summarises the quality parameters of the EBSD-map of the cropped images in Figure 60. Their total number of points varied slightly.

<i>Probe current</i>	<i>CI</i>	<i>IQ</i>	<i>Fit</i>	<i>Nr. of good points/All Points</i>
Cropped 50nA	0.46	129.56	1.08	572/572
Cropped 67nA	0.43	132.90	1.07	520/520
Cropped 80nA	0.36	131.33	1.19	432/432

The indexing software did not indicate any bad points for the three conditions for a minimum CI=0.01. From the Figure 61 can it be seen that there are several wrongly indexed points along the grain boundary. Instead they were counted manually for each condition and used as input to the N_{BP} factor in the spatial resolution formula below.

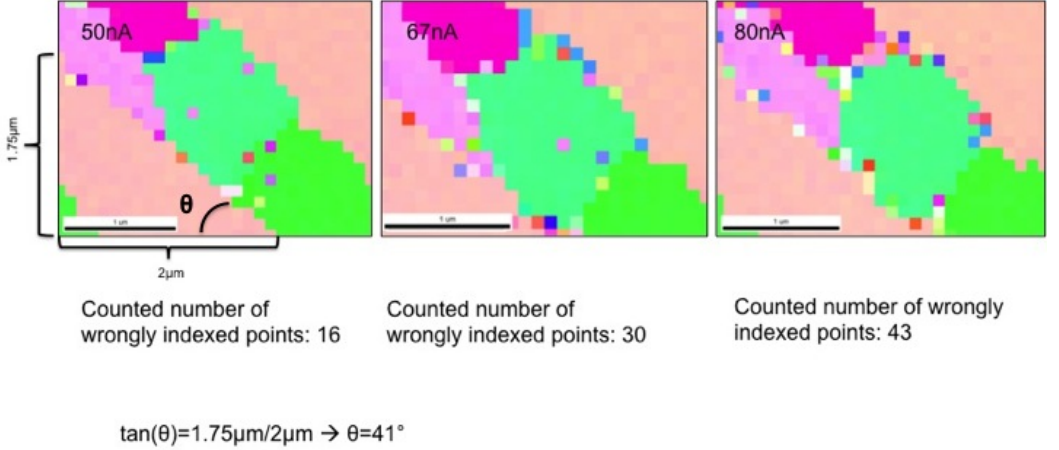


Figure 61: The counted number of bad points are given in the image. The angle θ relative to horizontal direction is also calculated.

The wrongly indexed points were counted manually for each probe current to calculate the spatial resolution from formula 12 below. The angle between the horizon and the grain boundary Θ was also calculated in Figure 61

$$R = \frac{N_{BP}D_s \sin\theta}{\frac{H}{D_s}} = \frac{N_{BP}D_s^2 \sin\theta}{H} \quad (12)$$

The height of the scans are $2.1\mu\text{m}=2100\text{nm}$, the step size D_s was 100nm . The number of bad points N_{BP} (counted wrongly indexed points from the cropped images), are given in Figure 61. Insertion of the numbers into the formula 12 above give the the following spatial resolution for the different probe currents:

$$R(50\text{nA})=50\text{nm}$$

$$R(67\text{nA})=93\text{nm}$$

$$R(80\text{nA})=134\text{nm}$$

5.10 Summary of Quality Parameters of the EBSD-map

Table 17 below summarizes the maximum, minimum and average quality parameters of the EBSD-map obtained during this work. The average values are based on 30 different EBSD-scans. The maximum values were obtained in previous project work for a coarse basketweave region of the microstructure, while the minimum values were obtained close to the rolled bimodal substrate plate. The complete table can be found in section 10.13 in the appendix. The values are for non-cleanup conditions and includes deformed in-situ specimens.

Table 17: Extract from Quality Parameters of the EBSD-maps presented in Table 28-36

<i>Result</i>	<i>CI</i>	<i>IQ</i>	<i>Fit</i>
Average	0.316	96. 25	1.32
Maximum	0.56	134	0.87
Minimum	0.13	51.73	1.78

5.11 Phases Indicated by XrD-Analysis

The XrD-spectras for block T200 and T600 are given in the appendix section 10.13.1. The measured fractions of the different phases after the XrD-experiments are given in the Tables 18 and 19. The volume fraction indicated by the software are wrong due to missing indexing of some intensity peaks i.e. the software calculate all the phases to 100%. The Ti0.862V0.036Al0.102 was indexed as a hexagonal phase, while Ti0.8V0.2 was indexed as a cubic phase. The XrD-analysis will be discussed in further details in section 6.8. As seen from the tables below was the Ti₃Al-phase identified in both blocks, but the volume fractions are wrong.

Table 18: XrD of block T200.

<i>Phase</i>	<i>Volume Fraction (%)</i>
SiC 2H	1.64
Quartz	4.79
Cristobalite	12.49
Ti ₃ Al	17.24
(Al ₃ Ti ₁₇)0.1	55.93
Ti0.862V0.036Al0.102	7.28
Ti0.8V0.2	0.64

Table 19: XrD of block T600

<i>Phase</i>	<i>Volume Fraction (%)</i>
Silicon	9.95
SiC 2H	1.34
Cristobalite	13.19
Ti ₃ Al	40.46
(Al ₃ Ti ₁₇)0.1	0.00
Ti0.862V0.036Al0.102	17.15
Ti0.8V0.2	17.91

5.11.1 Indexing with Ti₃Al-Phase

The same IPF-map as in Figure 56 was attempted indexed with the Ti₃Al-phase. The 30min ion milling sequence should according to theory leave a surface with less mechanical deformation than chemical-mechanical polishing alone. The ion milling should also prepare the phases more uniformly despite their different mechanical properties. This should imply that the conditions were optimized for observing the Ti₃Al-phase by EBSD. The phase distribution map after indexing can be seen in Figure 62 below. The larger fraction Ti₃Al-phase than α -phase implies that something went wrong during indexing. This will be discussed in section 6.8.

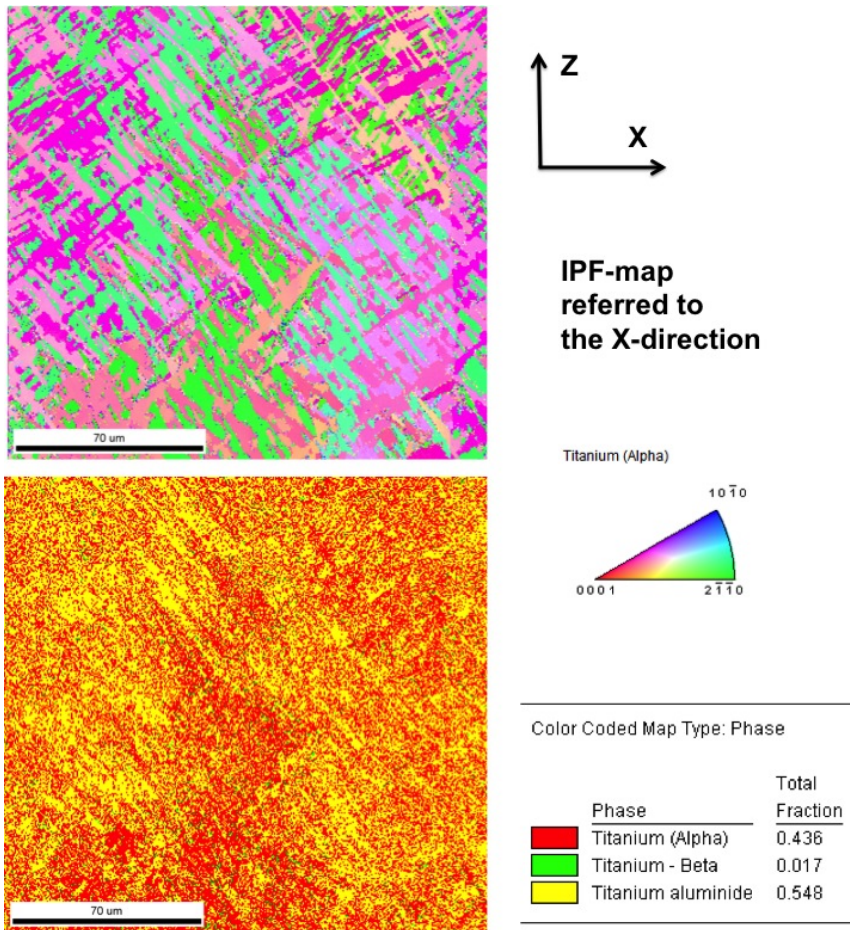


Figure 62: Ion-mill time: 30min. 400X magnification, step size 0.5 μ m, $I_p \sim 83$ nA. Titanium aluminide=Ti₃Al. Specimen from block T200.

5.12 Fracture Surface

One in-situ specimen from block T200 was dedicated for tensile testing only to reveal the fracture mode present in the material. The information provided from a fracture surface can contribute to understand more of the deformation mechanisms present in the material. The specimen failed at approximately 9070MPa. NB! This calculation was based on initial cross section area. The fracture surface can be seen in Figure 63 below. The center part of the fracture surface had a faceted appearance which will be discussed in sections 6.11. The specimen failed at the end of the specimens. See Figure 64 below.

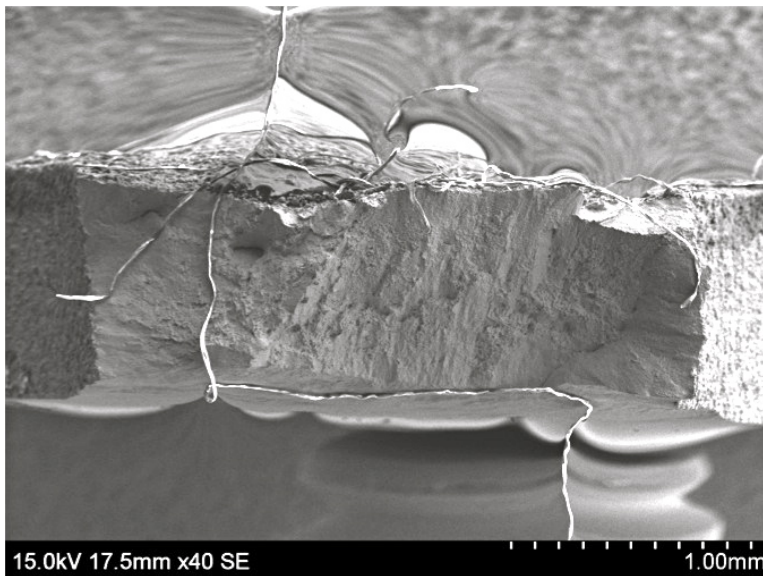


Figure 63: Fracture surface



Figure 64: Specimen T200 after failure

6 Discussion

6.1 Deformation at Macro Level

Comparing SE-images and brightfield images at low magnification of the tensiled in-situ specimens from block T200 and T600, the deformation generally appeared to be more homogeneous in T200. Some of the differences in deformation behaviour at low magnifications, seems to be restricted to prior β -grain boundaries. In T600 was it generally much more visible deformation at prior β -grain boundaries. The T600 specimens was much more severely deformed at 4-5% elongation compared to T200, this deformation seemed to have propagated from β -grain boundaries. However, the etchant effect seemed to have slightly different effect on the samples. This may result from reduction in etchant effect by using the same Kroll-etch several times or because of the microstructure itself was different between the blocks. See for instance Figure 65. S1T600 was reported to may contain a globularized α -phase. This image can support some of these observations. A very coarse and continuous microstructure could be seen near on of the ends of the specimen. This was totally distinct from the other specimens. It is interesting to see how the slip bands are distributed around the area of the center of the specimens and are barely not visible at the center.

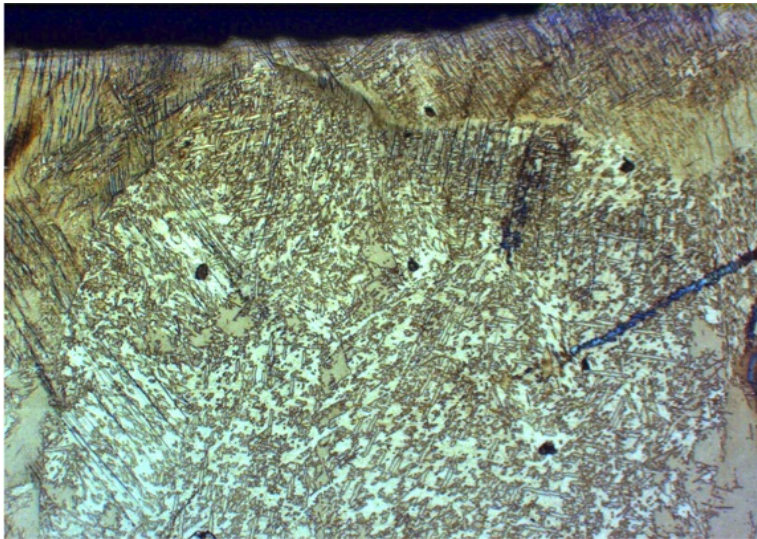


Figure 65: S1T600 was differently etched than the other specimens and may result from the globularized α -phase reported by SINTEF. Magnification 50X. 4% elongation. The scalebar was missing.

Considering the early stage SE-image of S1T600 in Figure 66 below it can be seen that the first visible deformation was also the location for the most severely deformation at the end. From the IPF-map of the same specimen in Figure 46 it also

seems that this early deformation appeared close to a very small β -grain compared to the surrounding grains. The differences in grain sizes may be responsible for the stress concentrated there.

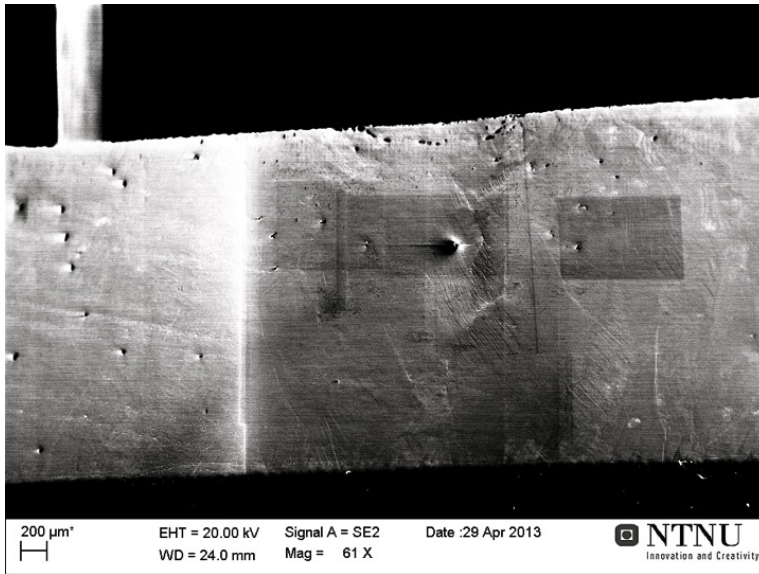


Figure 66: S1T600 after 2.5% elongation

The generally more activity on prior β -grain boundaries may be explained by the differences in cooling rates from the peak temperature. The peak temperature should be approximately the same in both blocks, giving the same β -grains size before cooling. If equilibrium cooling rates are followed will the β -grains size become smaller the closer to the β -transus the temperature gets. The less ordered and in some regions smaller β -grains in in T600 may results from a closer to equilibrium cooling rates. The higher cooling rates in T200 results from the higher position in the block. The higher cooling rates are supported by the narrow β -grains in image 3 Figure 35. It may seem that the heat was more efficiently extracted through the block leading to more efficient epitaxial growth. According to theory the faster cooling rates also implies that less primary α -phase will nucleate and decorate the prior β -grain boundaries. The thicker homogeneous α -phase at prior β -grain boundaries in T600 compared to T200 seems also to play a large role in the overall deformation. This could for instance be seen on S2T600 in Figure 49.

6.1.1 Slip Bands in T200 vs. T600

The larger fraction grain boundary α and maybe globular α -phase expected in T600 in-situ specimens, may also contribute to explain some of the more ductile properties of T600 specimens. These regions are more homogeneous regions of the microstructure compared to lamellar microstructures which can facilitate more long-range dislocation movement. Eventually will visible slip bands be created at the specimen surface after dislocations have moved through the crystal and left the surface. Distinct slipbands at specimen surfaces are generally more easily to observe in homogeneous microstructures because interaction with several slip systems will instead leave a surface with topography. But in contrast may more deformation be observed in homogeneous microstructures before the deformation can be observed as slip bands i.e. the dislocations have to move all the way to the surface. This theory can also be supported by the slightly larger work-hardening properties observed in the T200 compared to T600 in the deposition direction as presented in Table 4. The ratio between UTS and YS for the two blocks were 1,072 and 1.065. The interaction between more slip systems in T200 can for instance be seen in Figure 67 below. The images were taken after a mild Kroll-etch.

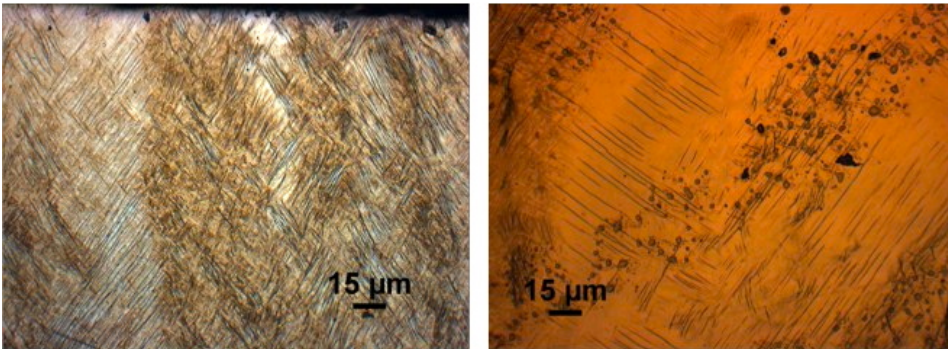


Figure 67: 50X brightfield. Left: S2T200, Right: S2T600. S2T200 appear to have a larger number activated slip systems interacting with one another, leaving a surface with more topography. S2T600 can facilitate distinct parallel slip bands because of homogeneous microstructure. This may result from either from primary α or globular α .

6.2 Deformation at Micro Level

6.2.1 Deformation in globular α -phase

According to section 2.9.2 is globular α -phase a favoured phase for hot-worked fine lamellar structures heat treated at subtransus temperatures. The repeated heating and cooling during deposition introduce internal tensions by phase transformations across β -transus and contraction/expansions by thermal gradients in the material. This may favour globularization in the region with the originally finest lamellar microstructure in the DMD-material. S1T600 was the specimen with the coarsest microstructure in this investigation, beyond comparison. Therefor this specimen was also the most likely to contain a globular α -phase. The globular α -phase may be favoured in T600 because of the longer time at higher temperatures during production. Since this specimen was the most severely deformed of the four specimen is it also tempting to conclude that the coarser microstructure in this specimen must be responsible for some of the deformation. However, when evaluating IPF-maps of S1T600 in Figure 46 is it suprisingly small deformations within coarse regions. The deformation is instead restricted to slipbands in finer parts of the microstructures and at interfaces between differently oriented grains (α -colonies or prior β -grains). But it may seem that the homogeneous regions in S1T600 specimen have absorbed deformation e.g. in the purple area to the right in Figure 47. The IQ-map is very dark in the same region indicating large deformations. If the different ITs of the two blocks can be considered as different holding temperatures in the two phase region will the T600 block generally be located at higher temperatures in the $\alpha+\beta$ -regions of the phase diagram giving larger diffusional rates during the production. This can also contribute to coarsen the already formed globular α -phase and explain why S1T600 have a coarser microstructure.

6.2.2 Critical Resolved Shear Stress in α -Colony

The α -colony structure in Figure 49 survived 5.5% elongation without any visible deformations. The corresponding IQ-map is attached in Figure 68 below. This is relatively bright inside the colony indicating small deformations. Other colonies of the same grain-combination but with a different orientation relative to the tensile direction had much more visible deformation e.g. Figure 45 in the results. The grain combination inside the α -colony is very close to the soft-hard grain combination in both examples. Therefore it may seem that the respective orientation of the α -colony play an important role for the deformation. The soft-hard grain combination tend to fracture instead of slipping because of the very few active slip systems for such orientations. This implies that the Schmid factor is high for all slip systems. The only slip systems which can be active are the shaded prismatic slip systems indicated in the figure below.

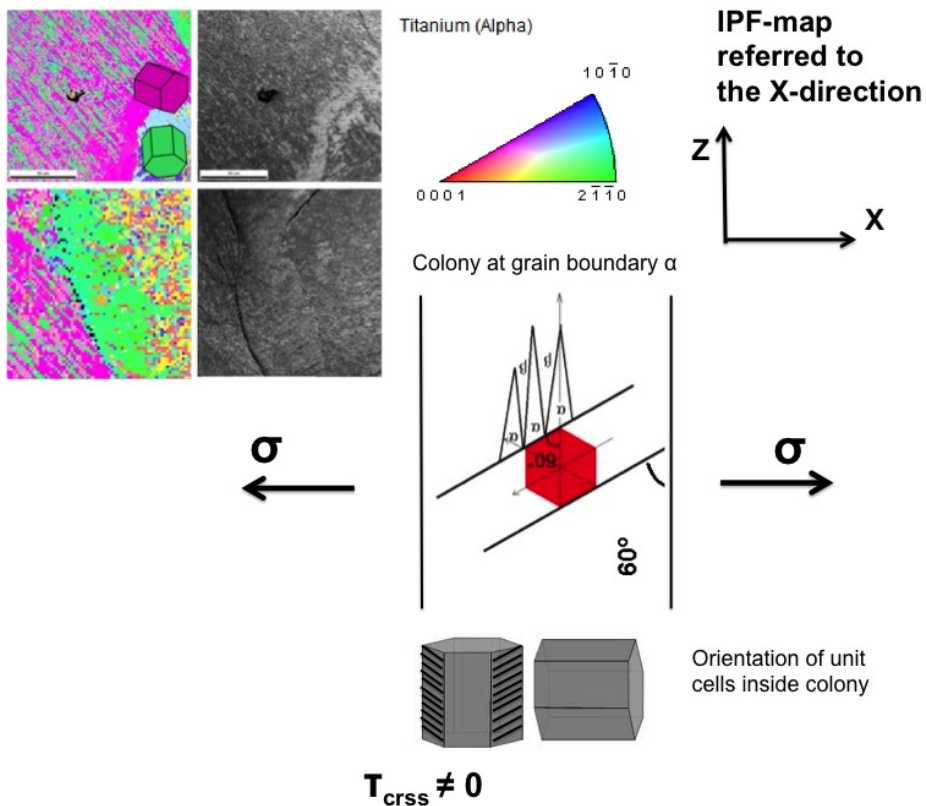


Figure 68: The α -colony structure in the image have a close to hard-soft grain combination, which allows very few slip systems to be active. The only slip systems active for such an orientation is indicated in the figure. The β -phase indicated in the figure have transformed to α -phase in this example.

In this example is cross slip neglected i.e. (a+c)-slip because they have a considerably larger CRSS-value and are less frequently reported to be responsible for the deformation. No shear stress is resolved in the other planes because no shear stress can be resolved in planes parallel and perpendicular to the applied stress σ . Therefore, the deformation along the grain boundary is likely to result from either the prismatic active slip systems or the soft-hard grain combination.

Figure 69 illustrate an example for the calculated Schmid factor for the active slip systems in the α -colony structure of Figure 68. Only two of three prismatic slip systems can be activated for the given load direction. However, the corresponding slip systems across the mirror plane can also be activated. The Schmid factor of 0.433 is relatively close to the maximum value of 0.5. See Figure 18 for comparison with other orientations of the prismatic planes relative to the tensile axis. From Schmid's law presented in equation 13 in the appendix this implies a large CRSS-value is needed to activate these slip systems for this orientation. However, there are also relatively few active slip systems for this orientation. This mean that the few active slip systems must accomodate more energy in a smaller volume of the material. This may also contribute to understand why colony-structures are some of the most important microstructural constituents for this alloy.

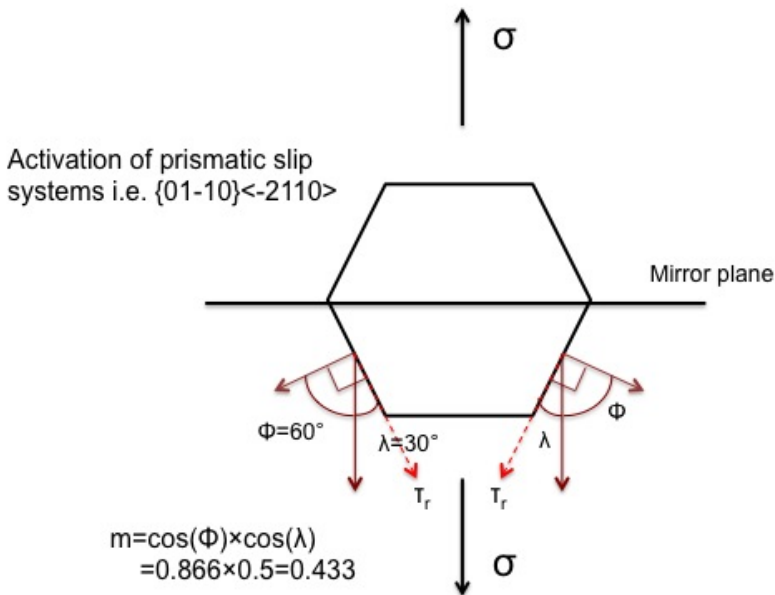


Figure 69: Applying Schmid's law for α -colony. Illustration: Lars Eriksen

6.2.3 Dominating Slip Systems Indicated by Taylor Factor Maps

A function in OIM Analysis 6.0 can map Taylor factor for desired slip systems. The procedure to create the maps was presented in section 10.12 in the appendix. This procedure was used on the EBSD-scan presented in Figure 43 in the result part. The Taylor maps for the both basal and prismatic slip systems for uniaxial tension conditions are given in Figure 70 below. NB! there are some uncertainties of the default reference direction for the uniaxial stress conditions selected in OIM Analysis 6.0. i.e. which of the three coordinate axis the uniaxial tension corresponds with. However, in these maps are the brightest areas the most susceptible to accommodate slips for the given grain orientations. The Taylor maps were generally brighter for the basal slip system for this EBSD-scan, indicating that basal slip are most likely to be responsible for the initiation of the cracks at the center of the image. However, only one the three possible prismatic planes were selected for this comparison. The cracks in the image are generally located between bright and dark regions. This may result from the the different orientations of the grains which again accomodate the deformation very differently, leading to different deformation behaviours. The highest Taylor factor indicated in the tables to the right also support that the basal slip was the most dominating i.e. Taylor factor is the inverse of the Schmid factor also presented in section 10.1 in the appendix.

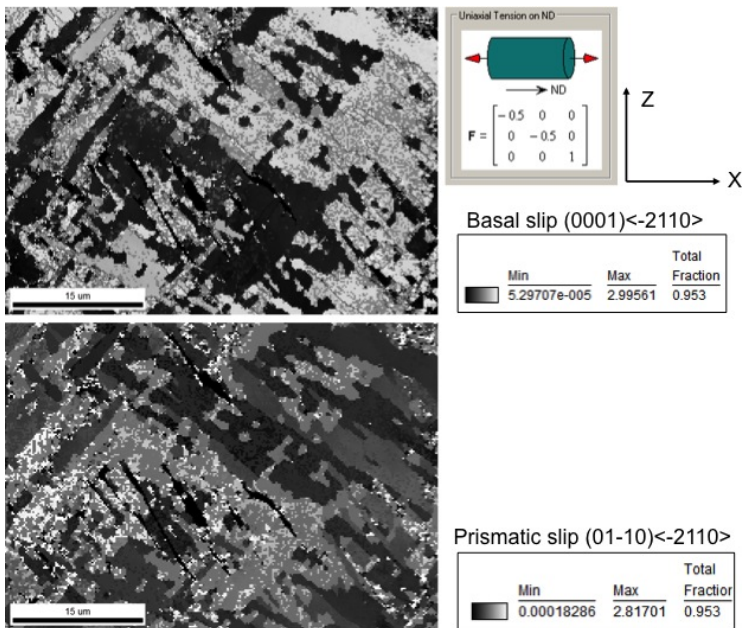


Figure 70: The Taylor factor map above was used to analyse susceptible grain orientations for accommodating slip in S1T200. Brighter areas are generally more susceptible for slip. The matrix in the figure indicates the stress distribution. This can be modified to apply to deformations such as extrusion and rolling.

The cracks in the figure were located in a similar position of the microstructure as in the left image of Figure 67. Seemingly have the cracks been effectively stopped at the crack tip by a plate with distinct orientation. The effective stopping of a crack may also be seen by the frequently alternating directions of the slipbands in Figure 67, and explain why T200 had a more uniform deformation because of the shorter effective slip lengths.

6.3 Tensile Curves

The tensile curve of S1T600 in Figure 50 yielded an UTS of 807MPa. The higher UTS of T600 compared to T200 was in contrast to measurements performed by SINTEF. They obtained 985MPa for block T200 and 978MPa for T600 in the deposition direction. However, the higher position of T200 in the block and the additional deposits in the volume of T200-specimens does not give comparable conditions.

The tensile curves obtained have 3-4 times lower E-modulus than the 110GPa reported for the material in the litterature. This was explained in previous work [6] in ch. 5.3.3. The tensile stage was termed a "soft" machine, not giving reliable or replicable stress-strain curves.

The specimens were fastened to different forces at the tensile stage before the tensile experiments could start. This mean that in-situ experiments were started at different unknown forces and did not have origo in the same values. This may for instance lead to yielding of one specimen seemingly at an early stage. The dipping of the curves can be explained by mainly two contributions: relaxation of the specimen and the tensile stage after start and stop of the experiments. The electrical motor also consists of a set of several gears of different sizes. It is not likely that the grooves are completely tight leading "creeping". A weakness with the tensile stage is the strain-measurements are not performed by a dilatometer but by counting the turns of the motor.

6.4 Identification of Burgers Orientation Relationship at Prior β -Grain Boundaries

By using a highlight function in the OIM Analysis 6.0 software can desired grain orientation be highlighted with a color in ordinary IQ-maps. This was performed on the same grain boundaries as in Figure 55 for a tolerance angle of 2 degrees. From this the BOR in the top image become more apparent to be related to the right prior β -grain.

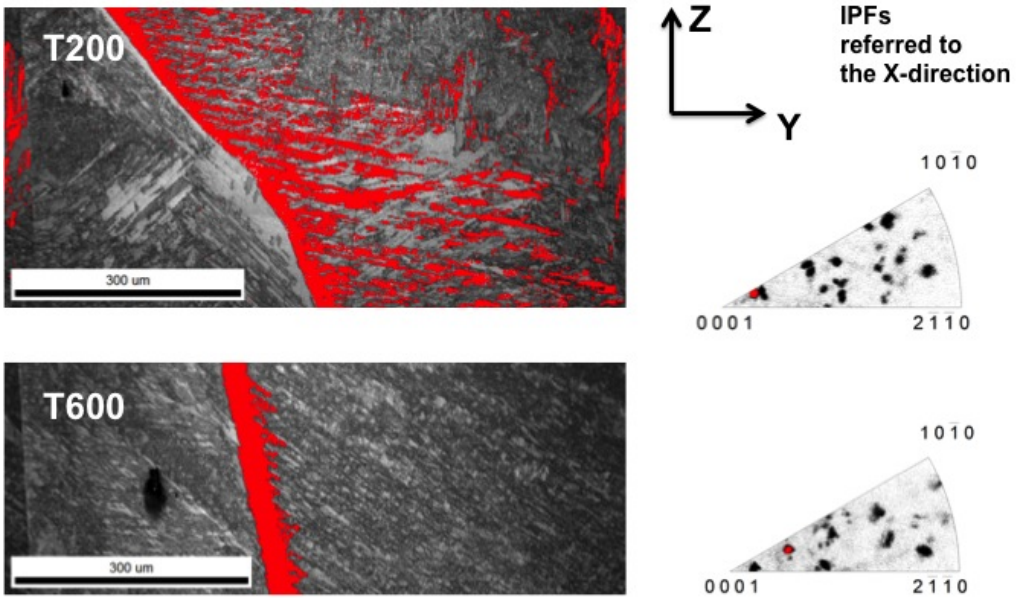


Figure 71: The colonies along the prior β -grains have BOR with the right grain. The corresponding IPFs are given to the right in the image.

Preferential Grain Orientations

Along prior β -grain boundaries can linearization of prismatic planes frequently be observed i.e. the prismatic planes are almost exclusively following the curvature of the β -grain boundary. This is a consequence of BOR.

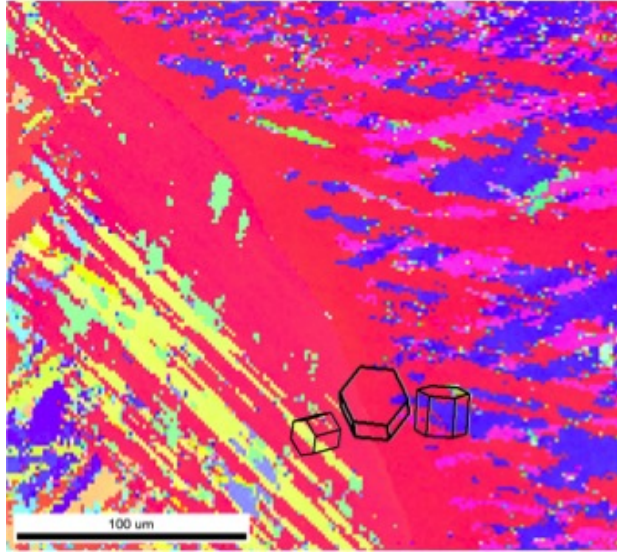


Figure 72: HCP-unit cells seems to have their prismatic planes in proximity to the grain boundary. The unit cells indicates the red, yellow and blue grain orientation. Scalebar=100 μ m.

6.5 Texture in Columnar β -Grains

Pole figures were added to the IPF-images in Figure 54 to evaluate the texture in the interface region between the substrate plate and the block. A gradually transformation from a highly random grain distribution in the plate to a more ordered structure in the columnar β -grains in the block could be observed. This can be seen from the more "clustering" of points in the polfigure image 1. Supprisingly was the texture in the bimodal plate very low. The rolling should traditionally introduce texture by orienting the HCP-grains. It could be seen from the IPF-map in 4 that several grains have the basalplane with its c -axis oriented out of the image, but the effect of them are very low on the corresponding pole figure. However, this may indicate that the plate had recrystallised between each rolling sequence leading to a more random distribution. The basketweave microstructure which is generally observed in the center of the block has not yet fully developed in the image 1. An introduction to how to read pole figures was attached in section 10.20 in the appendix.

The highlighting function in OIM Analysis 6.0 was used to evaluate the texture in the first columnar grains growing from the equiaxed microstructure in Figure 54. The majority of the grains have an orientation between the prismatic and basal orientation. See IPF to the right in Figure 73 below. However, the basal orientation was most favoured in plates growing from the β -grain boundary, while prismatic orientation can be observed in the interior of the grain. They were given red and green colors, respectively.

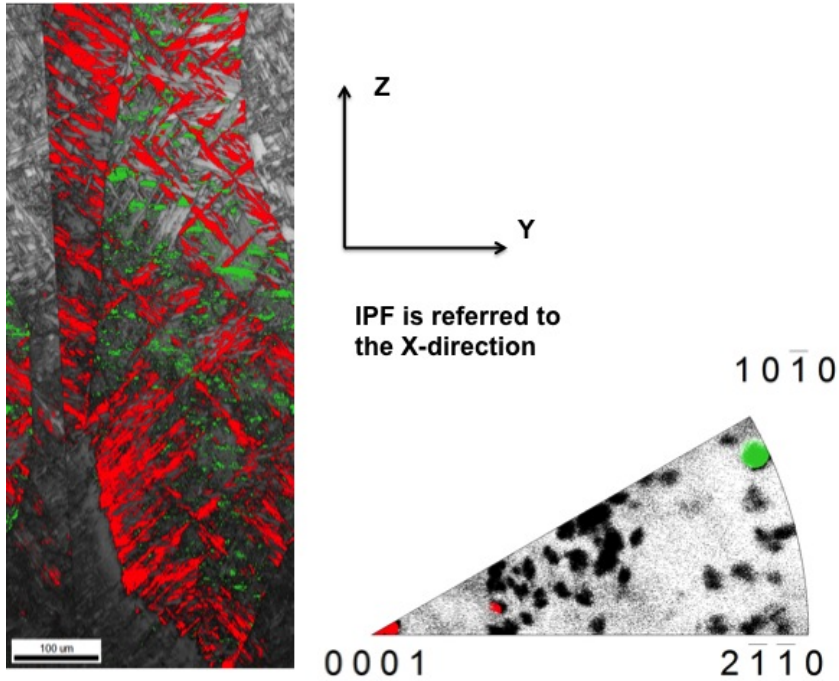


Figure 73: The highlight function in OIM Analysis 6.0 was used to evaluate texture-components in the columnar grain above. The artifact to the left in the image was reported in section 5.6.

According to theory can lamellar α -phase nucleate directly from the β -grain boundaries for high cooling rates. The cooling rates in the first deposited layers are very high because of the relatively large substrate plate compared to the weld bead. The substrate act as a heat sink giving fast cooling rates. The high cooling rates close to the substrate plate can be verified by the narrow and very oriented columnar grain. The fast cooling rates is supported by the small amounts of primary α -phase in Figure 73. Compared to block T200 in Figure 71, are also the plates considerably shorter. $300\mu\text{m}$ compared to approximately $100\mu\text{m}$.

6.6 Contributions from Hydrocarbon Deposition on Quality Parameters of the EBSD-maps

The EBSD+in-situ tensile tests were performed for a minimum of four scans of the same region of the microstructure during this work. It is difficult to evaluate if the hydrocarbon deposition have contributed to lower the quality parameters of the EBSD-maps additionally to the contribution from the deformation. From section 10.13 in the appendix it can be seen that all the quality parameters drops as a function of deformation. To evaluate the influence of hydrocarbons a comparison between the SEM-settings used in this work with the settings reported after Y. Chen et. al. [45] should be made. See Table 20 below for this comparison:

Table 20: Comparison of SEM-settings for Y. Chen et. al. experiments and in this work. The higher probe current, lower system vaccum and lower frame rate give increased hydrocarbon deposition compared to Y. Chen et. al.

<i>SEM-settings</i>	<i>Y. Chen et. al.</i>	<i>This work</i>
Probe current (nA)	33	37
Vacuum (Torr)	$4.5 \cdot 10^{-7}$	$2 \cdot 10^{-6}$
Frame rates per seconds (fps)	140	100-150

The lower frame rates (for worst case scenario) used in this work implies also a longer exposure time. Therefor, the hydrocarbon deposition during the in-situ experiments may play a minor role for the overall degradation of the quality parameters in addition to deformation. To evaluate the true effect of hydrocarbon deposition should repeated scans be performed on an undeformed material.

6.7 Calculation of Spatial Resolution

When comparing the calculated values for the spatial resolution in section 5.9 with the graph for spatial resolution in Figure 78 in the appendix, the calculated spatial resolution is generally larger. Minimum a factor of 1.5 larger. However, to do calculation of spatial resolution should several grain boundaries be selected to achieve a more accurate comparison. Another contributing factor for the differences, may be the weak tilting of the grain boundary giving different resolution across the cropped region. A rule of thumb is that the spatial resolution is a factor of 3 higher in the vertical direction compared to the horizontal direction. The method used here to calculate the spatial resolution was also slightly different. The wrongly indexed points were counted directly from the cropped images and from both side of the grain boundaries in Figure 61. This was in contrast to Y. Chen et. al which used the software to indicate the number of bad points with a $CI < 0.08$.

However, when performing cleanup of the three probe current conditions with a CI -correlation of < 0.08 was more bad points changed from the 50nA probe current conditions compared to 80nA. This may indicate that lower probe current are the favoured selection for the following reason: The improved spatial resolution at grain boundaries makes it easier for the OIM Indexing software to separate bad points from good points, and therefor was more points removed from 50nA. This is supported by the theory that larger probe currents give a higher probability for having overlaying patterns.

6.8 XrD-Analysis and Indexing of Ti_3Al -Phase

The Ti_3Al -phase may be present in the material, as indicated by the indexed peaks of the XrD-spectras. However, the volume fractions must be wrong. According to the Ti-Al phase diagram, does the material only "touch" the two-phase region between $\alpha + Ti_3Al$ during the solidification path of the material. The mix-up between the HCP phase and the Ti_3Al -phase during indexing may be caused by the similar lattice parameters. Another explanation may be that the sample preparation is insufficient to separate the phases because of different mechanical properties. The XrD-spectras of the blocks in section 10.13.1 in the appendix also indicated relatively large amounts of cristobalite for both blocks. This may result from the silica substant added to the OPS-suspension. The sharp peaks in the patterns are most likely the α -phase. They show quite pronounced preferred orientation, which indicates that the grains in the sample are not randomly oriented. The broad peaks are a different phase where the database did not contain a match. The broadness of the peaks indicates that there is a "problem" with the phase. This might be microstrain or extremely small crystallites. Note that the database used is not updated for all and intermetallic and metallic phases. Reference: From E-mail Julian R Tolchard, Senior Engineer NTNU.

6.9 Effect of Deformation on Quality Parameters of the EBSD-map

EBSD is a technique which rely upon an undeformed material in the uppermost 50nm of the sample surface. This is where the EBSPs are emitted, and small deformations in the lattice can lead to more scattering of the BSEs and weaker Kikuchi-bands. Deformation or tensions was introduced to the investigated material by three mechanisms: during solidification, sample preparation or during in-situ tensile tests. Their contributions on the quality parameters will be discussed below:

Sample Preparation

The chemical-mechanical polishing was often used as a stand-alone sample preparation during the experimental part of this work. This sample preparation relies upon removal of the most deformed top layer by finer and finer grids, in addition to oxidize the surface additionally by building up the oxidized layer. However, because of the different chemical and mechanical properties of the different microstructure constituents and their crystal orientations will this sample preparation be highly dependent on positions. For example as illustrated below in Figure 74 do the IQ-map have different grey tones after the qualities of the EBSPs. The bright regions are generally the best, having the less deformed lattice. The IQ-value is for instance 195 inside the red needle in the image, while the surrounding blue orientation have only a IQ-value of 147. The oxidation suspension used may also attack some microstructures more frequently than others.

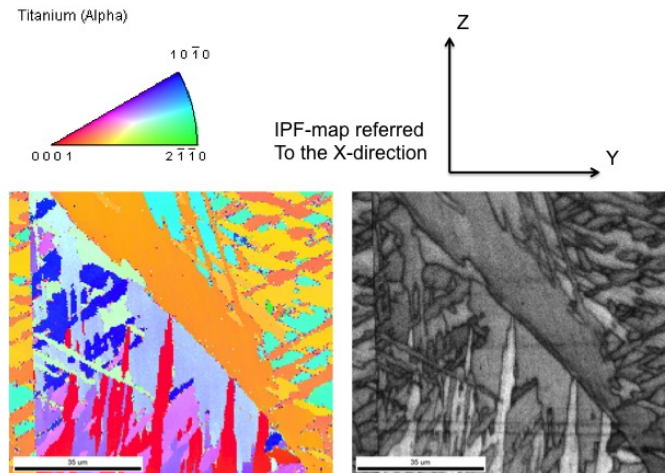


Figure 74: The different microstructural constituents can responding differently on the chemical-mechanical polishing used. Scalebar= $35\mu\text{m}$.

Solidification

When comparing the Quality Parameters of the EBSD-map of the interface region between the substrate plate and the block with the tensiled in-situ specimens in section 10.13, the quality on the parameters drops more rapidly for the interface region. This may indicate that the DMD-material deforms relatively locally after the in-situ experiment. Assuming that the cooling rate is faster closer to the substrate plate, the generally lower parameters close to the substrate plate compared to the solidification of columnar prior β -grains can tell us that there may be more internal tensions between the plates growing close to the substrate plate. However, the different quality parameters seems to drop relatively uniformly.

Lamellar microstructures are often favoured growth mechanisms for materials having high internal stresses. The lamellar shape can reduce the interface stresses between the β - and α -phases. A consequence of this growth mechanisms is that lamellar microstructures also contains a large grain boundary area. Grain boundaries are generally regions with high dislocation densities. Thermal stresses and volume changes by phase transformations are also mechanism which can give a generally more deformed crystal structure. Because of this the DMD-material is a challenging material to investigate with the EBSD-technique. The relatively low overall EBSD-map qualities are therefor expected compared to recrystallized and homogeneous materials.

The best quality parameters was obtained for a relatively coarse basketweave region of the microstructure at the center of the block. This EBSD-scan was not included in this report, but can be found in Figure 25 in previous work [47]. However, the high quality obtained for this scan supports the theory that cooling rates and internal tensions influence the overall quality parameters of the EBSD-map. Since the coarsest basketweave microstructure is where the cooling rates are lowest at the intersection of β -transus.

6.10 Fraction β -Phase

The fraction retained β -phase obtained in this work is highly uncertain. Singular pixels indexed as β -phase are generally not a good indication for the phase. The indexed β -phase was mainly located at grain boundaries. It may seem that the phase are favoured in region with highly deformed patterns along grain boundaries. The amount of β -phase dropped sharply after cleanup, from 9% to only approximately 0.2%. Short enough step size is believed to be the key to reveal this phase in larger amounts. If the grain boundaries containing the β -phase are assumed to be approximately $1\mu\text{m}$ will only 20 pixels origins from the grain boundary for a step size of $0.05\mu\text{m}$. When considering that electron beam also have a diameter the points inside the β -phase at the grain boundary will be reduced. Therefor it may seem

that the step size applied in this work may be still too large to have enough pixels inside the grain boundary and to avoid many overlapping patterns at the grain boundary.

6.11 Fracture Surface

The crack surfaces of T200 contain mainly a combination of facets and dimples. This may indicate that there are two different crack-nucleation and growth processes involved. The dimpled part of the fracture surface may be located in regions of the microstructure containing lamellas where a transgranular fracture has taken place. The faceted surface seems to be less ductile and may be a result of cracks growing along prior β -grain boundaries decorated with homogeneous primary α -phase. The crack process in these regions has more intergranular characteristics. This is in correspondence with analysis of Charpy notched fracture surfaces after electron beam welded Ti6Al4V performed by [51]. From this work it was also reported the same faceted-like appearance in regions containing prior β -grains.

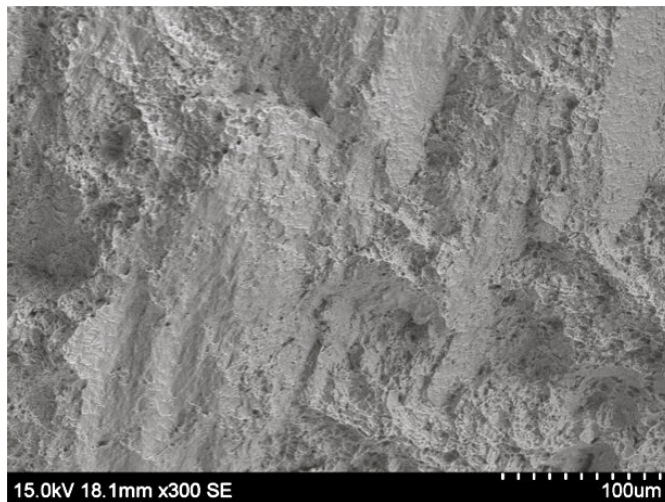


Figure 75: Fracture surface of in-situ specimen from block T200.

The region to the left in the fracture surface of Figure 63, had a slightly different appearance than the region to the right. A close up image of this region is given below. From the location of the fracture at the in-situ specimen in the lower part of Figure 76, it is believed that this can be explained by the thinner deposited layer in the same location. The thinnest part of the deposit is indicated with arrows. The coarseness of the lamellar structure at different position inside a deposited layer was discussed in Figure 13, and the finest lamellar microstructure was reported to be located at the interface between two deposits. Because this is where the cooling rates are expected to be the highest. Finer lamellas also means higher YS from Figure 19, and a shorter effective slip length. This may contribute to explain the less dimpled surface at 300X in Figure 76.

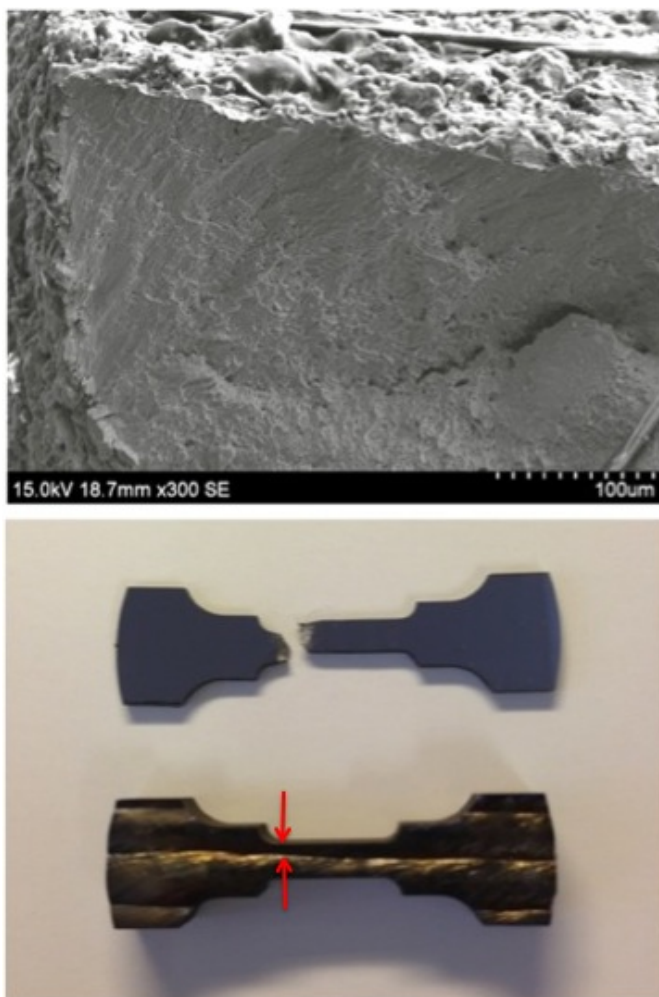


Figure 76: Fracture surface of in-situ specimen from block T200 and position of failure.

7 Conclusion

- Very small differences in the solidification structures grain size and morphology were found between the blocks for specimens extracted from the center of the blocks. This corresponds to the similar cooling rates of the blocks from the same peak temperature across β -transus.
- A consequence of the statements above was also similar thickness of the primary α -phase along prior β -grains observed between the blocks.
- The higher position of T200 in-situ specimens in the block did not give comparable conditions to T600 in-situ specimens. The T200 specimens also contained two deposits in contrast to only one in T600. These conditions made investigations of the ITs influence on ductility difficult.
- Prior β -grain boundaries were observed to play an important role for initiation of the plastical deformation.
- Thinner, longer, and more ordered columnar β -grains were observed in T200 in-situ specimens because of faster heat extraction closer to the top of the block. The faster cooling rates was further expected to give less primary α -phase on prior β -grain boundaries, and finer lamellar microstructure. The combinations of these parameters gave a more homogeneous deformation of T200 in-situ specimens.
- More visible slipbands on T600 in-situ specimens support the presence of more homogeneous phases such as primary α -phase and globular α -phase. Dislocations can more easily move through the material in such region and create slipbands. Correspondingly was more topography observed in T200 specimens due to interactions with several slip systems in the lamellar microstructure.
- The frequently reported mismatch between soft and hard HCP-grains were observed.
- The average quality parameters of the EBSD-maps for the DMD-alloy is still very low after ion milling as a subsequent sample preparation to chemical-mechanical preparation. An averagely CI of 0.316 were obtained for 30 different EBSD-scans. The maximum CI was 0.56. The highest CI-value for retained β -phase was only 0.114 after ion milling and cleanup function in OIM Analysis 6.0. This phase is not likely to exist in large amounts in the material. And its seemingly located in the most deformation-rich locations of the lamellar microstructure.
- Attempts to index the Ti_3Al -phase were not successful.
- The basketweave microstructure develops at relatively short distances from the substrate plate.

8 Further Work

For more accurate comparison of the influence of IT on mechanical properties should the in-situ specimens be extracted from the same position in the blocks, i.e. both in z-direction and the relative position inside a deposition layer. It can also be valuable to mark both the deposition direction and the position in the y-direction on each in-situ specimen. This allows combining information between adjacent specimens which may contain some of the same β -grains.

The Taylor map function in the OIM Analysis 6.0 software should be applied to the material in larger extent than in this work to evaluate the different deformation mechanisms present in the material. In this work it was only applied to a lamellar microstructure for one basal and one prismatic slip system. This map is believed to be one of the best tools to evaluate the deformation mechanisms over a larger area of the microstructure. Schmid factor calculations to evaluate active slip systems are not considered particularly informative in the complex lamellar DMD-material.

A weakness with the combined EBSD+in-situ technique was the small area which could be observed with the technique for the respective material. To observe the deformation mechanisms in the very fine grained regions of the material was a small step size selected. This led to increase in scan times and that only very small ROIs was selected. For the working distance of 24mm could only approximately half of the specimen be observed from the SE-image at the lowest magnification of 61X. See for instance Figure 66. This implies that some of the deformation events were lost during the in-situ experiments because they were outside the screen or ROI. Based on these experiences it can be valuable to perform some complementary studies to evaluate the chronology of events. This can for instance be performed the following way: A set-up with film camera, oblique illumination, the tensile stage in Figure 29 on a table, and a camera tripod can be used to take images for instance every second during very slow monotonic tension. The complete tensile specimen can then be imaged very accurately uncovering the weakest locations and the first deformation on the in-situ specimen. The specimen can further be investigated at this particular location by EBSD.

9 References

- [1] Fatigue and Durability of Structural Materials, Gary R. Halford, S.S Manson. The Materials Information Society, 2006.
- [2] Lütjering, G. and J.C. Williams, Titanium. 2007, Berlin, Heidelberg: Springer-Verlag.
- [3] Titanium, a technical guide, second edition, Matthew J. Donachie, Jr. ISBN: 0-87170-686-5. Desember 2000. ASM International.
- [4] Article Teknisk Ukeblad (technical magazine), edition 1, year 2013. Page 34. Den Industrielle revolusjon 2.0.
- [5] Matthew J. Donachie Jr., Titanium: a technical guide, 2000.
- [6] In-Situ Tensile Testing Combined with EBSD Analysis of Ti-6Al-4V Samples from Components Fabricated by Additive Layer Manufacture, Martin Borlaug Mathisen, 15 Jun 2012.
- [7] C. Leyens and M. Peters, Titanium and Titanium Alloys: Fundamentals and Applications, WILEY-VCH Verlag GmbH & Co., 2003.
- [8] F.J. Gil, M.P. Ginebra, J.M. Manero, J.A. Planell, Formation of α -Widmannstätten structure: effects of grain size and cooling rate on the Widmannstätten morphologies and on the mechanical properties in Ti-6Al-4V alloy. Journal of Alloys and Compounds, 2001. 329(1-2): p. 142-152. DOI: 10.1016/S0925-8388(01)01571-7
- [9] J.C. Williams, A.W. Sommer, and P.P. tung: Metall. Trans., 1972, vol. 3, pp. 2079-984; Metall. Trans., 1973, vol. 4, p. 1188
- [10] Banerjee, S. and P. Mukhopadhyay, Phase transformations: examples from titanium and zirconium alloys. 2007, Amsterdam: Elsevier. xxii, 813s.
- [11] Materials Properties Handbook: Titanium Alloys, ASM International, 1994.
- [12] Vanadium-producers homepage: <http://vanitec.org/home-2/titanium/>
- [13] Investigations of the benefits of plasma deposition for the additive layer manufacturing of Ti-6Al-4V. F. Martina, J. Mehnen, S.W. Williams, P. Colegrove, F. Wang. Journal of Materials Processing Technology, Volume 12, Issue 6, June 2012, Pages 1377-1386.
- [14] Additive manufacturing of Ti-6Al-4V components by shaped metal deposition: Microstructure and mechanical properties. Bernd Baufeld, Omer Van der Biest, Rosemary gault. 16 November 2009.
- [15] Characterisation of Metal Deposition during Additive Manufacturing of Ti6Al4V by Arc-wire Methods. N.P. Hoyer, E. C. Appel, D. Cuiuri and H. Li. School of Mechanical, Materials and Mechatronic Engineering, University of Wollongong NSW, Australia 2518.

- [16] Kurz, W. and D.J. Fisher, Fundamentals of solidification. 1998, Uetikon-Zuerich: Trans Tech Publications. 305s.
- [17] Compendium is the course TMM4165 Joining Technology, teacher Odd Magne Akselses, SINTEF.
- [18] Fatigue Data Book: Light Structural Alloys, ASM International
- [19] Microstructure and Phase Transformation of Ti-6Al-4V, Robert Pederson, Department of Applied Physics and Mechanical Engineering. Division of Engineering Materials, Luleå University of technology. 2002:30 ISSN: 1402.1757
- [20] T. Furuhashi, S. Takagi, H. Watanabe et. al., Metall, Mater, Trans, A 27 1635(1996)
- [21] T. Furuhashi, J.M. Howe and H.I. Aaronson, Acta Metall. Mater. 39 2873 (1991).
- [22] D. Rugg, M Dixon and F. P. E Dunne, Effective structural unit size in titanium alloys, The journal of strain Analysis for Engineering Design 2007 42: 269.
- [23] Ivasishin, O.M. and R.V. Telioich, Potential of rapid heat treatment of titanium alloys and steels. Materials Science and Engineering: A, 1999. 263(2): p. 142-154.
- [24] E. Lee, R. Banerjee, S. Kar, D. Bhattacharyya & H. L Fraser (2007): Selection of α variants during microstructural evolution in α/β titanium alloys, Philosophical Magazine, 87:24, 3615-3627. DOI: 10.1080/14786430701373672
- [25] Ahmed, T. and H.J. Rack, Phase transformation during cooling in $\alpha + \beta$ titanium alloys. Materials Science and Engineering A, 1998. 243(1-2): p. 206-211
- [26] Mechanical Metallurgy, George E. Dieter.
- [27] A systematic study of hcp crystal orientation and morphology effects in polycrystal deformation and fatigue. F.P.E. Dunne, A. Walker and D. Rugg. Department of Engineering Science, Oxford University. Available Online: DOI: 10.1098/rspa.2007.1833.
- [28] Betsofen, S.Y., et al., Texture and anisotropy in the mechanical properties of titanium caused by the mechanism of plastic deformation. Russian Metallurgy (Metally), 2007. 2007(5): p. 387-393.
- [29] Rösler, J.; M. Baker, and H. Harder, Mechanical Behaviour of Engineering Materials: Metals, ceramic, Polymers, and Composites. 2007, Berlin, Heidelberg: Springer-Verlag Berlin Heidelberg.
- [30] Analysis of the different slip systems activated by tension in a α/β titanium alloy in relation with local crystallographic orientation. F. Bridier, P. Villechaise, J. Mendez. 2004

- [31] Deformation Twinning: Mechanisms and Their Role in Crystal Plasticity Models. Su Leen Wong. May 8, 2006.
- [32] The crystallography and deformation modes of hexagonal close-packed metals. P.G. Partridge.
- [33] Experimental study of dislocation mobility in a Ti-6Al-4V alloy. P. Castany, F. Pettinary-Sturmel, J. Crestou, J. Douin, A. Coujou. doi:10.1016/j.actamat.2007,07.032.
- [34] High deposition rate high quality metal additive manufacture using wire + arc technology, available at: www.norsktitanium.no. Authors: Dr. Paul Colegrove and Professor Stewart Williams.
- [35] Effect of welding on impact toughness of butt-joints in a titanium alloy, Wei Zhou, K.G. Chew. November 1999. Materials Science and Engineering A347 (2003), Page 180-185
- [36] J.L Barreda, F. Santamaria, X. Azpiroz, A.M. Irisarri, J.M. Varona, Vacuum 62 (2001) 143-150.
- [37] Effect of Initial Structure on Globularization of Hot Multi-Forged ELI Grade Ti6Al4V. Jin Young Kim, In Ok Shim, Soon Hyung Hong. Technology R&D Center, Agency for Defense Development, Yusong P.O. box 35-5. Daejeon 305-600, Korea. Materials Science Forum Vols. 558-559 (2007) pp 529-532 online at <http://www.scientific.net>.
- [38] The influence of microstructural characteristics on the mechanical properties of Ti6Al4V-alloy produced by the powder metallurgy technique. Dusan Bozic, Ivana Cvijovic, Mirosljub Viltotijevic, Milan T. Jovanovic. Institute of Nuclear Sciences, Belgrade, Serbia. doi: 10.2298/JSC0609985B
- [39] Deformation Modes of the α -Phase of Ti-6Al-4V as a Function of Oxygen Concentration and Aging Temperature. Gerhard Welsh and Wolfgang Bunk.
- [40] G.Welsch, G. Lütjering, K. Gazioglu, and W. Bunk: Metall. Trans. A 1977, vol. 8A, pp- 169-77.
- [41] J.N. pratt, W.J. Bratina, and B. Chalmers: Acta Metall., 1954, vol. 2, pp. 203-08.
- [42] A. Clauss, F. Ashtrafi, and B. Heulin: C.R. Acad. Sc. Paris, 1974, t. 278, pp. 909-12.
- [43] Teaching material in the course TMT4505, Jarle Hjelen. Electron BackScatter Diffraction EBSD in SEM, Institutt for materialteknologi.
- [44] Transmission EBSD from 10nm domains in a scanning electron microscope. Journal of Microscopy. R.R. Keller, R.H. Geiss. published online 17now 2011. DOI: 10.1111/j.1365-2818.2011.03566.x

- [45] Y. Chen, J. Hjelen, S.S. Gireesh & H.J. Roven, Optimization of EBSD parameters for ultra-fast characterization, Norwegian University of Science and Technology NTNU, Department of Materials Science and Engineering, Trondheim, Norway. doi: 10.1111/j.1365-2818.2011.03551
- [46] Use of the Hough Transformation To Detect Lines and Curves in Pictures. Richard O. Duda and Peter E. Hart Stanford Research Institute, Menlog Park, California. November 1970.
- [47] Eriksen L., EBSD-Investigation of DMD Ti-6Al-4V, Characterisation of microstructure, in Department of Materials Science. Fall 2012, NTNU: Trondheim
- [48] Electron Backscatter Diffraction (EBSD) Technique and Materials Characterization Examples. Tim Maitland and Scott Sitzman.
- [49] Bill Taylor (Struers Ltd, G., Elisabeth Weidmann (Struers A/S, Copenhagen) Application Note: Metallographic preparation of titanium 2008.
- [50] Pearson, W. B. A Handbook of Lattice Spacing and Structures of Metals and Alloys, , Pergamon Press,: Oxford, UK, 1964; p. 106.
- [51] Fracture toughness of electron beam welded Ti6Al4V. K. Prasad Raoa, K. Angamuthub, P. Bala Srinivasan. Department of Metallurgical and Materials Engineering, Indian Institue of Technology (Madras), Chennai 600036, India Adama University, Nazareth, Ethiopia. Journal of materials processing technology 199 (2008) 185-192. 2007.
- [52] Fabrication of Ti-6Al-4V Scaffolds by Direct Metal Deposition, G.P. Dinda, L. Song, and J.Mazumder. The Minerals, Metals and Materials Society and ASM International 2008, September 2008, DOI; 10.1007/211661-008-9634-y, volume 39A, s2914-2922.
- [53] The role of bimodal and lamellar microstructures of Ti6Al4V on the behaviour of fatigue cracks emanating from edge-notches. M. Bendetti, V. Fintanari. Department of Materials Engineering and Industrial Technologies, University of Trento Via Mesiano 77, 38050 Trento, Italy.
- [54] Medical Device Materials. Proceedeings of the Materials & Processes for Medical Devices Conference. Sanjay Shrivastava. 2003. ISBN: 0-87170-798-5 SAN: 204-7586.
- [55] Inleunce of microstructure on High-Cycle Fatigue of Ti6Al4V: Bimodal vs. lamellar Structure. R.K. Nalla. B.L, Boyce, J.P. Campbell, J.O. Peters, and R.O. Ritchie.

10 Appendices

10.1 Critical Resolved Shear Stress for single crystals

The theory behind the CRSS-value can best be illustrated by an example for a single crystal. The cylindrical single crystal in Figure 77 have a cross-section area A_0 . The angle between the normal to the slip plane A and the vertical tensile axis is ϕ , and the angle which the slip direction makes with the tensile axis is λ . The area of the slip plane inclined at the angle ϕ will then be $A=A_0/\cos \phi$, and the component of the axial load acting in the slip plane in the slip direction is $F_r=F \cdot \cos \lambda$.

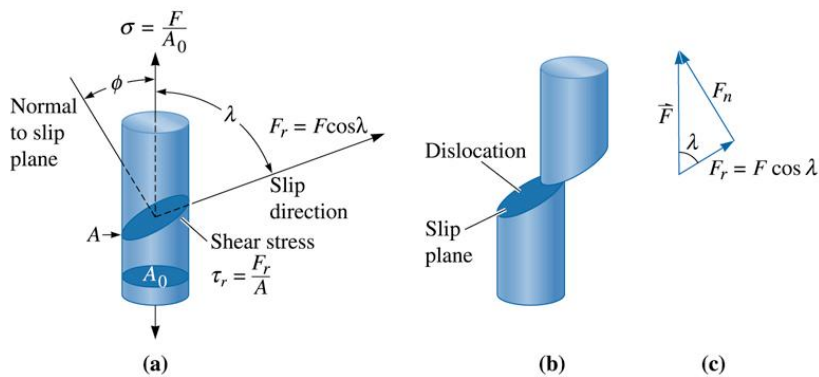


Figure 77: Illustration of CRSS for single crystal.

Insertion of F and A into the formula 13 for shear stress stress i.e. $\tau_r = F_r/A$ gives the following relationship for CRSS or τ_r :

$$\tau_r = \frac{F \cdot \cos \lambda}{\frac{A_0}{\cos \phi}} = \frac{F_r \cos \phi \cos \lambda}{A_0} \quad (13)$$

This relationship is called Schmid's law, where the product $m = \cos \phi \cos \lambda$ is frequently referred to as the Schmid factor.

10.2 Spatial Resolution vs. Probe Current

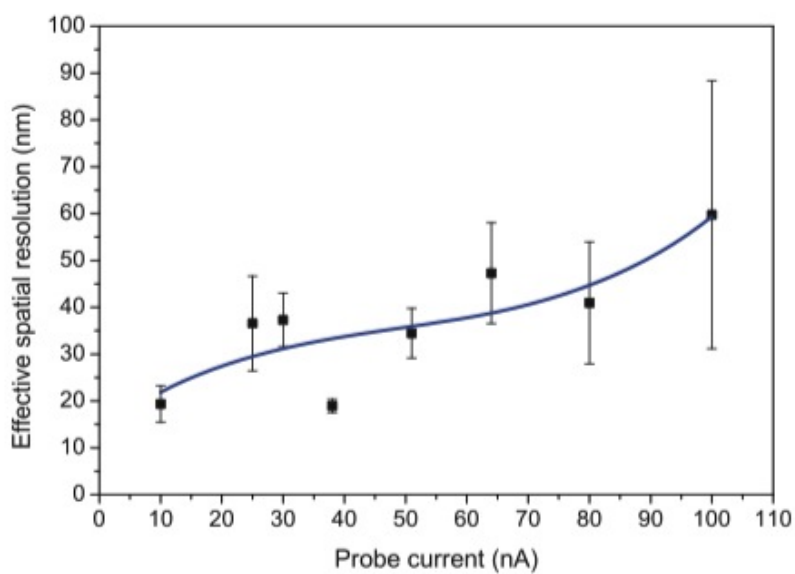


Figure 78: From Y. Chen et al. [45]

10.3 Stress Relief

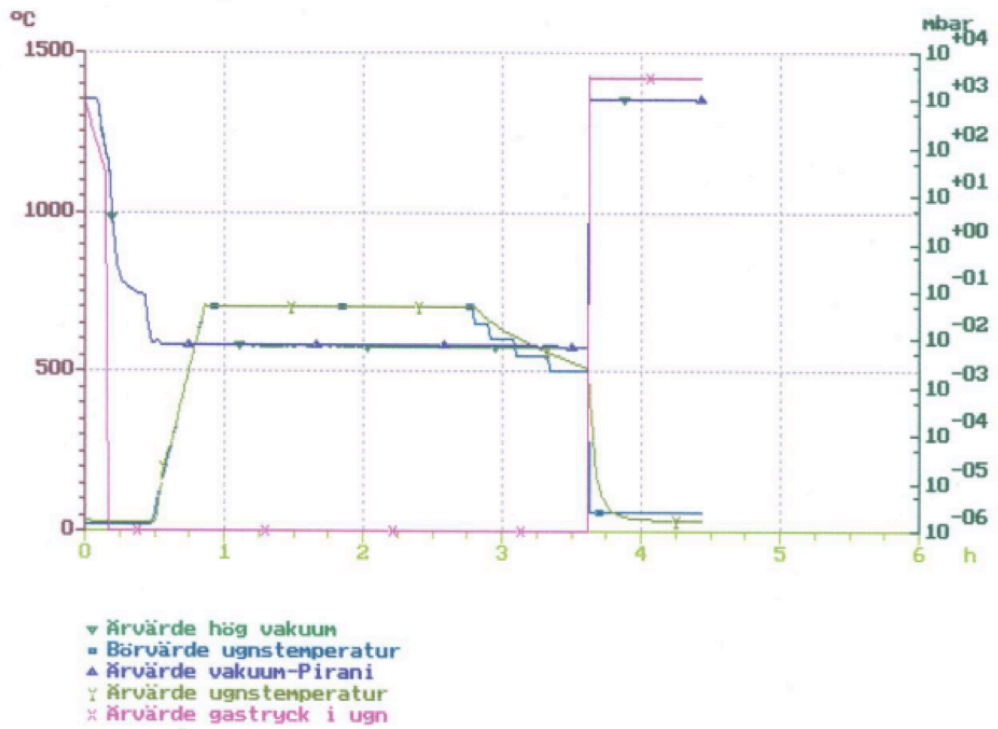


Figure 79: Light green curve show the temperature as a function of time, measured inside the vacuum furnace.

10.4 Macroetched Samples

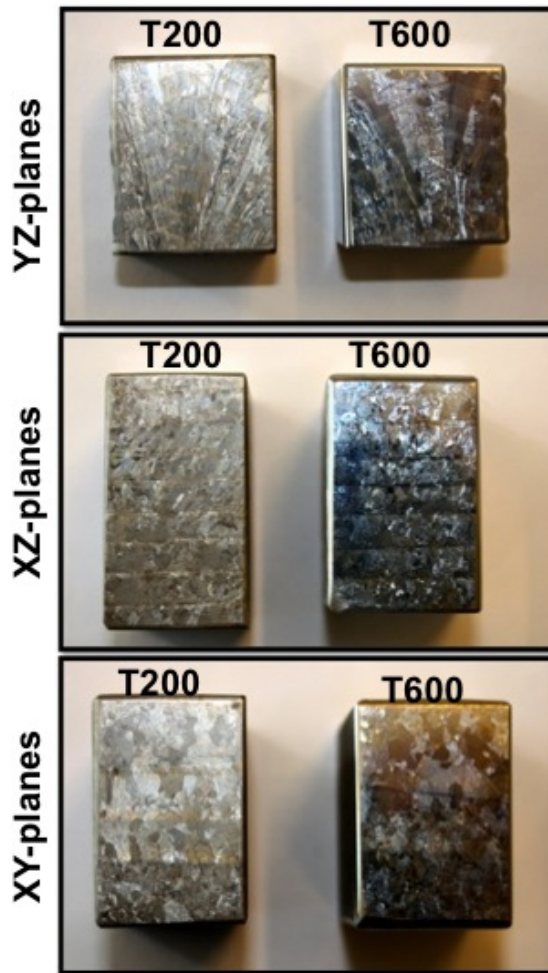


Figure 80: T200 specimen: etched with Kroll's etch + Weck's reagent. T600 specimen: etched with Kroll's etch only. The geometry of the specimens were measuring approximately: 3cm·2.5cm·2cm

10.5 SEM-Procedures before EBSD-Investigations

Before tilting the specimen inside the SEM-specimen chamber the procedures in Table 21 should be followed. They are executed on a horizontal specimen to "prepare" the optics of the SEM for EBSD-investigations i.e. it is much easier to adjust the optics on a horizontal specimen.

Table 21: Procedures conducted in the SEMs software before EBSD-investigations.

Procedure	Function
Insertion of large objective aperture	Increase fraction BSE on phosphor screen
High Current Mode	Increase fraction BSE on phosphor screen
High acceleration voltage	Band-width of Kikuchi bands decreases
Alignment of aperture	Reduce aberrations and astigmatism

The acceleration voltage is normally set high for EBSD-investigations. Despite the higher interaction volume in the specimen surface, will a higher acceleration voltage increase the efficiency of the phosphor screen. This results in brighter EBSPs with smaller band widths which is easier to index.

The alignment of the aperture is performed by selecting a small particle on the sample surface in good contrast to the background. If the aperture is not correctly adjusted, the particle will tend to move across the screen as it goes in and out of focus. Most SEMs will have a control-function that can help to adjust the apertures position such that a particle will stand at the same point on the screen when the focuse-point is altered. The Zeiss microscope used in this investigation have a so-called Wobble-function.

Adjustmets of working distance, dynamic-focuse, and the use of tilt compensation

After the specimen is tilted inside the SEM, the working distance (WD) must be correctly adjusted for the respective SEM. Because the EBSD-detector stands at a fixed point inside the vacuum chamber, the WD varies for different SEMs. See section 10.8 and Table 25 in the appendix for the WD used during this investigation. The optimized WD gives the best intensity on the EBSPs and a pattern center located close to the center of the EBSD-detector. To adjust the dynamic-focuse, it is helpful to use the tilt-compensation function of the SEM. This enables the operator to see a tilted sample as it where flat from a point of view parallel to the electron beam. Dynamic focuse ensures focuse on larger area of the tilted sample compared to when this function is switched off. For most SEMs the dynamic focuse is updated when the magnification is altered.

10.6 Frequently used CCD-Camera Settings in NORDIF 1.4.0

Hitachi Microscope

Table 22: The CCD-camera settings presented in Table 22 below was frequently used for a probe current of approximately 85nA in the Hitachi microscope. NB! Gain-values had to be adjusted.

<i>Setting</i>	<i>Aquisition Patterns</i>	<i>Calibration Patterns</i>
Frame rate	400fps	300fps
Resolution	120·120px	160·160px
Exposure time	2450 μ s	3283 μ s
Gain	1	1

Zeiss Microscope

Table 23: The CCD-camera settings presented in Table 23 below was frequently used for a probe current of approximately 37nA in the Zeiss microscope. NB! Gain-values had to be adjusted.

<i>Setting</i>	<i>Aquisition Patterns</i>	<i>Calibration Patterns</i>
Frame rate	100fps	50fps
Resolution	120·120px	240·240px
Exposure time	9950 μ s	19950 μ s
Gain	1	1

10.7 Hough Transformation Settings

Table 24: Hough transformation settings used in the TSL OIM Data Collection 5.32 Indexing software

Hough type	classic
Hough resolution	Low
Convolution mask	9·9
Min peak magnitude	5
Min peak distance	10
Peak Symmetry	0.5
Vertical bias	0%
Binned pattern size	120
Theta step size	1%
Rho fraction	90%
Max peak count	7
Min peak count	3

10.8 Camera Length for the two SEMs

Table 25: The camera lengths given in Table 25 were successfully used during indexing of the calibration patterns. This is input-information to the TSL OIM Data Collection 5.32 Indexing software. WD=working distance of SEM.

Microscope	Camera Length, Z (%)
Hitachi SU6600	~60 (for WD=26)
Zeiss	~80 (for WD=24)

10.9 Formula for Confidence Index

$$CI = \frac{V_1 - V_2}{V_2} \quad (14)$$

where:

V_1 =number of votes for the most likely solution

V_2 =number of votes for the second most likely solution.

CI= -1 for unindexed pixels. CI=0 when $V_1=V_2$, which mean that to phases or orientation have the same probability.

10.10 Thickness of primary α -phase in block T200 and T600

Table 26: Measurements primary α -phase thickness in Figure 55.

<i>Measurement</i>	<i>T200 (μm)</i>	<i>T600 (μm)</i>
1	40	30
2	38	31
3	35	35
4	53	33
5	45	36
6	44	41
7	30	28
8	30	34
9	41	33
10	23	36
Avg.	37.9	33.7

10.11 Interface Region between Substrate Plate and Block

The images below illustrates that equiaxed prior β -grains are present with various diameters in the interface region. Their morphology are relatively equiaxed.

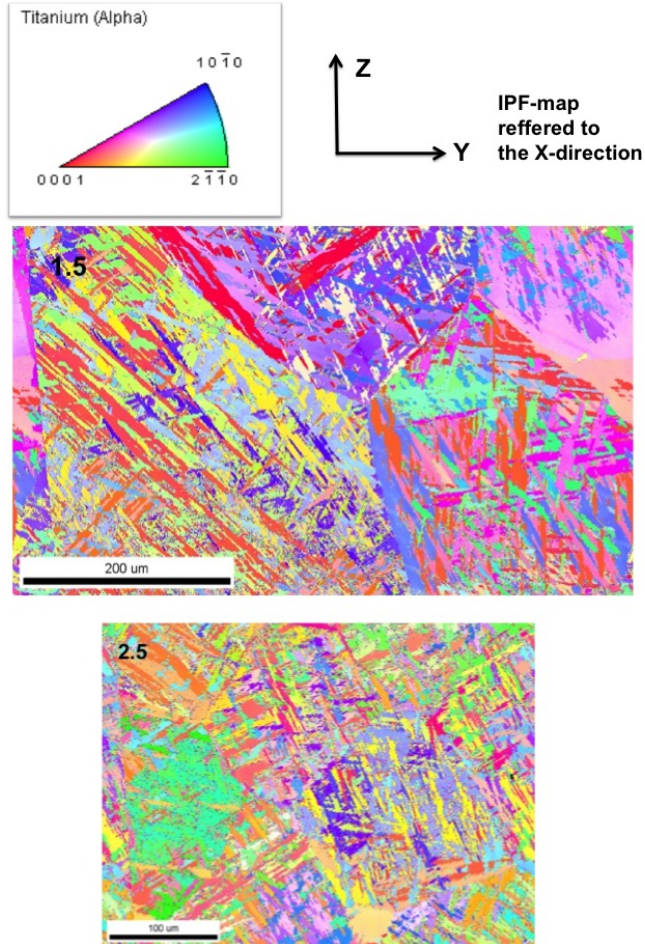


Figure 81: The images were taken from the transition-region between image 1 and 2, and 2 and 3 Figure 53.

10.12 Procedure to Create Taylor Factor Map

The procedure in Table 27 was used to create Taylor factor maps. NB! Remember to check that the tensile direction in your sample corresponds to the tensile direction indicated in the OIM Analysis 6.0 software. Only one slip system can be selected at the time. Different color scales can be adjusted to the dataset, to indicate maximum and minimum Taylor factor. If desired can histograms showing the distribution of the Taylor factor also be selected.

Table 27: Procedure to create Taylor factor map in OIM Analysis 6.0

Step 1	Open desired dataset
Step 2	Right click on All data
Step 3	Click new and then map
Step 4	Choose Taylor factor from the "Greyscale" in the map style

10.13 Summary of Quality Parameters of the EBSD-maps

In Table 29-37 below are all quality parameters of the EBSD-maps presented throughout the result-part of this report summarized. Note that these values are obtained for non-cleanup conditions in the OIM Analysis 6.0. Cleanup generally lead to better quality.

The highest quality was obtained in previous project work, see Table 28 below. The Zeiss microscope settings was essentially the same as in this work except a shorter working distance used, i.e. 20mm compared to 24mm. The probe current used remains unknown because the absorbed current was not measured during the project work.

Table 28: The best quality parameters obtained for the DMD-material.

<i>Figure nr.</i>	<i>CI</i>	<i>IQ</i>	<i>Fit</i>	<i>Nr. of good points/All Points</i>
Fig 26	0.56	134	0.87	89999/90000

Quality Parameters S1T200

Table 29: Summary of parameters obtained in Fig 41. NB! Note that the total number of points can vary between the different EBSD-scans.

<i>Figure nr.</i>	<i>CI</i>	<i>IQ</i>	<i>Fit</i>	<i>Nr. of good points/All Points</i>
Fig 41 3.5%	0.2	73.99	1.59	79871/80000
Fig 41 4.5%	0.2	73.99	1.59	79871/80000
Fig 41 5.5%	0.18	75.53	1.66	124023/124500

Table 30: Summary of parameters obtained in Fig 43. NB! Note that the total number of points can vary between the different EBSD-scans.

<i>Figure nr.</i>	<i>CI</i>	<i>IQ</i>	<i>Fit</i>	<i>Nr. of good points/All Points</i>
Fig 43 1	0.44	117.17	1.18	43150/43500
Fig 43 2	0.35	96.85	1.35	42962/43500
Fig 43 3	0.32	85.93	1.39	42355/44500

Quality Parameters S2T200

Table 31: Summary of parameters obtained in Fig 45. NB! Note that the total number of points can vary between the different EBSD-scans.

<i>Figure nr.</i>	<i>CI</i>	<i>IQ</i>	<i>Fit</i>	<i>Nr. of good points/All Points</i>
Fig 45 3.5%	0.36	115.56	1.28	93298/93375
Fig 45 4.5%	0.4	115.36	1.22	43218/43500
Fig 45 5%	0.43	113.46	1.16	110361/112000

Quality Parameters S1T600

Table 32: Summary of parameters obtained in Fig 46. NB! Note that the total number of points can vary between the different EBSD-scans.

<i>Figure nr.</i>	<i>CI</i>	<i>IQ</i>	<i>Fit</i>	<i>Nr. of good points/All Points</i>
Fig 46 3%	0.34	82.4	1.32	79485/80000
Fig 46 3.5%	0.37	86.93	1.26	78962/80000
Fig 46 4%	0.33	79.73	1.34	77823/80000

Quality Parameters S2T600

Table 33: Summary of parameters obtained in Fig 48. NB! Note that the total number of points can vary between the different EBSD-scans.

<i>Figure nr.</i>	<i>CI</i>	<i>IQ</i>	<i>Fit</i>	<i>Nr. of good points/All Points</i>
Fig 48 2.5 %	0.24	86.39	1.41	79984/80000
Fig 48 3.5 %	0.23	82.6	1.47	79321/79401
Fig 48 5.5 %	0.17	76.27	1.65	79747/80000

Quality Parameters of the Interface Region

Table 34: Summary of parameters obtained in Fig 53. NB! Note that the total number of points can vary between the different EBSD-scans.

<i>Figure nr.</i>	<i>CI</i>	<i>IQ</i>	<i>Fit</i>	<i>Nr. of good points/All Points</i>
Fig 53 1	0.38	96.25	1.15	420585/420595
Fig 53 2	0.29	96.43	1.38	187499/187500
Fig 53 3	0.26	92.69	1.45	187500/187500
Fig 53 4	0.13	51.73	1.78	124375/124400

Quality Parameters in Grain Boundary Region

Table 35: Summary of parameters obtained in Fig 55. NB! Note that the total number of points can vary between the different EBSD-scans.

<i>Figure nr.</i>	<i>CI</i>	<i>IQ</i>	<i>Fit</i>	<i>Nr. of good points/All Points</i>
Fig 55 T200	0.4	100.76	1.18	146266/146300
Fig 55 T600	0.26	81.64	1.41	106298/106600

Quality Parameters after Ion Milling

Table 36: Summary of parameters obtained in Fig 56 and Fig 59. NB! Note that the total number of points can vary between the different EBSD-scans.

<i>Figure nr.</i>	<i>CI</i>	<i>IQ</i>	<i>Fit</i>	<i>Nr. of good points/All Points</i>
Fig 56 Not ion-milled	0.43	136.28	1.02	122393/122400
Fig 56 Ion-milled 30min	0.42	149.03	0.98	122400/122400
Fig 59 T200	0.30	108.78	1.24	68208/68208
Fig 59 T600	0.21	102.34	1.52	59700/59700

Effect of Probe Current on Quality Paramters

Table 37: Summary of parameters obtained in Figure 60.

<i>Probe current</i>	<i>CI</i>	<i>IQ</i>	<i>Fit</i>	<i>Nr. of good points/All Points</i>
50nA	0.35	128.81	1.18	160000/160000
67nA	0.39	134.04	1.07	160000/159999
80nA	0.39	137.65	1.09	160000/160000

10.13.1 XrD-Spectras

The dashed lines along the horizontal axis in Figure 82 and Figure 83 indicates the different phases indentified. The colors iillustrates corresponding minerals and intensity peaks. The red, blue and grey curves are used by the software to quantify the identified phases. Blue curve is the actual diffractogram from the specimen. Red curve is the best fit between the measured phases and the identified phases. And the grey curve illustrate the differences between the red and blue curve.

XrD-Spectra T200

The spectra below has some peaks that were not indexed by the software. They are located in the rightern part of the spectra. This indicate that XrD-equipment used is not specialized for metallurgical phases. However, the phases that were indexed are included in Table 18 in the report.

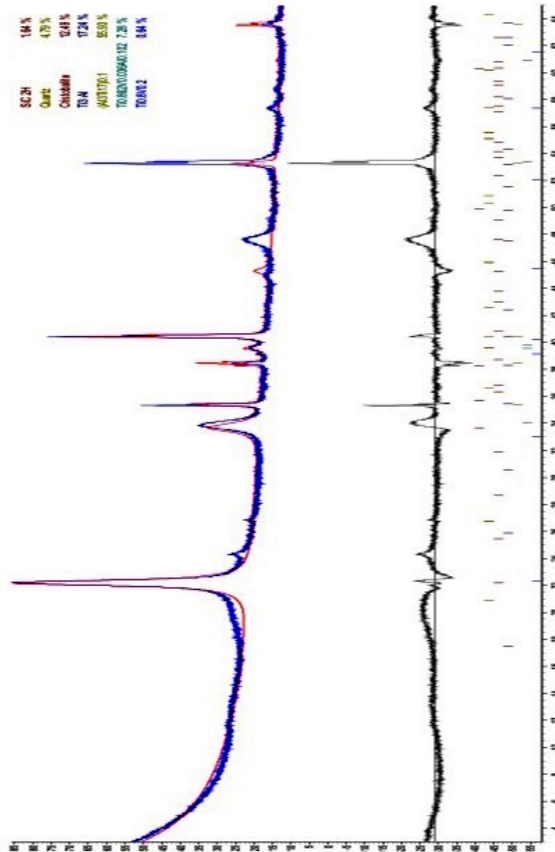


Figure 82: XrD-spectra from block T200. Intensity on vertical axis (counts), and d-value (angle) on horizontal axis.

XrD-Spectra T600

The spectra below has some peaks that were not indexed by the software. They are located close to the largest intensity peaks. This indicate that XrD-equipment used is not specialized for metallurgical phases. However, the phases that were indexed are included in Table 19 in the report.

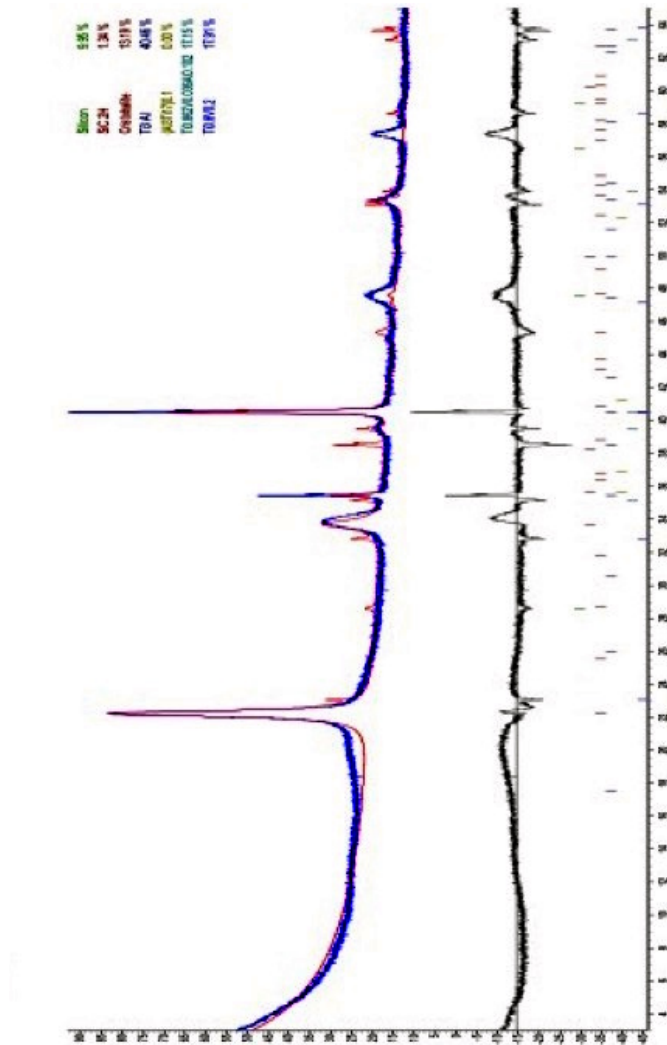


Figure 83: XrD-spectra from block T600. Intensity on vertical axis (counts), and d-value (angle) on horizontal axis.

10.14 Buy-to-fly ratio - DMD Compared to Machining

The buy-to-fly ratio is a common term within the aerospace industry. It is defined as the weight ratio between the raw material used for a component and the weight of the component itself. Due to the importance of weight optimization in this industry can this ratio be very large. Compared to machine the component directly, can machining combined with the DMD-process reduce this ratio significantly. Figure 84 below illustrates an example for a stiffening panel for airplanes and how the buy-to-fly can be reduced by the DMD-process. The traditional way to produce a stiffening panel today for an airplane is to machine the component directly from a forged or milled material. This can lead to a material loss of 80%. When Wire Additive + Arc Manufacture (WAAM), a comparable production technology to DMD, is implemented in the production of the panel can the component be produced with only 10% material loss.

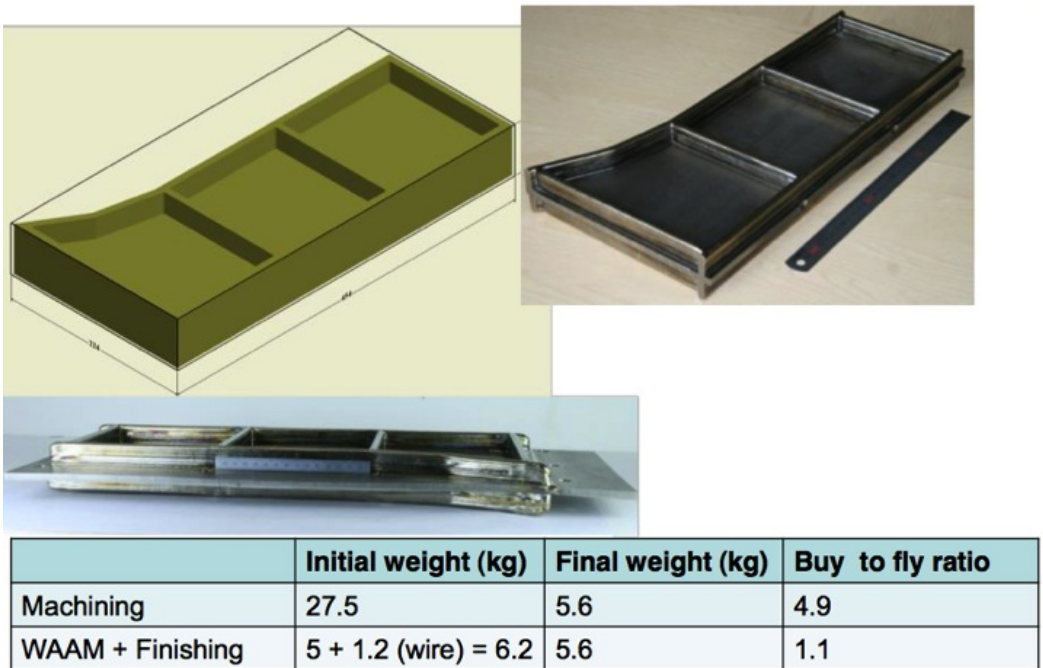


Figure 84: The buy-to-fly ration can be reduced significantly with the DMD-process compared to machining. The figure illustrates how this ratio can be reduced with the DMD-process. Reference Illustration: [34].

10.15 Comparison of Mechanical Properties between Lamellar, Bimodal and Equiaxed Microstructures

Mechanical datas from three different sources were selected for comparison of the microstructures. It can be seen from the table that the major limitation for the lamellar microstructure regarding mechanical properties is the lower elongation and reduction in area. However, the coarseness of the microstructures and the solid solution strengthening by interstitial elements are not taken into consideration in this comparison.

Table 38: RA=Reduction in Area. YS=Yield Strength. UTS=Ultimate Tensile Strength. El=elongation. KIC=Fracture toughness. References: (1) [53] M. Bendetti, (2) [54] S. Shrivastava, (3) [55] R.K. Nalla et al.

<i>Mechanical Property</i>	<i>Lamellar</i>	<i>Bimodal</i>	<i>Equiaxed</i>
UTS (MPa)	949 (2), 1055 (3)	978 (3)	1020 (2)
YS (MPa)	850 (1), 884 (2), 975 (3)	840 (1), 930 (3)	951 (2)
RA (%)	23 (2), 10 (3)	45 (3)	35
El(%)	13 (2)	64 (3)	15 (2)
KIC (MPa/m ^{0.5})	78 (2), 100 (3)	64(3)	61 (2)

10.16 Machining of Titanium

Ti is still regarded as one of the most difficult materials to machine, but the knowledge has improved and good results are obtained. However, Ti and its alloys does have metallurgical properties that makes machining more challenging than for instance some steels of the same hardness [5]. As a consequence, it is beneficial if machining of Ti can be reduced with methods such as DMD. Some metallurgical explanations for why Ti is difficult and expensive to machine are given in the bullet-point list below.

- Ti is poor conductor of heat and heat is easily concentrated at the tool face. This will lead to shortened tool life.
- Ti is a very reactive metal. At elevated temperatures during machining the reactivity is increased, and this may create an alloying tendency against the tool face.
- Ti have low elastic modulus. This increases the need for extensive clamping of the work piece to avoid deflection.
- The hexagonal crystal structure is known to have low work hardening properties. This will lead to absence of built-up edge during machining, which lead to less efficient removal of material during machining.

10.17 Tensile Properties of Laser-aided Deposited Ti6Al4V after Different Heat Treatments

The mechanical datas in Table 39 were obtained after tensile tests perpendicular to the deposition direction [52]. The microstructure observed in the laser deposited material is very similar to the microstructure investigated in this work. It can be seen that the strength values drops with increased heat treatment temperature, while the elongation have a maximum for a heat treatment temerperature of 950°C followed by furnace cooling. It was reported that the 950°C annealed samples showed a better ductility due to a coarser and more uniform microstructure. The sample annealed at 1050°C showed lower ductility because of thicker grain boundary α . The prior β -grains had a parallell orientation to the tensile axis for all the samples, this mean that the grain boundary α were subjected to tensile stress in contrast to the shear stress this work. However, cracks may easily propogate along the grain boundaries in either case. Table 39 also illustrates that the elongation are generally improved with additional heat treatment after deposition.

Table 39: The tensile samples in this table were heat treated at 950°C and 1050°C for one hour followed by either air cooling or furnace cooling. The best ductility was obtained for 950°C followed by furnace cooling.

<i>Heat Treatment</i>	<i>YS (MPa)</i>	<i>UTS (MPa)</i>	<i>Elongation (%)</i>
As-deposited	1105±19	1163±22	4±1
950°C/air cool	975±15	1053±18	7.5±1
950°C/furnace cool	959±12	1045±16	10.5±1
1050°C/air cool	931±16	1002±19	6.5±1
1050°C/furnace cool	900±14	951±15	7.5±1

10.18 Methods for Improving Mechanical Properties of the DMD-Material

Recent investigations have found new methods to control the coarseness of the β -grains after deposition. The methods will be presented below, and are based on the reference [34]. All the methods have in common that they attempt to interrupt the easy growing of columnar β -grains during solidification of the weld pool or to use grain refiners to achieve equiaxed β -grains. As a consequence of more homogeneous distribution of β -grains, the final components will have more isotropic mechanical properties.

Subsequent Rolling after Deposition

Nucleation points (stored energy) are introduced to the material after rolling. This will induce recrystallisation in highly deformed region when layers are reheated during subsequent deposition. The rolling can be performed immediately after deposition (when the material have solidified) in a combined deposition and rolling equipment.

Grain Refining

Successful tests were performed by using boron coating of a Ti6Al4V-wire for grain-refining. The β -grains appeared to be more equiaxed with the boron coating in contrast to long columnar β -grains pervading deposition layers without coating.

Wire feed rate

The length of the columnar β -grains appeared to be strongly dependent on the wire feed rate. Wire feed speed $>2.0\text{m/min}$ lead to blocking of columnar grains giving more equiaxed grains.

10.19 Fusion Line between Single String and Substrate Plate

The line in Figure 85 indicate the fusion line for a single string on a plate. The fusion line can be observed approximately 2.5-3mm below the plate surface. However, the HAZ were a coarsening of the plate microstructure can be observed can reach 6-7mm below the surface. See unaffected plate structure in the lower part om the image. Image reference: NTiC.

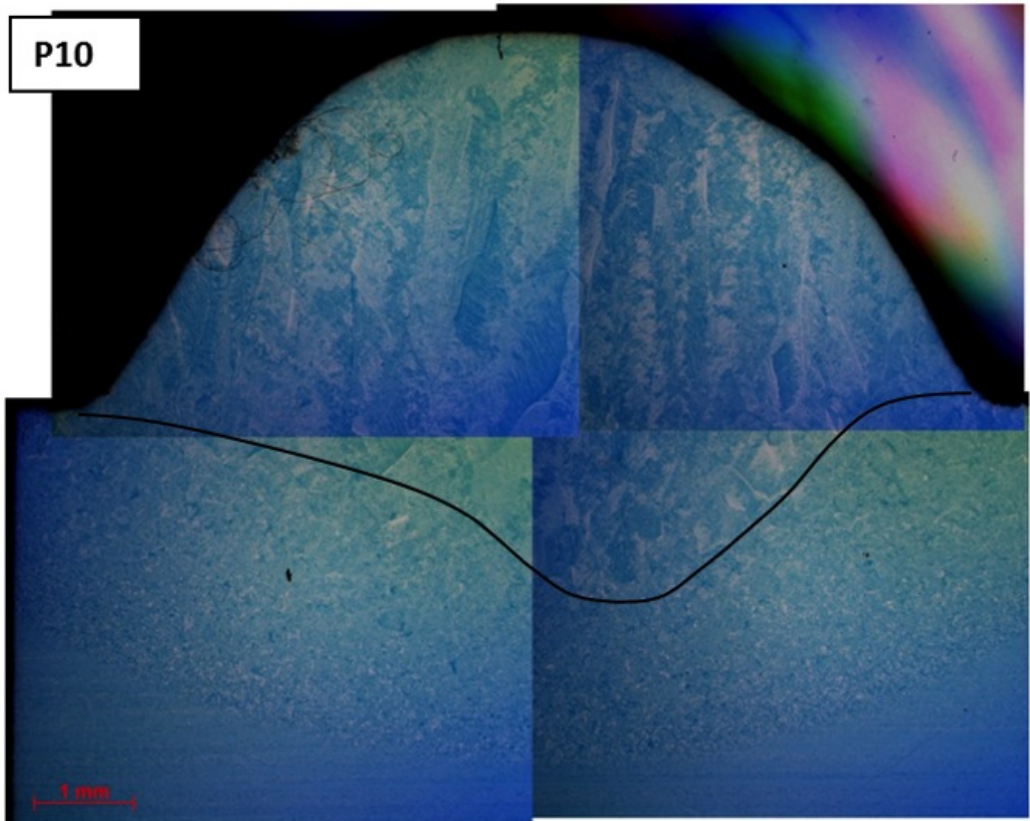


Figure 85: Overview of the transition from bimodal plate structure to columnar β -grains. Scalebar=1mm.

10.20 Pole Figures

The coordinate axis of the sample in Figure 86 can be modified to apply for the DMD-process:

Rolling Direction (RD) = Deposition direction, X

Transverse Direction (TD) = Thickness direction, Y

Normal Direction (ND) = Building Direction, Z

The example below is illustrated for a cubic crystal but the same procedure applies to HCP. The example below is for $\{111\}$. The first step is to let the principal lattice vectors of the unit cell, intersect with the reference sphere. The intersection points can further be projected on the equatorial plane, by drawing a line between the points and the pole of the reference sphere. It is the equatorial plane with the projected points which is referred to as the pole figure. The pole figure can for instance be used to determine the texture of a material i.e. which grain orientations that dominates.

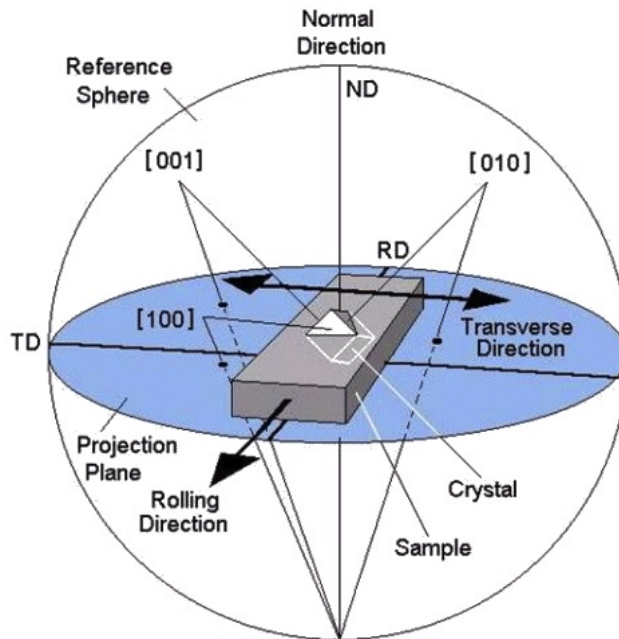


Figure 86: Theoretical background for making pole figures. Image reference: www.ebsd.com